1

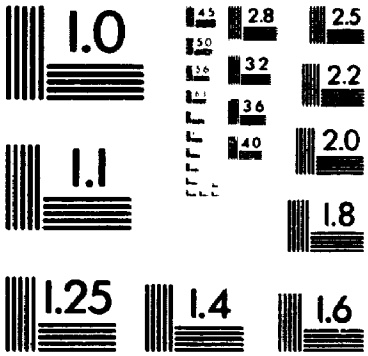

MicroD

National Library of Canada
Bibliothèque nationale du Canada

Canadian Theses Service
Service des thèses canadiennes

Ottawa, Canada
K1A 0N4

NOTICE

The quality of this microform is heavily dependent upon the quality of the original thesis submitted for microfilming. Every effort has been made to ensure the highest quality of reproduction possible.

If pages are missing, contact the university which granted the degree.

Some pages may have indistinct print especially if the original pages were typed with a poor typewriter ribbon or if the university sent us an inferior photocopy.

Reproduction in full or in part of this microform is governed by the Canadian Copyright Act, R.S.C. 1970, c. C-30, and subsequent amendments.

AVIS

La qualité de cette microforme dépend grandement de la qualité de la thèse soumise au microfilmage. Nous avons tout fait pour assurer une qualité supérieure de reproduction.

S'il manque des pages, veuillez communiquer avec l'université qui a conféré le grade.

La qualité d'impression de certaines pages peut laisser à désirer, surtout si les pages originales ont été dactylographiées à l'aide d'un ruban usé ou si l'université nous a fait parvenir une photocopie de qualité inférieure.

La reproduction, même partielle, de cette microforme est soumise à la Loi canadienne sur le droit d'auteur, SRC 1970, c. C-30, et ses amendements subséquents.

NL-339 (r. 88/04) c

Canada

Miniature Hybrid Microwave Integrated Circuit Passive Component Analysis Using Computer-Aided Design Techniques

by

Edward Frlan

This thesis is submitted to the Faculty of Graduate Studies and Research in partial fulfillment of the requirements for the degree of

Master of Electrical Engineering

Department of Electronics
Carleton University
Ottawa, Ontario

© August 22, 1989

National Library of Canada
Bibliothèque nationale du Canada

Canadian Theses Service
Service des thèses canadiennes

Ottawa, Canada
K1A 0N4

The author has granted an irrevocable non-exclusive licence allowing the National Library of Canada to reproduce, loan, distribute or sell copies of his/her thesis by any means and in any form or format, making this thesis available to interested persons

L'auteur a accordé une licence irrévocable et non exclusive permettant à la Bibliothèque nationale du Canada de reproduire, prêter, distribuer ou vendre des copies de sa thèse de quelque manière et sous quelque forme que ce soit pour mettre des exemplaires de cette thèse à la disposition des personnes intéressées.

The author retains ownership of the copyright in his/her thesis. Neither the thesis nor substantial extracts from it may be printed or otherwise reproduced without his/her permission.

L'auteur conserve la propriété du droit d'auteur qui protège sa thèse. Ni la thèse ni des extraits substantiels de celle-ci ne doivent être imprimés ou autrement reproduits sans son autorisation.

ISBN 0-315-54372-8

Canada

The undersigned hereby recommends to the Faculty of Graduate Studies and Research acceptance of the thesis,

MINIATURE HYBRID MICROWAVE INTEGRATED CIRCUIT PASSIVE COMPONENT ANALYSIS USING COMPUTER-AIDED DESIGN TECHNIQUES

submitted by Edward Frlan, in partial fulfilment of the requirements for the degree of Master of Engineering

Thesis Supervisor

Chairman,
Department of Electronics

Department of Electronics
Faculty of Engineering

September 1989

Abstract

This thesis explores the design and analysis of various MHMIC passive components using CAD techniques. Specifically, a novel approach is investigated in order to accurately characterize the performance of square spiral inductors and transformers to their first resonant frequency. Also, thin-film overlay couplers are analyzed and investigated in this thesis. An application of the transformers in an amplifier is discussed as well as the expected performance of such a circuit.

Acknowledgements

I would like to express deepest appreciation to my supervisor Professor J.S. Wight for his support .

Also, I would like to thank the Communications Research Centre (Ottawa) and specifically Michel Cuhaci and Sara Meszaros for their help and encouragement. I am indebted as well to Langis Roy for his support.

Finally I would like to thank the Natural Sciences and Engineering Research Council for their funding.

Table of Contents

List of Tables

List of Figures

Nomenclature

Symbol	Description
C_c	discontinuity capacitance of chamfered microstrip bend
C_e	even-mode capacitance
C_f	total feedback capacitance in square spiral inductor
$C_f(f)$	total frequency-dependent feedback capacitance of square spiral inductor
C_g	capacitance-to-ground
C_{g1}	total capacitance to ground of transformer primary
C_{g2}	total capacitance to ground of transformer secondary
C_m	static intersegment capacitance, or frequency-dependent mutual capacitance between transformer primary and secondary
$C_{m,eff}$	frequency-dependent mutual capacitance between two adjacent segments in a square spiral inductor
C_o	odd-mode capacitance
C_{par}	parallel plate capacitance beneath microstrip line
C_{total}	total capacitance of a microstrip line
C_{01}	outer half capacitance-to-ground of square spiral inductor
C_{02}	inner half capacitance-to-ground of square spiral inductor

C_1	half of the equivalent stripline capacitance
C_{12}	parallel plate capacitance of overlay coupler
D	distance
D_{cent}	distance between the centers of two parallel conductors
f	frequency
GMD	geometric mean distance
I_{DS}	DC bias current
i	current
L	total inductance of square spiral inductor
L_1	total inductance of transformer primary
L_2	total inductance of transformer secondary
L_c	discontinuity inductance of a chamfered microstrip bend
L_{image}	total static image inductance of square spiral inductor
$L_{image}(f)$	total frequency-dependent image inductance of square spiral inductor
L_{mut}	total static mutual inductance of square spiral inductor
$L_{mut}(f)$	total frequency-dependent mutual inductance of square spiral inductor
L_{self}	total self inductance of square spiral inductor
$L_{total,stat}$	total static inductance of square spiral inductor
L_1	total inductance of transformer primary
$L_{1,image}$	static image inductance of transformer primary
$L_{1,image}(f)$	frequency-dependent image inductance of

	transformer primary
$L_{1,mut}$	static mutual inductance of transformer primary
$L_{1,mut}(f)$	frequency-dependent mutual inductance of transformer primary
$L_{1,self}$	static inductance of transformer primary
$L_{1,stat}$	total static inductance of transformer primary
L_2	total inductance of transformer secondary
$L_{2,image}$	static image inductance of transformer secondary
$L_{2,image}(f)$	frequency-dependent image inductance of transformer secondary
$L_{2,mut}$	static mutual inductance of transformer secondary
$L_{2,mut}(f)$	frequency-dependent mutual inductance of transformer secondary
$L_{2,self}$	static inductance of transformer secondary
$L_{2,stat}$	total static inductance of transformer sencondary
M	mutual inductance between transformer primary and secondary
M_{image}	total static image inductance portion of transformer M
$M_{image}(f)$	total frequency-dependent image inductance portion of transformer M
M_{mut}	total static mutual inductance of transfomer M
$M_{mut}(f)$	total frequency-dependent mutual inductance of transfomer M

M_{stat}	total static mutual inductance between transformer primary and secondary
M_{11}	self inductance of coupler top plate
M_{12}	mutual inductance between top and bottom plate of overlay coupler
M_{22}	self inductance of coupler bottom plate
l	length
R	resistance in inductor model
R_{DC}	DC resistance of a rectangular conductor
R_{ohmic}	ohmic resistance
R_1	total resistance of transformer primary
R_2	total resistance of transformer secondary
S_{ij}	S-parameter
V_{DS}	DC bias voltage
v	voltage
v_{air}	speed of light in air
Y_{ij}	Y-parameter
Z_0	characteristic impedance of microstip
α_d	dielectric attenuation loss
ε_{eff}	effective permittivity relative to free space
ε_r	permittivity relative to free space
ε_0	dielectric permittivity of free space
λ_0	wavelength in free space
λ_g	wavelength in microstrip
σ	conductivity
θ	phase
μ	permeability of free space
ω	radian frequency

1 Introduction

1.1 Introduction

Previously microwave circuits have been developed in either coaxial or waveguide systems. However the inherent flexibility of planar circuit technology, in which a single dielectric sheet is used as a substrate, allows a significant reduction in weight and bulk.[1] The many kinds of transmission lines, each with their own different properties, that can be fabricated on planar substrates can be very advantageous in specific applications. For example, if slotlines are used then there are no holes required to be drilled to a ground plane as in microstrip. Components can be laid directly on top of the substrate which significantly simplifies the manufacturing aspect of the circuit.

The first planar circuit technique to be used at microwave frequencies is MIC (Microwave Integrated Circuit) technology in which all of the circuit paths are etched onto a glass reinforced Teflon substrate (such as R/T Duroid) and components soldered on. Typically all of the matching in a circuit using MIC technology is done by distributed techniques (ie. using transmission lines and stubs) or by discrete lumped elements.

MMIC (Monolithic Microwave Integrated Circuit) technology dates back to the early 1970's. This particular technology uses a semiconductor such as GaAs as the substrate material so that the passive and active components can be fabricated using the same process. In this way the active device is directly integrated on the substrate and discontinuities between FETs and transmission lines are avoided.[2] The problems with MMICs at the moment are that they have a fairly low yield and have to be produced in large quantity in order to be economical. As well, the turnaround time for a typical MMIC iteration is approximately two months, depending on the foundry, which in certain cases can be considered excessively long.

The newest trend in microwave circuits is MHMIC (Miniature Hybrid Microwave Integrated Circuit) technology which is based on the integration of monolithic passive lumped element components with commercially available active hybrid components. Hence MHMIC circuits have similarities with both MIC and MMIC circuits. This technology is well-suited to small and medium quantity applications and complements MMIC technology in many ways. In some aspects it has more flexibility than monolithic technology since active components can be chosen for specialized applications for better overall circuit performance. Typical MMIC foundries are not generally providing specialized active devices such as power or low-noise FETs. MHMIC's complements

MHMIC circuits are usually fabricated on ceramic substrates such as Alumina or quartz which have very low loss tangents and have a higher resistivity than the semi-insulating GaAs substrate used in monolithic circuits. The typical turnaround time for an MHMIC circuit is six weeks which is less than that for an MMIC circuit.

Some MMIC and MHMIC circuits use traditional distributed elements for impedance matching. However, this is rare and it is usually more advantageous to use lumped element matching. Distributed elements have a much higher Q factor than do lumped elements but at the same time their bandwidth is very narrow. The fact that lumped elements have a very large bandwidth and that they take up much less area than a distributed circuit, makes them indispensable for MHMIC circuit design. Although their Q factor is much lower, for many circuits the additional losses are not critical and can be acceptable. Therefore lumped element analysis is a fundamental aspect of this thesis.

1.2 Objectives

The MHMIC technology which is presently being developed requires the precise knowledge of passive component behavior. Unless the passive components can be accurately characterized to at least their first resonant frequency, it is difficult to produce well-behaved active circuits. Also, since the final circuits are not easily tuneable, it is important to try and produce a successful circuit on the first iteration. At the present time most of the microwave computer-aided design models are not advanced enough to model passive MHMIC components adequately. This thesis will investigate and solve the problems of modeling and optimization of several key passive components in order that they can be used in different types of microwave circuits. A novel, lumped element modeling approach will be described, which can take frequency dependent effects of a structure into account. Specifically, square spiral inductors and transformers, and overlay couplers will be studied intensively. Furthermore, a study of pushpull amplifier design using a center-tapped transformer will be undertaken.

1.3 Organization

The analysis and modeling of square spiral inductors is looked at in Chapter 2. The method used to analyze the spiral inductors is integrated into a FORTRAN program which is installed into a commercial microwave computer-aided design package. A general investigation is carried out in order to determine how the inductors can be optimized. Also, an application of the inductors is investigated by looking at the role they play in a delay line composed entirely of passive elements.

In Chapter 3, square spiral transformers are investigated. Since they are

very similar in structure to the inductors, they are analyzed in a similar manner. Two different types of transformers are investigated, namely the non-center-tapped transformers and the application-specific center-tapped transformers. The techniques used to evaluate the parameters of these devices is again integrated into two different computer programs.

A novel broadside coupled structure is analyzed and studied in Chapter 4 as well as some of the possible applications of such a structure in typical microwave circuits.

Finally, a class-A MHMIC pushpull amplifier which is designed using the center-tapped transformers is analyzed in Chapter 5.

The body of investigation carried out for this thesis will be summarized and conclusions drawn from the knowledge gained while studying the passive microwave circuits in Chapter 6.

2 Modeling and Analysis of Square Spiral Inductors

2.1 Introduction

Spiral inductors have many applications in planar microwave circuit technology, such as amplifier matching, filters and bias circuits. As stated in the introduction, the fact that square spiral inductors are broadband and can be considered approximately as a lumped inductance value makes them very useful. In combination with thin film capacitors, many types of circuits for different applications can be constructed, such as low pass delay line filters. Already, in MMIC designs, the spiral inductor is a basic component used in almost any circuit. Since MHMIC technology is very similar to MMIC technology, it appears that spiral inductors will play an equally important role in this new microwave circuit technology.

If small inductances (ie. below 2 nH), are required, then a rectangular cross-section ribbon can provide the required inductance. This is fabricated as a certain length of microstrip transmission line. However, if higher inductances are required then spiral inductors must be used to provide the necessary inductance. The tight coupling between the adjacent lines provides a higher inductance than the equivalent length of straight rectangular ribbon. Spirals can be fabricated in either circular or rectangular geometries. The emphasis in this thesis is on spiral inductors of a rectangular geometry, which are more readily fabricated with the current technology.

A typical thin film rectangular spiral inductor is shown in Figure 2.1. The inductor itself is the structure in the center of the photograph. The two wide lines on the top and bottom are the ground connections used with the ground-signal-ground probes when measuring. For comparison a diagram of an octagonal spiral can be seen in Figure 2.2 In this case, the metal leading out of the structure is seen to be an underpass, rather than an overpass. This type of inductor is a geometrical approximation to a circular inductor.

The square spiral inductors fabricated using thin film technology behave like true lumped inductors, with an approximately constant inductance value below their first resonant frequency. Above the first resonant frequency the inductors behave like capacitors and therefore they cannot operate in this range. Although their inherent broadband characteristics are very useful in the applications mentioned earlier, their typical Q-factor is quite low (from 20 to 60) and can sometimes have a negative effect on overall circuit performance. The circular spiral, as compared to a square spiral, has a higher quality factor, but will also has a smaller inductance for the same area.

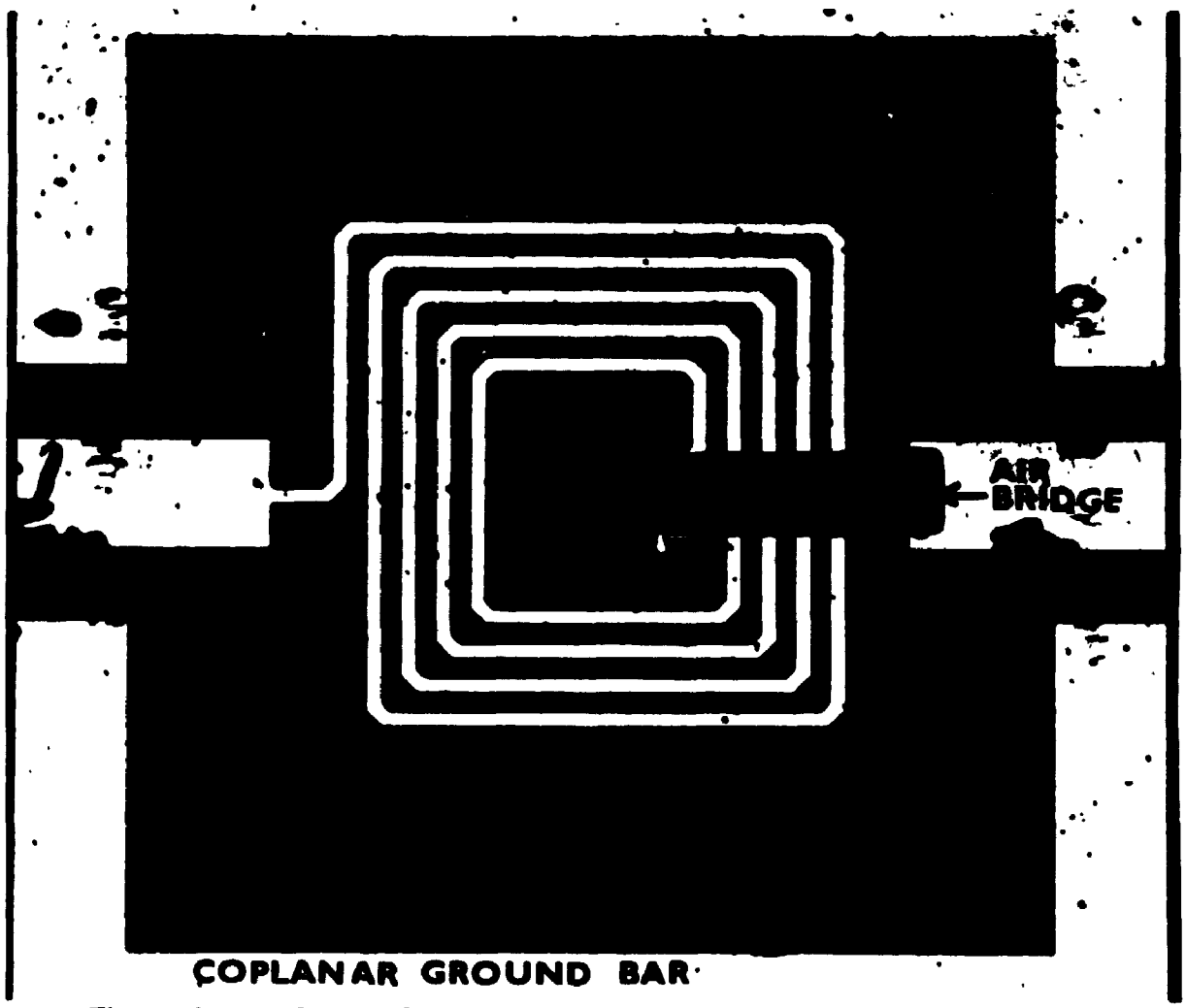

Figure 2.1 Square Spiral Inductor With Overpass to Output

The tight inductive coupling between the transmission lines in a square spiral inductor helps to increase the inductance considerably as compared to an equal length of straight line. Furthermore, since spiral inductors are very compact, their compatibility with monolithic and hybrid microwave integrated circuits is excellent. The analogy to square spiral inductors in low frequency circuits would be a wire-wound inductor in which a filament is wound in a loop many times in order to increase the inductance significantly over that of just a single loop.

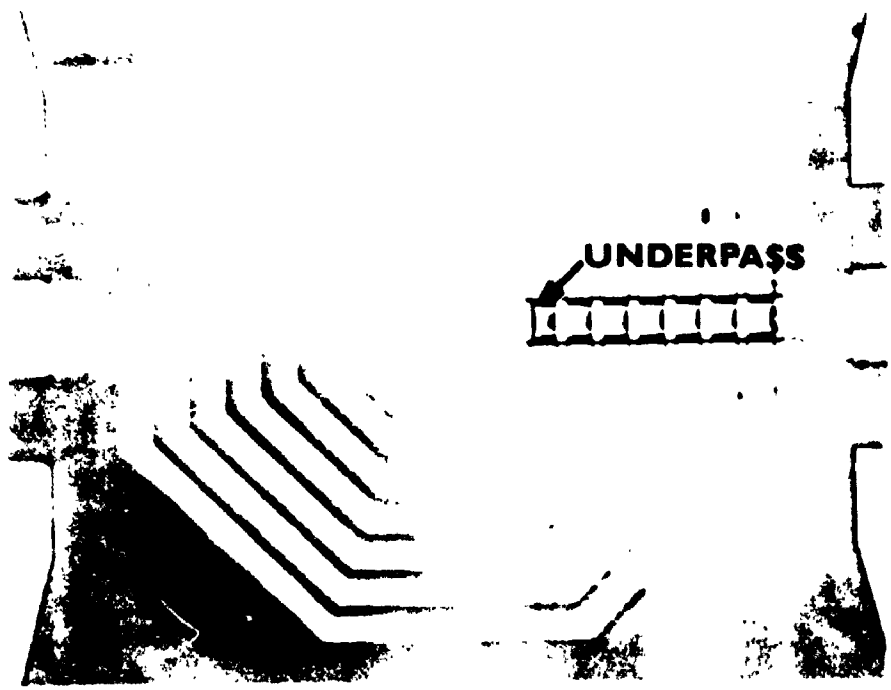

Figure 2.2 Octagonal Spiral Inductor with Underpass to Output
(Fabricated by Adams-Russell foundry for CRC)

2.2 Fabrication of MHMIC Circuits

The technology used to produce MHMIC circuits is based on thin-film processing techniques. Ceramic and glass substrates are most often chosen due to their high temperature stability, which is a critical criterion during several of the fabrication stages. Organic substrates such as RT/Duroid are incapable of withstanding the high temperatures of processing, and do not have the extremely smooth (1 μinch) surface finish required.

The circuits are fabricated using five levels which can be seen in Table 2.1. The circuits used in this study were all fabricated at the Microelectronics Facility, CRC (Ottawa).

Table 2.1

Five Levels Present in MHMIC Circuit Fabrication

Level No.	Name	Description
1	FLM	first level metal, used for transmission lines, interconnects, spirals etc.
2	RES	thin-film resistors
3	DIE	dielectric used for capacitors, resistor passivation
4	WIN	contact windows for top electrodes and air bridge supports
5	ABDF	airbridge metallization used for capacitor top electrodes as well as airbridges

These levels are described in more detail below.

FLM:

The first layer of metal is defined using liftoff for maximum precision. A 300 Å seed layer of titanium-tungsten (Ti:W) is sputtered onto the substrate in order to provide adhesion. A dark field mask is used in order to develop the photoresist wherever the gold is desired. Then 300 Å of Ti and 1 μm of gold is evaporated onto the substrate. Finally the unexposed photoresist is washed away.

The ground plane of the substrate is produced in the same way with a final gold thickness of 2 μm.

RES:

The resistors are produced using the Ti:W adhesion layer, whose resistivity can be controlled during sputtering. The substrate undergoes baking which stabilizes the Ti:W and gives a value of approximately 100 Ω/square. The resistance/square of the thin-film resistors can have a tolerance of 20 per cent, which is considered acceptable for most microwave applications.

DIE:

A thin (2000 Å) layer of silicon nitride (Si_3N_4) can be applied to the entire substrate and then selectively etched off. This step of the fabrication process is used to produce metal-insulator-metal (MIM) capacitors, however it can also be used to prevent the possibility of short circuits occurring with air bridges.

WIN, ABDF :

Contact windows are placed in a thick layer of photoresist in order to define the areas for the top layers of MIM capacitors and air bridge supports. Then 300 Å of Ti is applied to ensure adhesion and this is followed by 2000 Å of gold. The second level metal which is composed of 4 μm of gold is applied using either selective plating or conventional etching techniques.

In Figure 2.3 the typical structure of an MHMIC circuit can be seen. The thin-film resistor is formed by leaving the thin layer of Ti:W unexposed. during etching of the adhesion layer. The MIM capacitor has first layer gold as its bottom electrode, the silicon nitride layer as the dielectric, and the thick second layer gold as its top electrode.

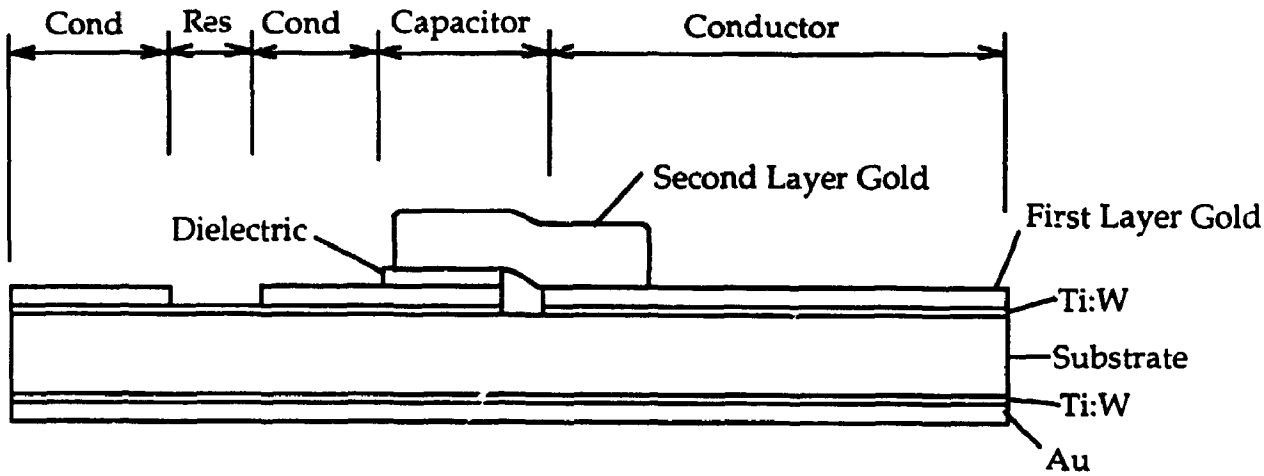

Figure 2.3 Structure of a Typical MHMIC Circuit

The MHMIC circuits realized to date have been fabricated on both 1"x1" alumina and quartz substrates of various thicknesses. The alumina substrates are a very good choice for microwave circuits operating at

frequencies below 20 GHz, as they have a high relative permittivity which affords a significant reduction in the size of the various components. As well, alumina has very low dielectric losses and can withstand the high temperatures which must be endured during fabrication. Above 20 GHz, and into the millimeter wave range, substrates such as quartz are preferred, since the wavelength reduction is not as high as for alumina and therefore fabrication tolerances become more reasonable.

2.3 Analysis

Lumped elements are by definition a small fraction of a wavelength in size. The fact that a structure such as a spiral inductor is made up of a combination of transmission lines can be ignored, as long as the total length of the structure is much less than $\lambda/30$. Even when the distributed effects become important, the component can still be used as long as it can be modeled accurately. Due to the inherently small sizes of lumped elements, they have only been actively used at microwave frequencies in the past two decades : the first lumped element amplifier was designed in the early 1970's, producing 10 dB gain at 2.25 GHz[3]. The small line lengths and accurate circuit definition required were not possible with the technology available in the 1960's.

The lumped element approach is always a more economical use of space than the equivalent distributed approach, which is based on the use of lengths of transmission lines and stubs which can be a significant fraction of a wavelength. Lumped elements as well have a much higher adaptability and flexibility for many different applications.

A number of methods have been developed to analyze square spiral inductors. The first method developed is Greenhouse's static method[4] : the total inductance of an inductor is calculated by breaking it up into segments and calculating all of the self and mutual inductances between the segments. The method is applicable only at very low frequencies

because capacitive effects in the structure are ignored.

Another method which is suitable for inductors with less than two turns is that of Camp[5] and Cahana[6]. Their's is a distributed approach which assumes that for a certain length of the inductor, the presence of two lines running along side each other can be considered as two coupled lines. Hence, the even- and odd-mode impedances of the coupled line structure can be calculated and therefore the inductor can be analyzed. The method has certain limitations: the coupling of segments that are on opposite sides of the inductor is not calculated, and as a result an error will be introduced into the final results. As a result this method will model the inductor as having too much inductance, since the negative mutual inductance of the opposite sides is not included.

The method outlined by Shepherd[7] is a multiconductor transmission line approach which also incorporates a special method to take into account the feedback capacitances of the airbridge. A similar approach is taken by Wolff[8].

A method using a combination lumped and distributed approach is outlined by Lang[9]. The author claims that the method formulated can analyze the inductors accurately to at least three times their resonant frequency. A lumped approach in which the inductor is split up into equivalent inductances and capacitances is put forth by Dueme[10].

A highly field theoretical method is described by Parisot[11] to determine the inductance of square spiral inductors. Also, Jansen[12] uses a highly CPU intensive approach in which multiconductor, multilayer hybrid-mode transmission line computations are performed in order to analyze the inductor very accurately to 18 GHz.

The method developed here to analyze the spiral inductors is essentially based on a lumped circuit equivalent model. This route was chosen as it is a less computer intensive procedure than other possible methods, such as a full- wave analysis. Although the method has certain limitations above the resonant frequency of the structure, it is useful at

frequencies below resonance.

Furthermore, the method is quite flexible and can easily be modified to other planar microwave line structures, as exemplified by transformers, which are discussed later.

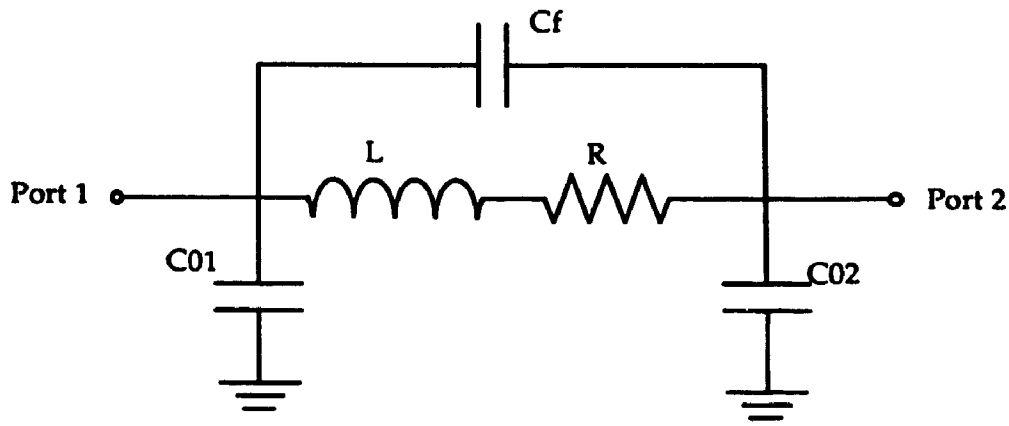

Figure 2.4 Frequency-Dependent Model of Square Spiral Inductors

Figure 2.4 shows a standard lumped element equivalent model which in addition to an inductance, includes the effects of losses (R), capacitive feedback (C_f), and capacitance to ground (C_{01} and C_{02}) Some authors have dismissed this model as only being accurate enough for low frequencies. However, work done in this thesis has shown that, by including appropriate frequency-dependence in some of the elements, this model is accurate up to at least the first resonant frequency. For instance, the inductance in the model, L, changes with frequency and must be calculated accordingly. The capacitors to ground, C_{01} and C_{02}, are frequency independent, but C_f is frequency dependent, and becomes significant at frequencies at and above resonance. Essentially it is the combination of the feedback capacitor C_f with the inductor L which dictates the resonant frequency of the inductor, whereas the ground capacitances have a lesser effect on the resonant frequency. It is desirable to extend the range of operation of these spiral inductors as much as possible by reducing the parasitics which are involved in the model. When designing a

microwave circuit with the spiral inductors, the parasitics must be as small as possible.

2.3.1 Model Inductance Analysis

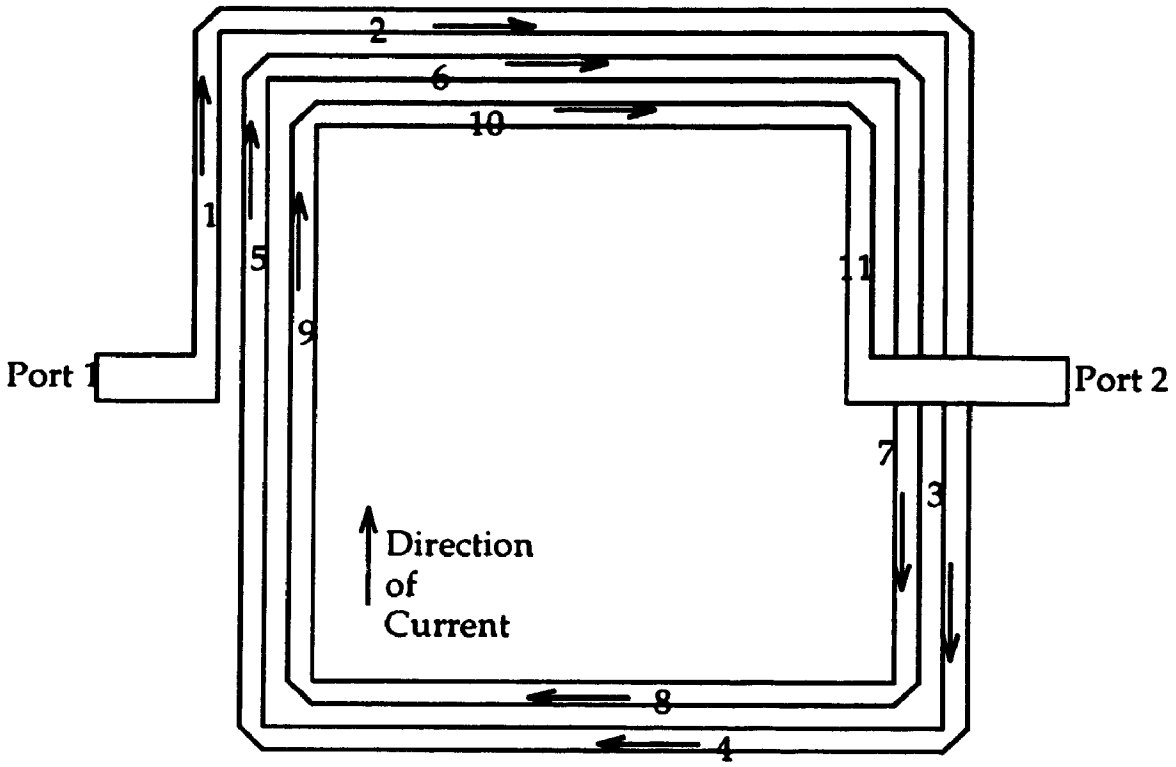

Figure 2.5 Sample Spiral Inductor with Current Directions Shown

The structure of Figure 2.5 must be broken up into sections in order to facilitate the analysis. Each straight segment of the inductor has a certain amount of self inductance; this self inductance can be calculated for a line of rectangular cross-section from a formula developed by Grover[13]. The appropriate formula is :

$$L = 2l\left(\ln\left(1/D + \sqrt{1 + \frac{l^2}{D^2}}\right) - \sqrt{1 + \frac{D^2}{l^2}} + \frac{D}{l}\right) \qquad (2.1)$$

The above formula shows that the inductance is dependent upon the length of the line as well as D, which represents the geometric mean distance as outlined by Maxwell[14]. The formula used to calculate the Geometrical Mean Distance, D, of a rectangle is given by :

$$GMD = 0.2235\,(W + T) \tag{2.2}$$

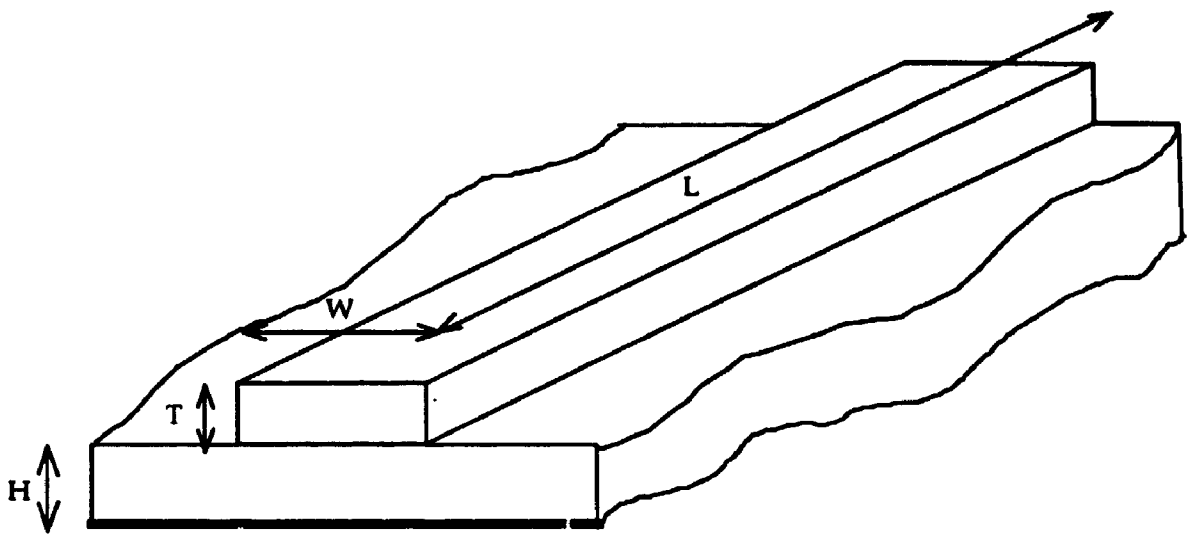

Figure 2.6 Structure of Microstrip Line with Dimensions

Hence, the total self inductance of the square spiral is calculated by summing the individual self inductances of each segment. Assuming the spiral has n segments, we have :

$$L_{self} = \sum_{i=1}^{n} M_{i,i} \tag{2.3}$$

The above formula is frequency-independent. In fact, the internal inductance of the line does change with frequency but since it is much less than the external inductance term, the effect is negligible. Formula 2.1 is general, and is also used to calculate the mutual inductance between two parallel lines of rectangular cross section. The D for this case

is given by the formula

$$D = GMD = \exp\left(\ln D_{cent} - \left(\frac{1}{12\left(\frac{D_{cent}}{W}\right)^2} + \frac{1}{60\left(\frac{D_{cent}}{W}\right)^4} + \frac{1}{168\left(\frac{D_{cent}}{W}\right)^6}\right)\right) \tag{2.4}$$

Here D_{cent} is the distance between the centers of the two parallel lines. Two different cases of mutual inductance can occur between any two lines, depending on their position relative to each other. These are shown in Figure 2.7. In case 1 the mutual inductance between the two lines must be calculated carefully in order to take into account the fact that they are not of the same length. The equation for the mutual inductance in case 1 is :

$$M = \frac{M(l_2 + l_3) - M(l_3) + M(l_2 + l_4) - M(l_4)}{2} \tag{2.5}$$

The equation for case 2 is :

$$M = \frac{M(l_1) - M(l_3) + M(l_2 + l_4) - M(l_4)}{2} \tag{2.6}$$

If the mutual inductance in case 2 is taken to be that of a length of line having the same overlap with the adjacent line (ie. $L=L_2$), the error can become significant in certain cases where L_3 and L_4 are large relative to L_2. Hence, it is important to use the above formulas properly, or else errors can accumulate in the analysis.

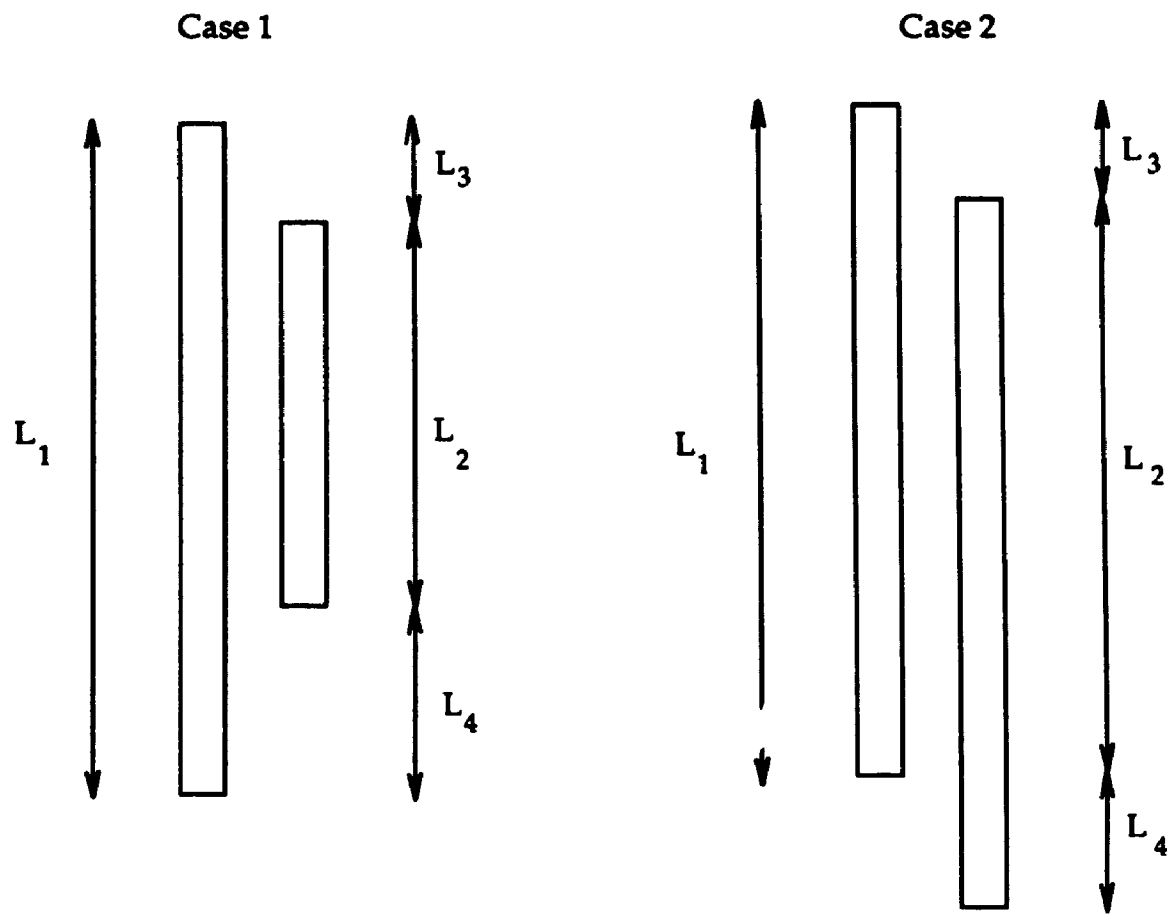

Figure 2.7 The Two Different Cases for Coupled Lines in an Inductor

Hence, the total mutual inductance presented by a square spiral inductor can be written as :

$$L_{mut} = \sum_{i=1}^{n} \sum_{j=1}^{n} M_{i,j} \tag{2.7}$$

The above equation shows that the mutual inductance between any two parallel lines must be added twice; once for the current flowing in line i inducing a voltage in line j, and the reverse, for the current flowing in line j inducing the same voltage in line i.

As the spacing between the two lines increases, the geometric mean

distance is given almost by the actual physical distance between the line centers. Also, equation 2.1 only calculates the absolute value of the mutual inductance. The sign is given from the direction of current flow in the spiral. For instance, in figure 2.5, the mutual inductance $M_{1,3}$ is negative, whereas $M_{1,5}$ is positive. The mutual inductance of an inductor is typically 10 to 20 % of the total inductance of an inductor and therefore cannot be ignored.

It is interesting to note here that a square spiral of exactly one turn has less inductance than that of a straight line of the same length, due to the presence of the negative mutual inductances between opposite sides of the square spiral.

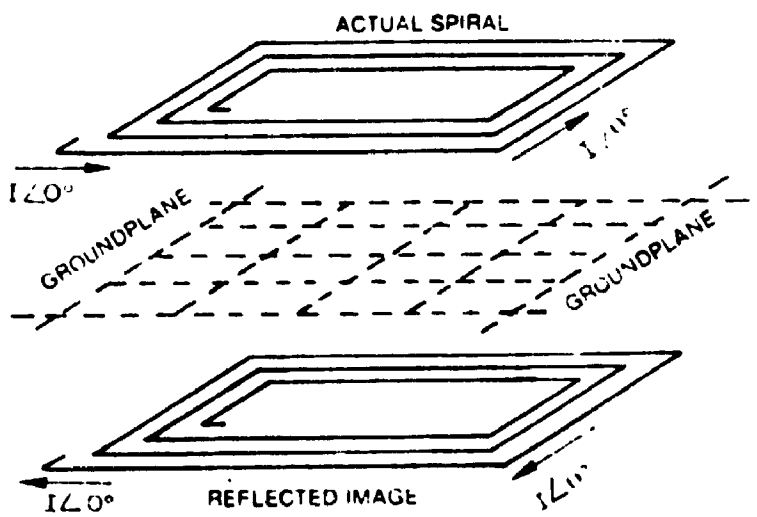

Figure 2.8 Image Spiral Produced as a Reflection in Ground Plane

Once all of the self and mutual inductances are calculated, the total inductance is known as long as the inductor has no ground plane beneath it. However, since microstrip has a ground plane, the coupling to the image inductor must also be calculated. This inductance can become significant if the distance of the inductor from the ground plane is small. Figure 2.8 shows an equivalent image inductor, the same distance from the ground plane but on the other side, which represents the ground plane effect. This effect, which lowers the total inductance, can best be reduced

by fabricating the inductor on a thicker substrate. In this way the parasitic capacitances associated with the inductor will also be reduced. The total image inductance of the inductor is therefore given by :

$$L_{image} = \sum_{i=1}^{n} \sum_{j_{image}=1}^{n} M_{i,j_{image}} \tag{2.8}$$

where j_{image} is the appropriate segment number on the imaginary underside spiral. The mutual inductance between the topside coil and the bottomside coil is not counted twice, because only the effect of the image inductor on the actual inductor is sought.

The three different inductances have to be summed and then the low frequency inductance of the spiral can be determined.

$$L_{total,stat} = L_{self} + L_{mut} + L_{image} \tag{2.9}$$

The above equation can only give the inductance with good accuracy up to several GigaHertz. In order to find the inductance to the first resonant frequency, the change in inductance with frequency must also be calculated.

The method used here to achieve this is an approximate method based on the phase shift of the current around the coil. At very low frequencies the phase shift around the coil is negligible and hence the mutual inductances add almost linearly. However, as the phase shift around the coil increases with frequency, the mutual inductances add vectorially to create a net mutual inductance that is smaller than for the static case. The self inductance of each segment is not affected by changes in frequency and therefore remains constant. Figure 2.9 illustrates how the mutual inductance vectors are added to decrease the overall inductance.

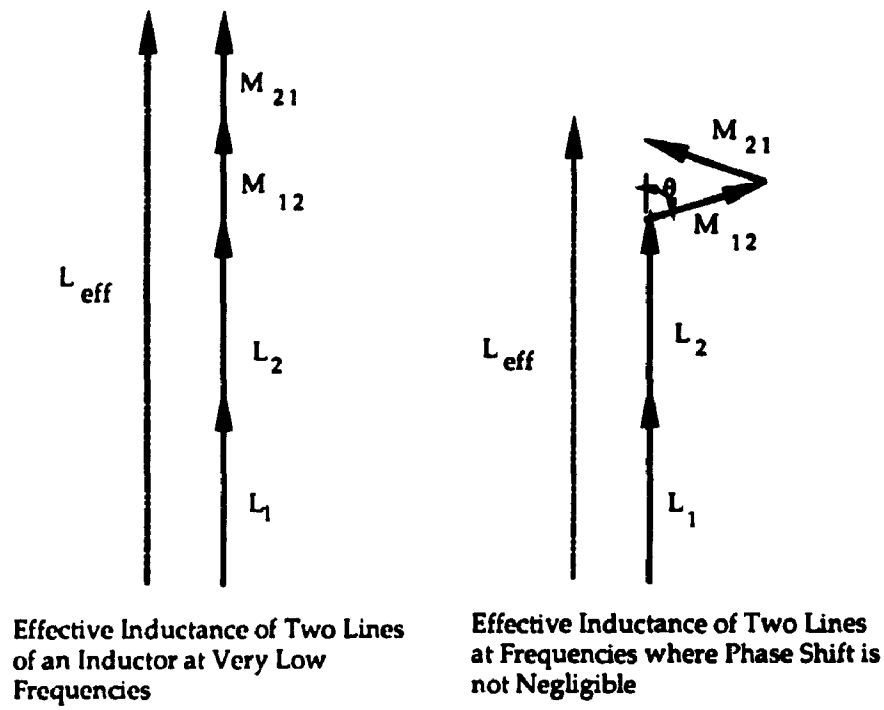

Figure 2.9 The Effect of Phase Shift Around the Coil on Effective Inductance

The resultant mutual inductance, including the effects of the phase shift of the current around the coil between the centers of the two segments concerned, is given by $M_{equivalent} = M_{i,j} \cos(\Delta\theta)$[15]. The phase shift around the coil is calculated according to the formula given for the wavelength of the fundamental even mode propagating on the microstrip line. This formula also calculates the phase shift at frequencies where dispersion begins to take place in the microstrip. Hence, the equations for the frequency dependent values for $L_{mut}(f)$ and $L_{image}(f)$ are given by :

$$L_{mut}(f) = \sum_{i=1}^{n} \sum_{j=1}^{n} M_{i,j} \cos(\Delta\theta_{i,j}(f)) \qquad (2.10)$$

$$L_{image}(f) = \sum_{i=1}^{n} \sum_{j_{image}=1}^{n} M_{i,j}\cos(\Delta\theta_{i,j}(f)) \qquad (2.11)$$

Therefore the final value of L containing the frequency-independent self inductance, L_{self}, as well as the frequency-dependent parameters $L_{mut}(f)$ and $L_{image}(f)$, is given by :

$$L = L_{self} + L_{mut}(f) + L_{image}(f) \qquad (2.12)$$

2.3.2 Model Capacitance Analysis

The calculation of the capacitance parameters C_{01}, C_{02}, and C_f is discussed next. C_{01} and C_{02} represent the total capacitance to ground of the outer and inner halves, of the spiral respectively. C_f is the total value of the feedback capacitance between the turns of the inductor. These values are calculated according to the closed-form equations outlined by J.I. Smith in his paper, "The Even- and Odd-Mode Capacitance Parameters for Coupled Lines in Suspended Substrate"[16]. The values of the capacitances to ground and the interline capacitances can then be calculated from the even- and odd-mode capacitances of the microstrip lines. The even mode capacitance for a segment will give the value of its capacitance to ground.

$$C_g = C_e \qquad (2.13)$$

This capacitance is larger for the outermost and innermost turns of the inductor because of the absence of a neighbouring segment.

The interline capacitance is given by

$$C_m = \frac{1}{2}(C_o - C_e) \tag{2.14}$$

Conformal mapping is used in order to find the even- and odd-mode capacitances. Each of the two cases is looked at separately, and a solution is found after a number of transformations. This method assumes that the microstrip lines are infinitely thin, which is acceptable when calculating the coupling capacitances for lines in typical thin-film circuits.

The fact that the actual fabrication technique used results in a metallization thickness of 1 μm will not make a significant difference in the final values of the capacitances. Also, it is assumed that the capacities between non-neighbouring segments is negligible. This is a valid assumption which could not be made for the inductance calculations where it was discovered that mutual coupling between segments even on opposite sides of the spiral is significant.

The model developed assumes that the capacitance to ground is constant with frequency. Hence, the capacitance to ground of the various segments must be calculated and then summed to form the total capacitances to ground, C_{01} and C_{02}, as given by :

$$C_{01} = \sum_{i=1}^{n/2} C_{g_i} \tag{2.15}$$

$$C_{02} = \sum_{i=n/2}^{n} C_{g_i} \tag{2.16}$$

The parameter C_f is the one which models the coupling between the turns of the inductor. It is given as

$$C_f = \sum_{i=1}^{n-4} C_{m_i} \tag{2.17}$$

However, since the full nodal analysis approach is not taken, the actual

feedback capacitance must be calculated according to the frequency at which the inductor is to be analyzed.

At DC the capacitive coupling between parallel segments of the inductor can be assumed to be zero. However, as frequency increases there is a non-negligible phase shift around the coil which causes the effective capacitance to increase with frequency. This increase with frequency can be shown to be :

$$C_{m,eff} = C_{m_i}(1 - \cos(\Delta\theta_{1\ turn})) \tag{2.18}$$

Hence, the variation of the mutual feedback capacitance with frequency is sinusoidal.

All of the effective interline capacitances must be calculated for each frequency point and then summed together :

$$C_f(f) = \sum_{i=1}^{n-4} C_{m_i}(1-\cos(\Delta\theta_{i,i+4})) \tag{2.19}$$

2.3.3 Model Resistance Analysis

The calculation of losses for this type of passive structure is broken up into two parts : ohmic losses and dielectric losses.

The ohmic losses are due to the finite conductivity of the metal which is used as the conducting layer. At frequencies where the thickness of the conducting layer becomes approximately three times thicker than the skin depth, it can be assumed that all of the current flows only on the surface of the conductor.

It was found that the total losses of the structure could be modelled as

an equivalent resistor value in series with the previously calculated inductance element value, L. Determination of this resistance is complicated by the fact that in typical thin-film technologies, the skin depth is no longer negligible compared to the conductor thickness which is only several microns (specifically, 1 μm for the CRC fabrication facilities). Detailed numerical techniques have been developed[17], but experiments performed for this thesis have shown that the closed-form expressions given by Pettenpaul et al.[18] describe the frequency-dependent resistance sufficiently. The equations used to calculate the ohmic losses in the MHMIC structures are given by :

$$R_{ohmic} = R_{dc}\left(\frac{0.43093x_w}{1 + 0.04(w/t)^{1.19}} + \frac{1.1147 + 1.2868x_w}{1.2296 + 1.287x_w^3} + 0.0035\left(\frac{w}{t} - 1\right)^{1.8}\right) \tag{2.20}$$

for $x_w >= 2.5$, and

$$R_{ohmic} = R_{dc}\left(1 + 0.0122x_w^{(3 + 0.01x_w^2)}\right) \tag{2.21}$$

for $x_w < 2.5$,

where,

$$R_{dc} = \frac{L}{\sigma\omega t} \tag{2.22}$$

$$x_w = (2f\sigma\mu wt)^{1/2} \tag{2.23}$$

and, w = conductor width

t = conductor thickness

σ = conductor conductivity

μ = permeability of free space

ω = radian frequency

The above equations are very easily inserted into a CAD program since they are closed form equations which are fitted to published results given

by Haefner[19]. The variable x_W contains the basic $\sqrt{f}$ frequency dependence which calculates the skin effect equation present in any conductor.

If more accuracy were required for the conductor loss, a lookup table would have to be constructed from the results of numerical methods.

The tangent loss in passive structures is due to energy dissipated in rotating dipoles inside the dielectric material. For ceramic substrates, the loss tangent is significantly less than the conductor loss and can therefore be ignored with only a slight error. (It is however, included in the model for the sake of completeness). The same cannot be said for many plastic-based substrates where the loss tangent is not always negligible. .The following equation given by Gupta[20] is used to calculate the attenuation of a signal in dB/unit length:

$$\alpha_d = 27.3 \frac{\varepsilon_r (\varepsilon_{eff} - 1) \tan\delta}{\sqrt{\varepsilon_{eff}}(\varepsilon_r - 1)\lambda_0} \tag{2.24}$$

In order to change the dielectric attenuation of Equation 2.24 to an equivalent resistive loss, the following equation is used :

$$\alpha_d = 8.686 \frac{R}{2Z_0} \tag{2.25}$$

Therefore the R in the frequency dependent model of figure 2.4 is given by :

$$R = R_{ohmic} + R_{dielectric} \tag{2.26}$$

2.3.4 Other Effects Included

The corners on the square spiral inductors fabricated at CRC are

chamfered. If the corners are produced square then a large amount of additional capacitance to ground would have to be added to the final values of C_{01} and C_{02}. This capacitance arises due to the fact that there is an accumulation of charge at the corners of the bend, and more significantly at the outer corner of the bend. With chamfered outer corners the parasitic capacitances are reduced slightly. Also, there is some small amount of inductance added to the circuit at each corner due to the interruption of current flow there. Hence, the model used to take into account the corner bends can be seen below.

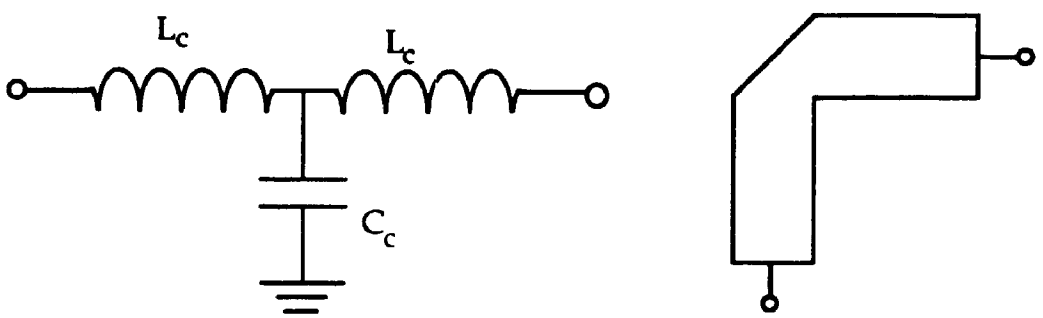

Figure 2.10 Model for Chamfered Microstrip Bend

The equations developed by M. Kirschning et al.[21] are used to obtain the values of L_c and C_c. They are given by the following equations :

$$L_c/nH = 0.44\ (H/mm)\ (1 - 1.062e^{(-0.177\ (W/H)^{0.947})}) \tag{2.27}$$

$$C_c/pF = 0.001\ ((3.93\varepsilon_r + 0.62)\ (W/H)^2 + (7.6\varepsilon_r + 3.80)\ (W/H)) \tag{2.28}$$

Table 2.2 illustrates some typical values obtained for L_c and C_c.

Table 2.2

Corner Chamfer Discontinuity Values as a Function of W/H with ε_r=9.9 and H=254 μm

W/H	L_c (pH)	C_c (fF)
10/254	-6.0	0.81
20/254	-5.1	1.64
30/254	-4.2	2.51
50/254	-2.5	4.34
70/254	-1	6.30
100/254	1	9.46

It can be seen that for small values of W/H, the discontinuity inductance, L_c, is negative which means that the line segments leading into and out of the corner are effectively shorter than their physical lengths. This will happen with all of the structures studied since they all have values of W/H near 10/254 or 20/254. The values for the discontinuity capacitance, C_c, are seen to increase with line width, if the substrate height is kept constant.

Hence, using Equations 2.27 and 2.28, the total additional inductance of all the corner bends is summed, and added to the final value of L. Similarly, the values of C_c are added to the final values of C_{01} and C_{02}.

The inductor is modeled in this manner all the way to the innermost segment of the square inductor. The airbridge which leads out of the spiral is modelled as an equivalent length of transmission line. Although the airbridge couples capacitively to the segments beneath it, ignoring this did not significantly affect the final calculated S parameters of the inductor in the frequency range tested.

It can be calculated that for the typical widths of microstrip lines used with the inductors, dispersion starts to occur from 10 to 15 GHz. This is

taken into account in the frequency-dependent calculations involved with the model by using the standard equation for wavelength on a microstrip line which includes dispersion effects.

2.4 Computer Program Integration

The above procedure is very convenient to implement in a computer-aided design package. The method outlined was written as a FORTRAN 77 program which calculated the Y matrix of the equivalent model of Figure 2.4. (This calculation can be seen in Appendix I). The program was then installed in the microwave CAD package SuperCompact[22]. It can then be used in the same manner as any other model in the program. The number of turns, track width, track spacing, substrate thickness, conductor thickness, horizontal and vertical lengths, and resistivity relative to gold have to be indicated, and the S-parameters of the inductor are thereafter calculated. For example, the following statement can be inserted into a SuperCompact program in order to analyze an inductor:

```
SSPI  TUR=2.50 LN1=300 LN2=300 WID=20 SPA=20 HEI=254
+     THI=1 RHO=2.0 TLO=0.0002 EPS=9.9
```

The above statement will provide the S parameters for a square spiral inductor (SSPI) with the following characteristics:

TUR=2.50	; 2-1/2 turn inductor
LN1=300	; overall horizontal length of 300μm
LN2=300	; overall vertical length of 300μm
WID=20	; track width of 20μm
SPA=20	; track spacing of 20μm
HEI=254	; substrate height of 254um (here, 10 mil)
THI=1	; conductor thickness of 1μm
RHO=2.0	; resistivity of conductor is twice that of gold

TLO=0.0002 ; loss tangent of substrate is 0.0002

EPS=9.9 ; relative permittivity of substrate (here, Alumina)

The sample inductor of Figure 2.11 shows the various dimensions which are required to use the user-defined SSPI model.

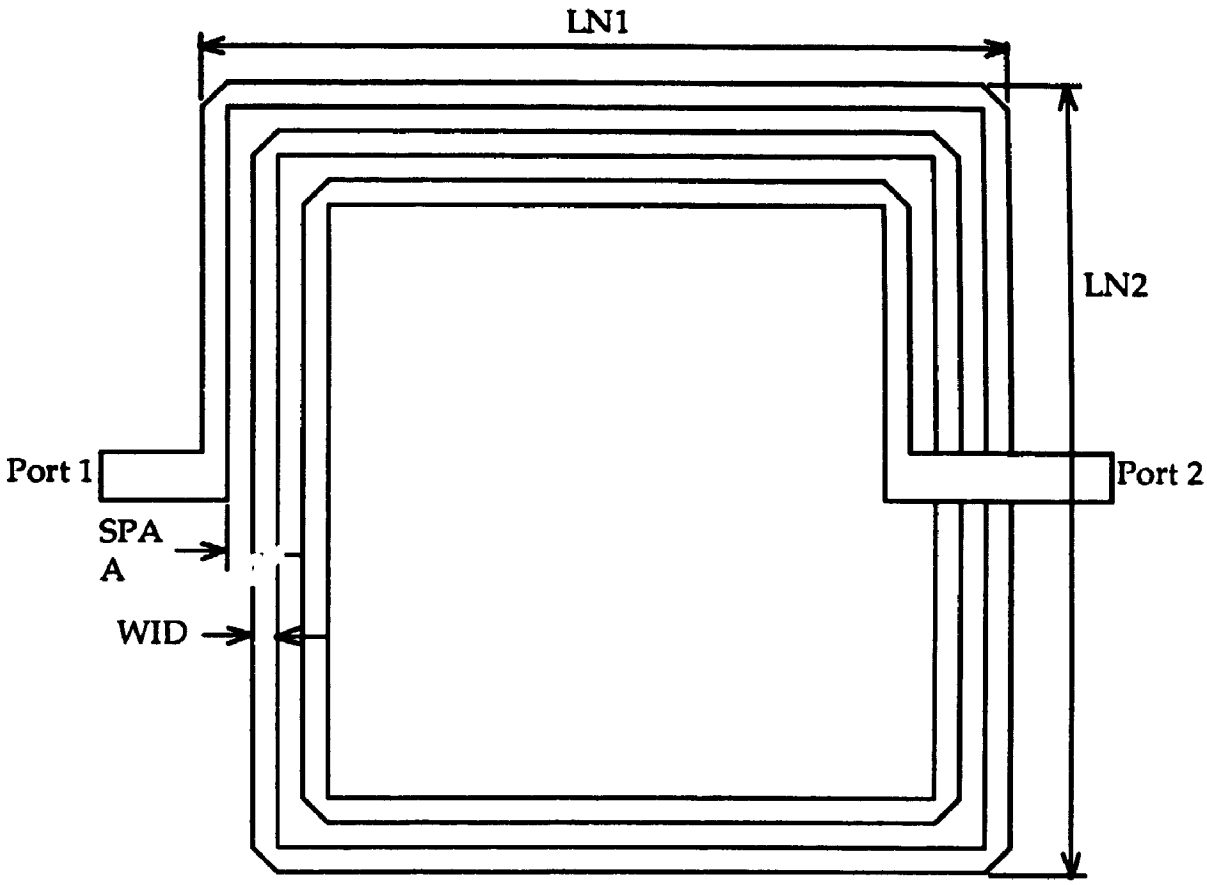

Figure 2.11 Sample Spiral Inductor with Dimensions Shown

2.5 Results and Discussion

Some of the results obtained for the inductors will be discussed in this section of the thesis. The model derived here was checked with many

different inductor sizes and found to be quite accurate up to at least the resonant frequencies of the inductors.

The measurement setup used for all of the structures in this thesis is shown in Figure 2.12. It consists of an HP8510 network analyzer whose two measurement ports are connected to a Rucker & Kolls Model 1032 Automatic Wafer Prober. The calibration method used is the standard open-short-through-50Ω load technique. The standards for the calibration are taken from a sapphire substrate. When the calibration is being performed the reference plane is taken at the level of the coplanar probe tips. The substrate which is under test is placed on the platter in the wafer prober, and then the coplanar ground-signal-ground probes are applied to the specific circuit which is being measured. The S-parameters are transferred from the network analyzer onto the hard disk of the HP8510 computer which is also connected to the network analyzer.

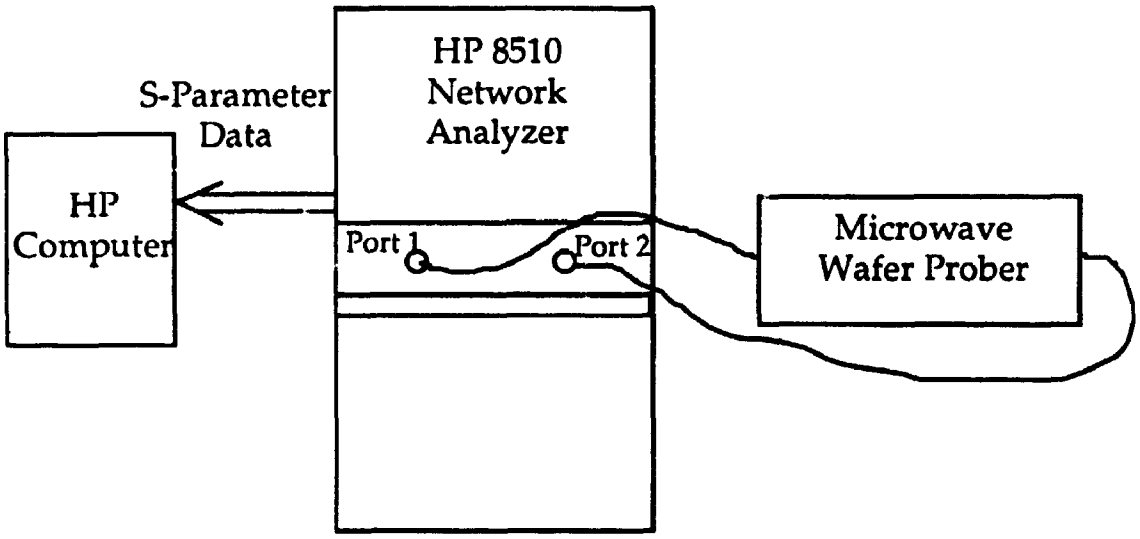

Figure 2.12 Measurement Setup

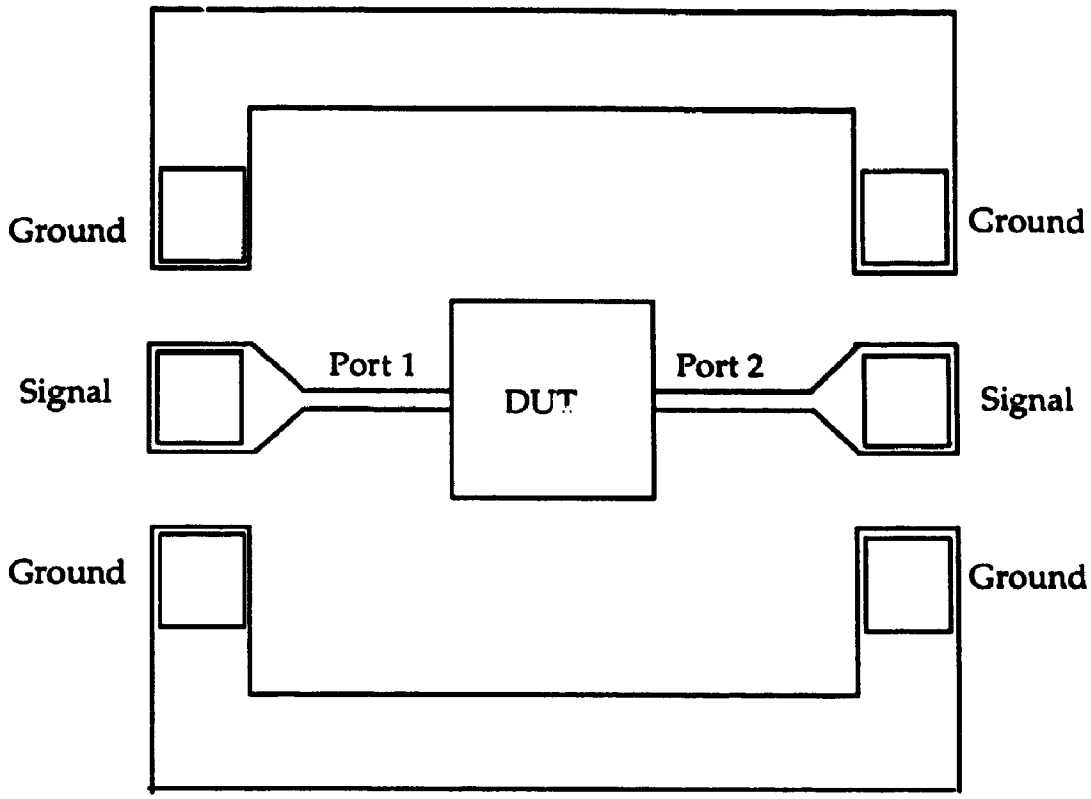

Figure 2.13 Layout Used for Coplanar Measurement

In Figure 2.13, the layout which is used for all of the passive devices can be viewed. The setup is seen to be tailored to the specialized ground-signal-ground probes which are attached to the wafer prober. In order to make electrical contact between the input and output ground tips, ground strips are used, which can be seen at the top and bottom of figure 2.13.

The results for a 1-1/2 turn inductor on 0.010" alumina with a 20 μm line width and 10 μm line spacing can be seen in figure 2.14 This inductor has lengths LN1 and LN2 of 230 μm. The results of the model element values for this case can be seen in Table 2.3 and the S-parameters are compared to measurements in figure 2.14.

Table 2.3
1-1/2 Turn Inductor Model Element Values
at Different Frequencies

f(GHz)	L(nH)	R(Ω)	C_{01}(fF)	C_{02}(fF)	C_f(fF)
1	0.78	1.17	24.1	17.3	.007
2	0.78	1.32	24.1	17.3	.028
3	0.78	1.53	24.1	17.3	.064
4	0.78	1.55	24.1	17.3	0.11
5	0.78	1.58	24.1	17.3	0.18
6	0.78	1.62	24.1	17.3	0.25
7	0.78	1.66	24.1	17.3	0.35
8	0.78	1.69	24.1	17.3	0.45
9	0.78	1.73	24.1	17.3	0.57
10	0.78	1.77	24.1	17.3	0.72
11	0.78	1.81	24.1	17.3	0.85
12	0.78	1.84	24.1	17.3	1.01
13	0.78	1.88	24.1	17.3	1.18
14	0.78	1.91	24.1	17.3	1.36
15	0.77	1.95	24.1	17.3	1.56
16	0.77	1.98	24.1	17.3	1.77
17	0.77	2.01	24.1	17.3	2.00
18	0.77	2.04	24.1	17.3	2.23
19	0.77	2.07	24.1	17.3	2.48
20	0.77	2.10	24.1	17.3	2.74

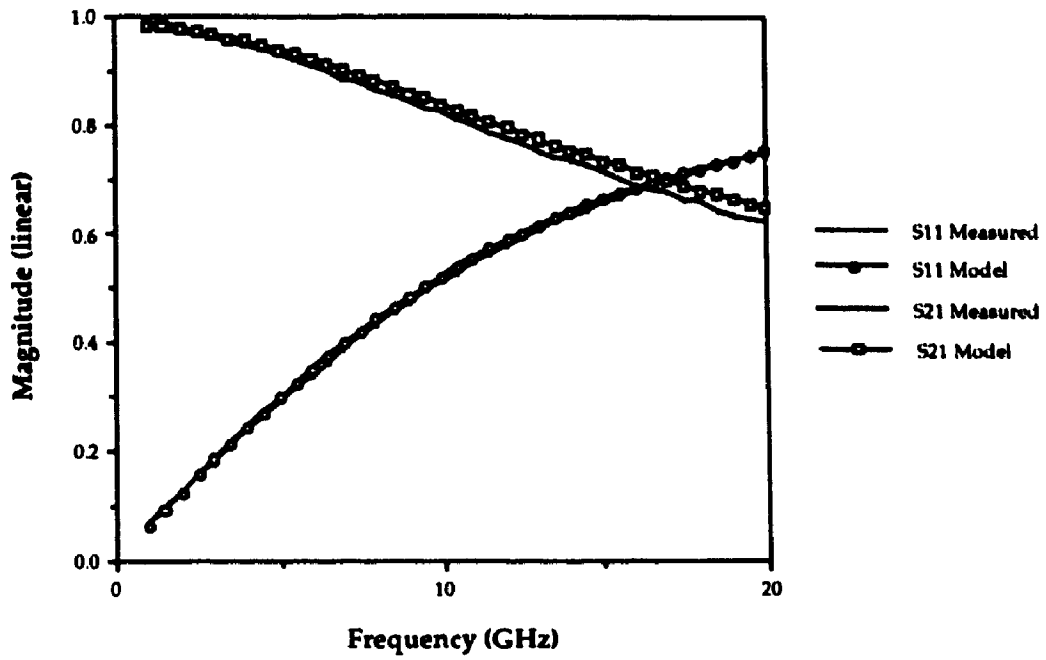

Figure 2.14a Magnitude Response of a 1-1/2 Turn Inductor

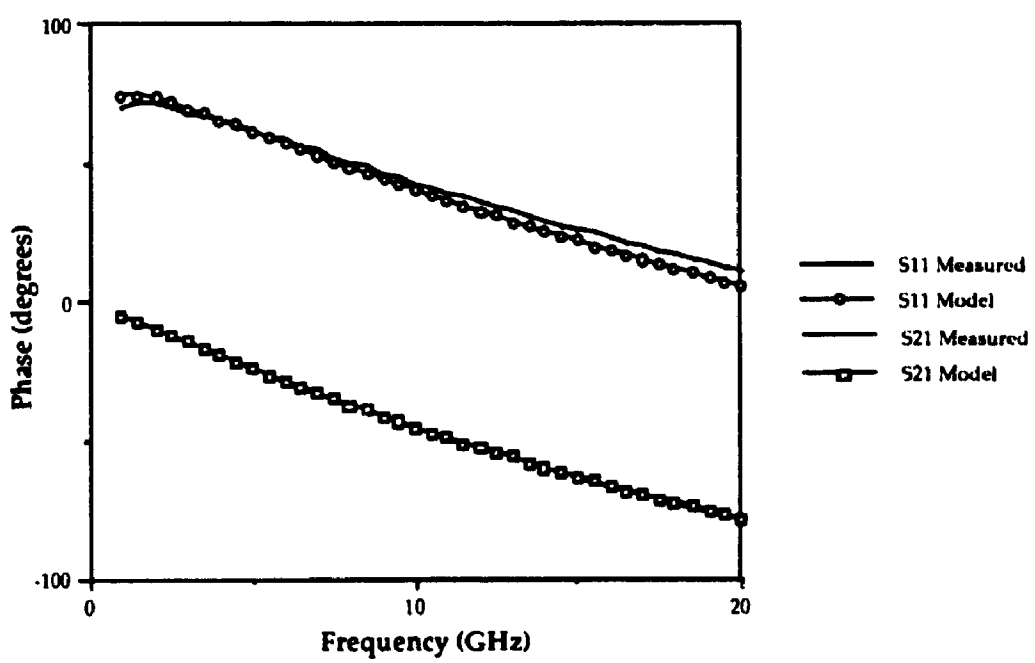

Figure 2.14b Phase Response of a 1-1/2 turn Inductor

The results for a 2-1/2 turn inductor on the same substrate with LN1 and LN2 being 345 μm and 315 μm respectively, and WID and SPA being 20 μm and 10 μm respectively is shown in Figure 2.15.

By observing the figures for the two different inductors it can be noted that the inductor with 2-1/2 turns resonates at approximately 13 GHz, whereas the inductor with only 1-1/2 turns resonates at a frequency above 20 GHz. This points out an important property of the inductors. The larger the inductance value desired, the smaller its useful frequency range. This can become very important when designing microwave circuits at K-band and above. Also, the response of the inductor with more turns is not predicted as accurately as that with fewer turns. The reason for this is that the inductor with the larger overall dimensions is much closer to the coplanar ground lines than the smaller inductor. Due to this proximity effect the inductor becomes affected by the ground plane metallization.

For most of the inductors measured, the model could predict the resonant frequency of the structure to within a GigaHertz. Predicting this frequency is an important benchmark for the validity of a passive microwave element model.

The results for an inductor, having 3-1/2 turns, overall horizontal and vertical lengths of 510 μm, track width of 20 μm, and track spacing of 10 μm, on 0.010" alumina, can be seen in Figure 2.16. As well, for this inductor the model element values are given in Table 2.4.

This inductor has a fairly large inductance of 7 nH at low frequency. However, as can be seen from the measured and modeled results, the inductor begins to resonate at a much lower frequency than the small inductor. Above 10 GHz the insertion loss can be seen to deviate from the predicted model response. This problem is believed to stem from calibration inaccuracies of the microwave prober which cause the measured results to show an internal resonance in the structure. Observing the phase from 10 to 15 GHz, an annoying dip can be seen in the curve, which is due to the same resonance.

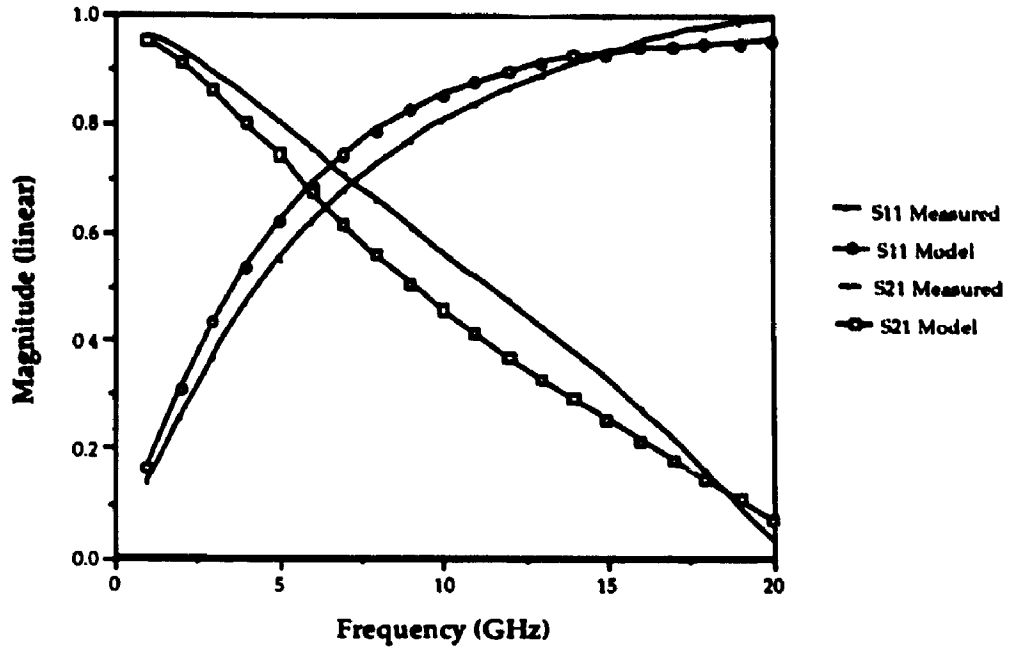

Figure 2.15a Magnitude Response of a 2-1/2 Turn Inductor

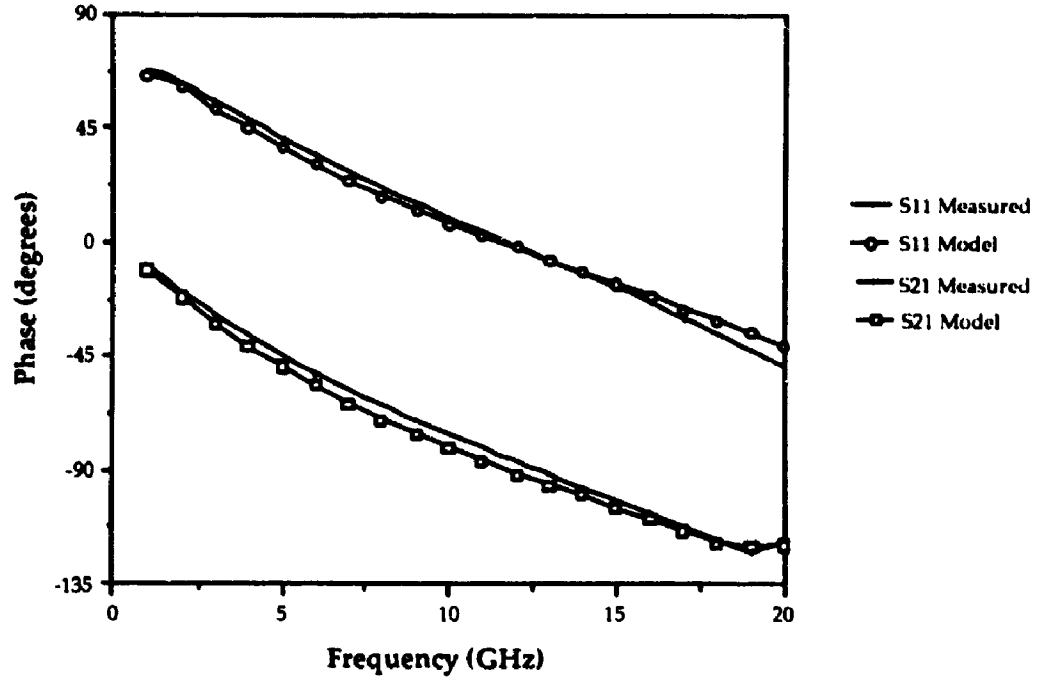

Figure 2.15b Phase Response of a 2-1/2 Turn Inductor

Table 2.4

3-1/2 Turn Inductor Model Element Values
at Different Frequencies

f(GHz)	L(nH)	R(Ω)	C_{01}(fF)	C_{02}(fF)	C_f(fF)
1	6.72	7.01	91.2	73.4	0.62
2	6.67	7.84	91.2	73.4	2.48
3	6.57	8.96	91.2	73.4	5.57
4	6.46	8.94	91.2	73.4	9.86
5	6.22	9.23	91.2	73.4	18.5
6	6.13	9.35	91.2	73.4	25.7
7	5.94	9.58	91.2	73.4	29.7
8	5.73	9.81	91.2	73.4	38.5
9	5.51	10.0	91.2	73.4	48.3
10	5.29	10.3	91.2	73.4	59.0
11	5.07	10.5	91.2	73.4	70.6
12	4.85	10.7	91.2	73.4	83.0
13	4.64	10.9	91.2	73.4	96.1
14	4.43	11.1	91.2	73.4	110
15	4.25	11.3	91.2	73.4	124
16	4.08	11.5	91.2	73.4	139
17	3.92	11.7	91.2	73.4	154
18	3.78	11.9	91.2	73.4	170
19	3.66	12.1	91.2	73.4	185
20	3.56	12.2	91.2	73.4	201

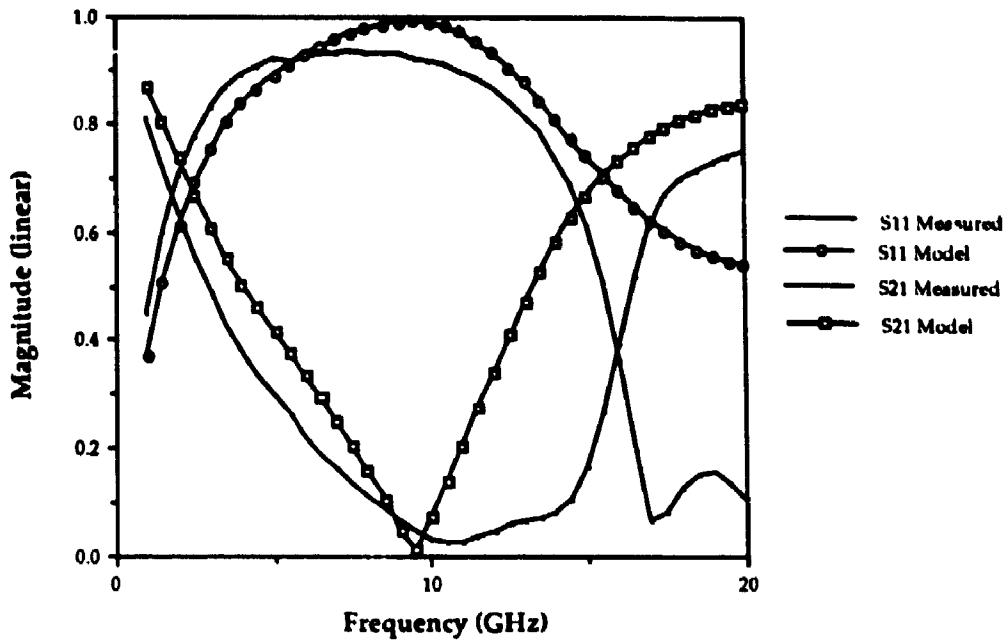

Figure 2.16a Magnitude Response of a 3-1/2 Turn Inductor

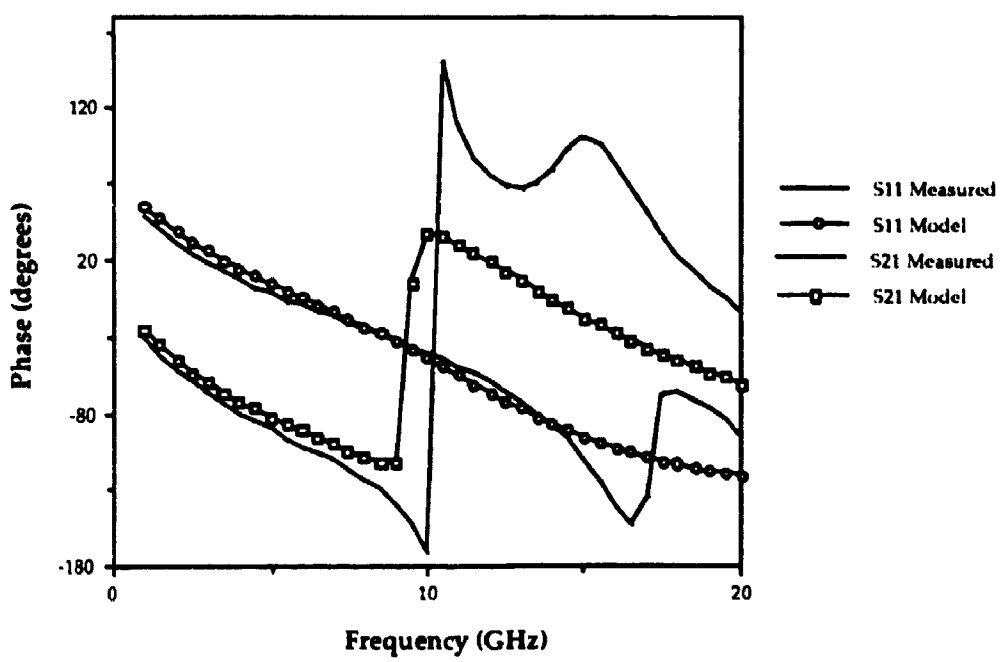

Figure 2.16b Phase Response of a 3-1/2 Turn Inductor

2.5.1 General Inductor Optimization

Once the methodology to analyze an arbitrary square spiral inductor was completed, a study was carried out to optimize the desired performance of the inductor while keeping the parasitics as low as possible.

It was discovered that for a given working area, the inductance could be maximized by keeping the spacing between the lines quite tight, but not so small that current crowding began to become significant. A good initial value is to make the track width of the inductor equal to its track spacing. Further, one must be careful not to make too many turns in the given area because the increase in inductance becomes negligible while the overall longer length of line produces more resistive losses in the component which lowers its quality factor.

Figure 2.17 below shows the theoretical results for an inductor which had to be built in an area of 500 μm x 500 μm, have a line width of 10μm, a substrate height of 0.010" and a substrate permittivity of 9.9 (alumina). It can be seen that the smaller the spacing between the lines, the greater the DC inductance of the structure. Also, the inductance increases with the number of turns, but the relationship is not linear. The same pattern is seen for the spirals layed out on the larger areas of 750 μm x 750 μm and 1000 μm x 1000 μm. From all three graphs it can be seen that when the number of turns is less than 2-1/2, decreasing the track spacing does not increase the overall inductance significantly. Hence, for these cases it would actually be better to keep larger spaces in order to avoid parasitics.

From the analysis of many inductor shapes and sizes it was discovered that the larger the inductance desired, the smaller the operating bandwidth of the inductor due to the fact that the resonant frequency is reached much sooner.

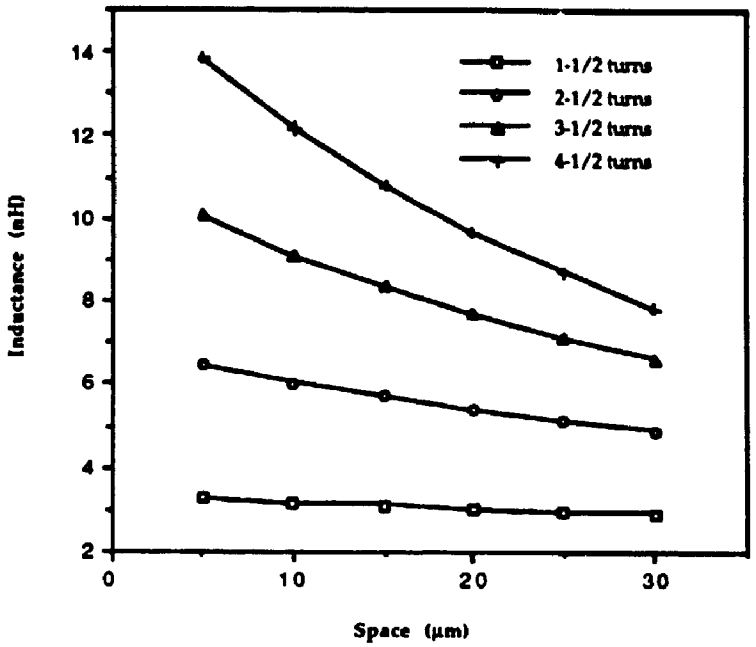

Figure 2.17 Inductance of 500 µm Square Spiral with 10 µm Line Width

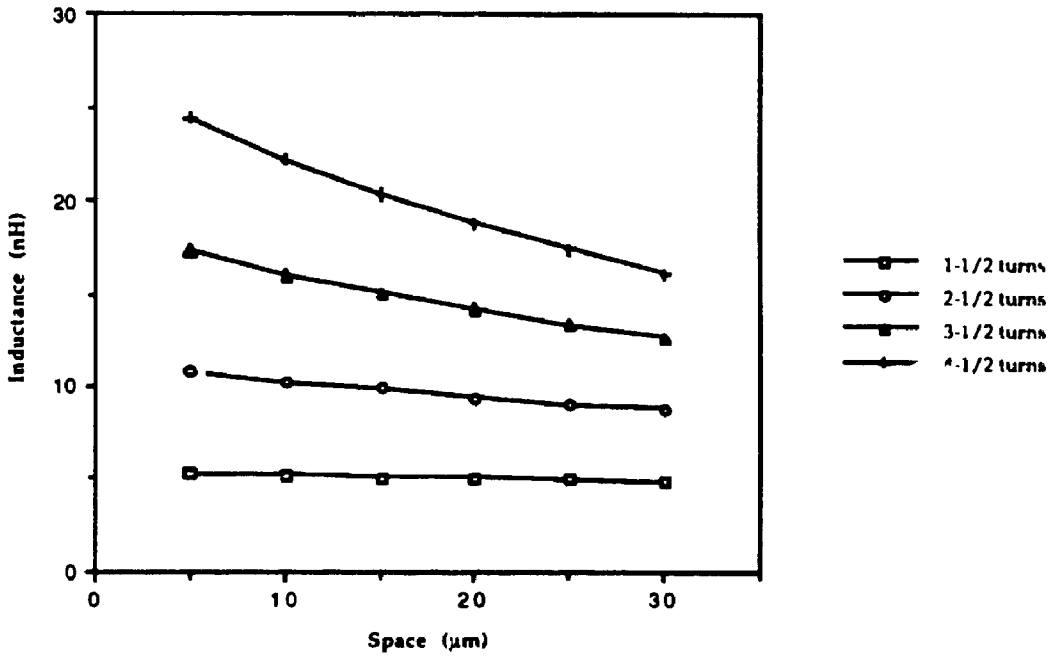

Figure 2.18 Inductance of 750 µm Square Spiral with 10 µm LineWidth

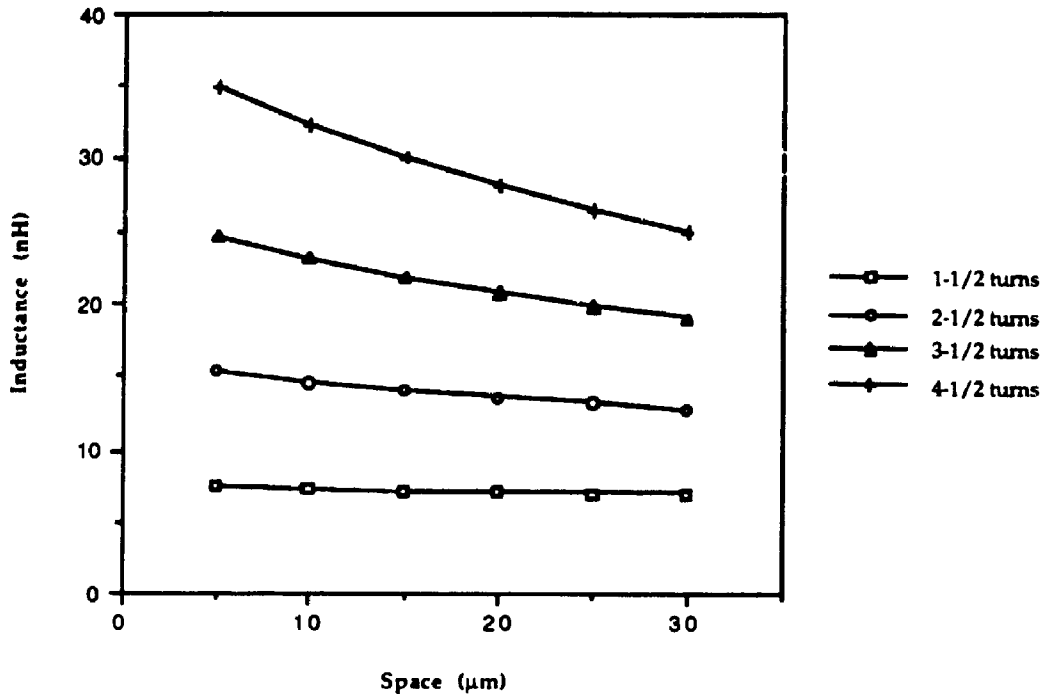

Figure 2.19 Inductance of 1000 μm Square Spiral with 10 μm Line Width

In Figure 2.19 it can be noticed that for the 1-1/2 turn inductor, the inductance decreases only very slightly as the spacing between the lines increases from 5 μm to 30 μm. Hence, in this case it would be better to fabricate the inductor with a 30 μm track space in order to decrease the parasitic coupling between the lines. Also, since the lines are spaced further apart, the resistance equations provided by Pettenpaul will have a slightly better validity.

2.6 Delay Lines

2.6.1 Introduction

A delay line is any structure, whether active or passive, which provides a certain through delay time for a signal propagating through it. The delay through the structure is calculated according to :

$$t_{delay} = \frac{\partial\theta}{\partial\omega} \tag{2.29}$$

The previously modeled inductors were used, along with thin-film capacitors, in order to design various delay lines. The delay lines which were manufactured at the CRC laboratory potentially have many uses. One is to provide the required time delays in a patch antenna array in order to produce a certain power pattern. The types of delay lines designed here are basically low pass filters which produce a certain time delay in the passband. The filter's low frequency analogy would be that of an LC filter with series L sections and parallel C sections to ground. The general structure of the the delay line can be seen in Figure 2.20. Low pass filters were designed with the objective of producing 250 ps and 500 ps delay times from 0.1 GHz to 3 GHz. The thin-film capacitors were modeled using the TFC model available in TouchStone.

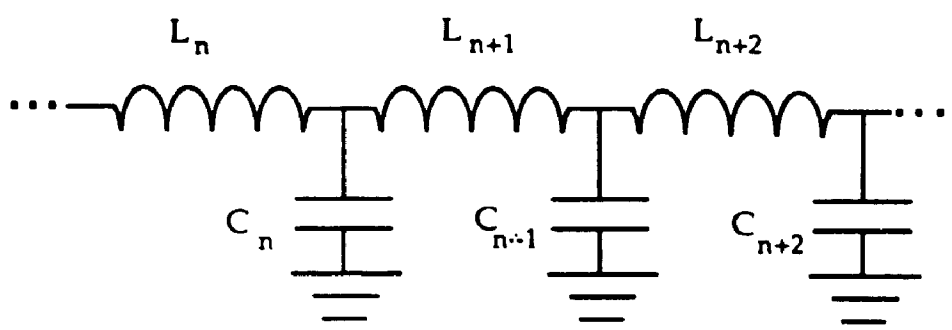

Figure 2.20 Lumped Element LC Delay Line Schematic

2.6.2 Analysis

The delay lines were optimized so that the fewest number of components would have to be used, but at the same time with an acceptable delay ripple in the passband of the structure. It was found that for the 500 ps delay line, four inductors and five capacitors were required. For the 250 ps delay line only two square spiral inductors and three thin-film capacitors were required to provide the necessary delay. Since the delay lines manufactured here were not for a specific purpose, but for general demonstration of the MHMIC passive technology, the filters were not designed as either Chebyshev, Butterworth or any other common type of filter. The elements were only optimized to obtain the required time delay with the fewest number of components.

2.6.3 Results and Discussion

The layout of a 500 ps delay line filter can be seen in Figure 2.21. This delay line is a single grounded version (ie. all of the capacitors are grounded to only one side of the coplanar ground bars) and contains four inductors and five capacitors.

Figure 2.22 which contains the second version of the delay line which was built has several of the capacitors grounded to both of the coplanar bars. Originally this was done in order to minimize the area the capacitors used, however, the circuit also worked in a much better fashion as will be discussed shortly.

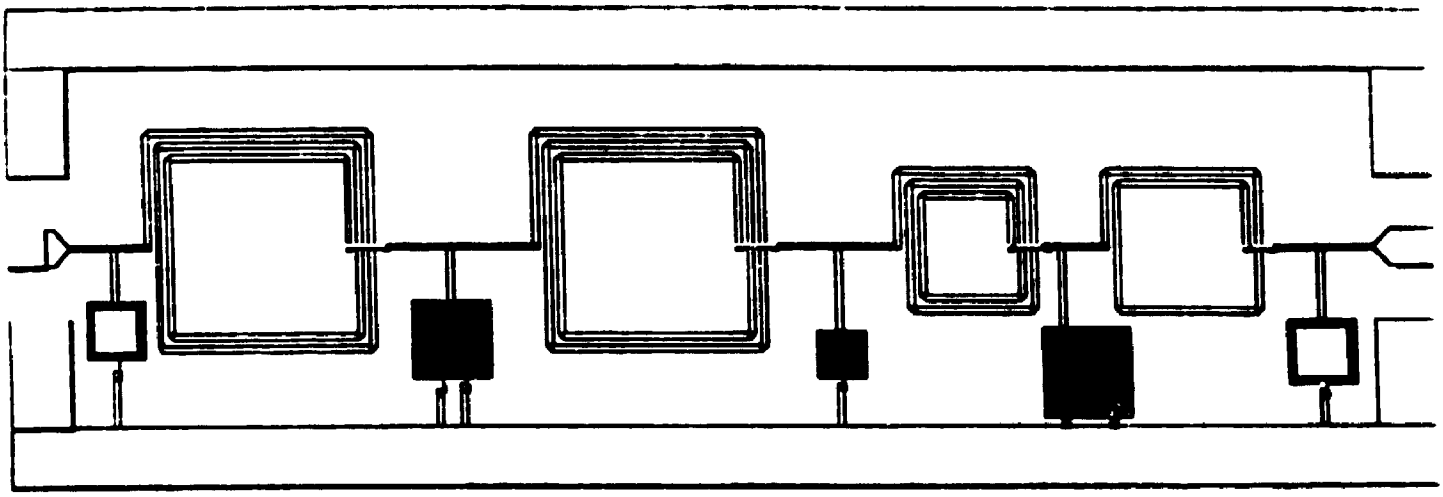

Figure 2.21 500 ps Delay Line Filter with Capacitors Grounded to only One Side

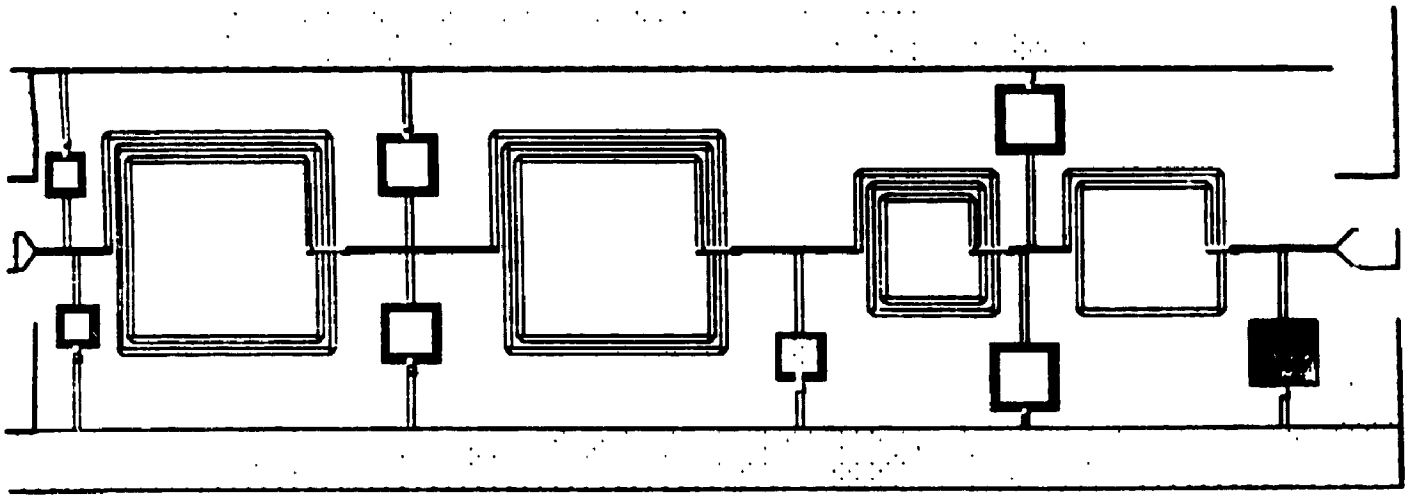

Figure 2.22 500 ps Delay Line Filter with Capacitors Grounded to Both Sides

The results for both versions of the 500 ps delay line can be seen in Figure 2.23 in which the time delay of the structure in the band from 0.1 to 3 GHz is displayed. It can be noticed that the theoretically and experimentally measured delays are quite close for both structures. Figures 2.24a and 2.24b show an interesting effect for the structure that has only been grounded to one of the bars. Annoying resonances at approximately 15 GHz and at a frequency slightly above the measurement limitations of the network analyzer, are apparent. The other design, though, has no such behaviour and shows very good agreement with the theoretically expected values over the entire frequency band. The reason that the single-grounded delay line has the resonant effect is that only one ground bar is actually physically attached to the LC filter. Hence, there is a proximity coupling effect to the bar which causes the resonance. The same coupling occurs in the dual-grounded case, however since both sides are grounded the possible resonance which could have occurred is cancelled. The current which flows in one side of the inductor has a certain direction and couples strongly to its closest ground bar, while at the same time the current which flows in the opposite side of the inductor has the opposite direction and therefore produces the opposite voltage in its ground bar. The presence of the large ground bar also has a negative effect on the transformers as will be discussed in the next chapter.

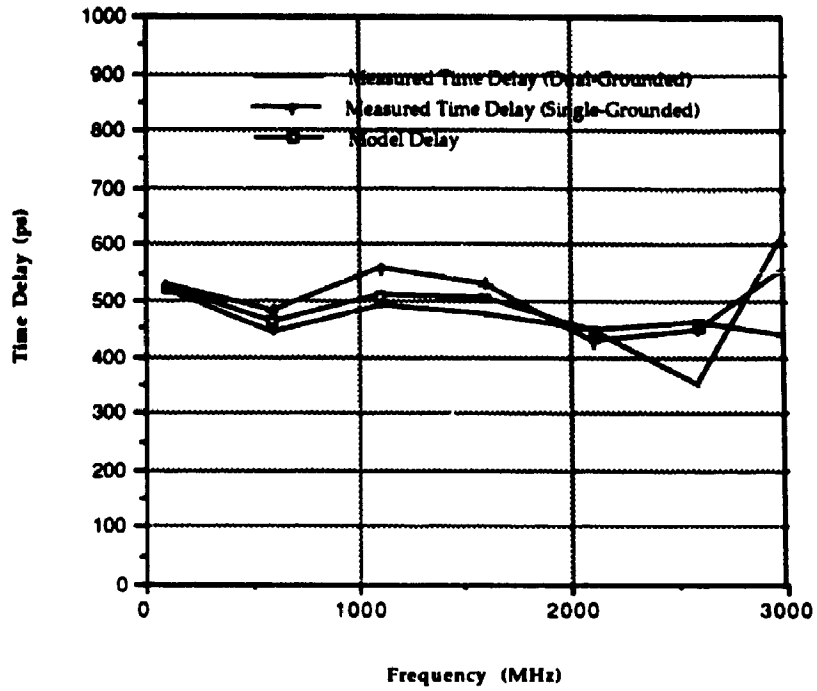

Figure 2.23 Modeled and Measured Time Delay of 500 ps Delay Line

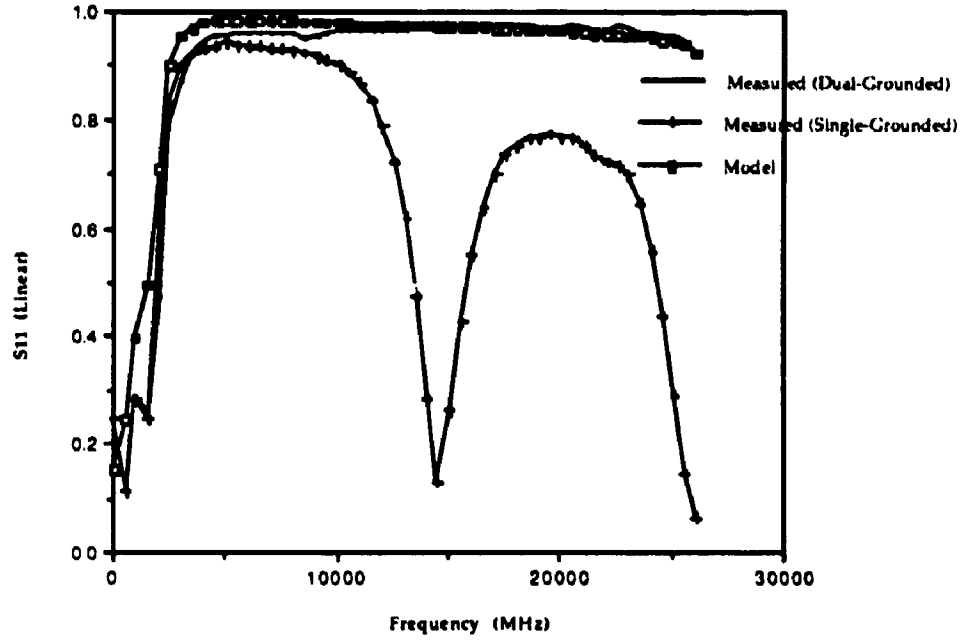

Figure 2.24a Model and Measured S11 vs Frequency for 500 ps Delay Line

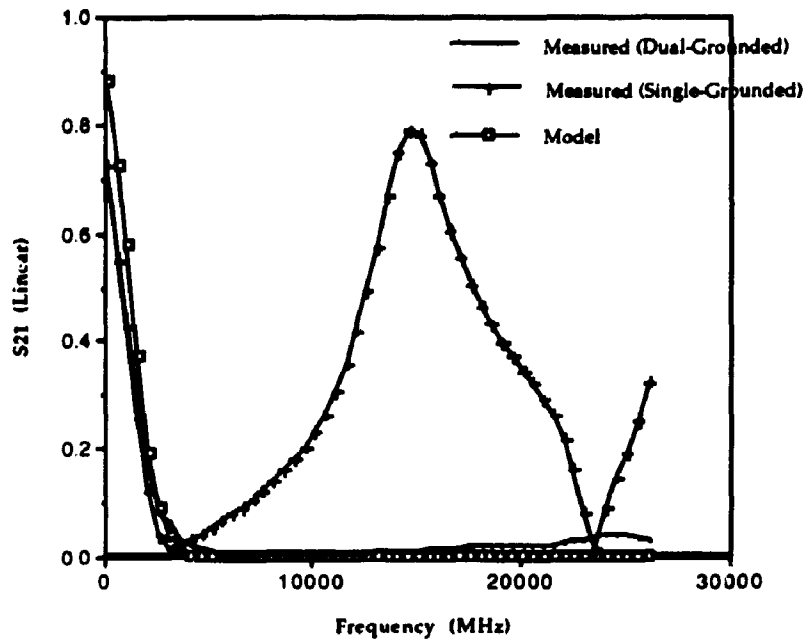

Figure 2.24b Model and Measured S21 vs Frequency for 500 ps Delay Line

The results for the 250 ps delay line can be seen in Figure 2.25. Due to the smaller time delay required, not as many inductors or capacitors are needed. The agreement between the theoretical and experimental values is seen to be quite good. When Figures 2.26a and 2.26b are observed, the resonant effect previously discussed can be seen once again.

The most important aspect that has been uncovered during the study of the delay lines is that the physical layout of the proposed circuit can have a crucial effect on the final results obtained. For example, if the capacitors in the delay lines are grounded by via holes, the delay line results would not have shown the resonances which are seen with the coplanar grounded delay lines.

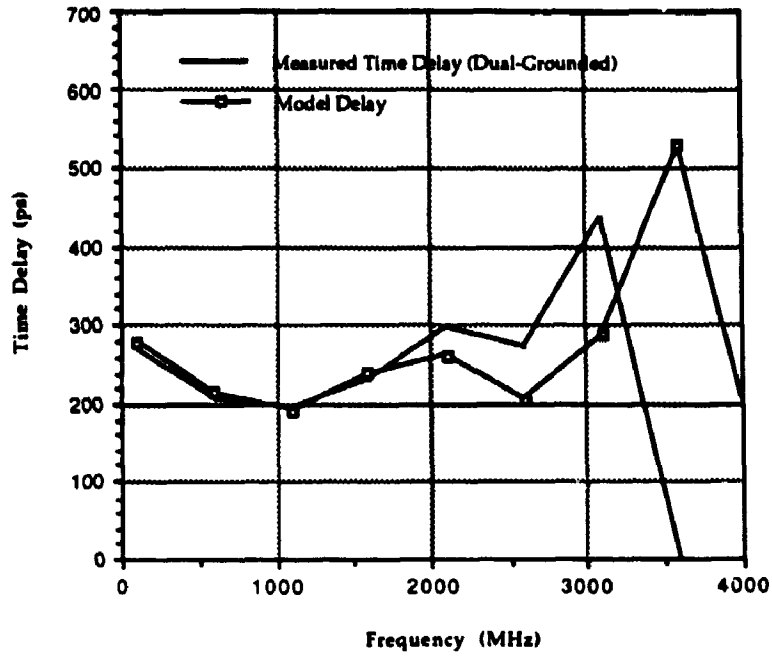

Figure 2.25 Modeled and Measured Time Delay of 250 ps Delay Line

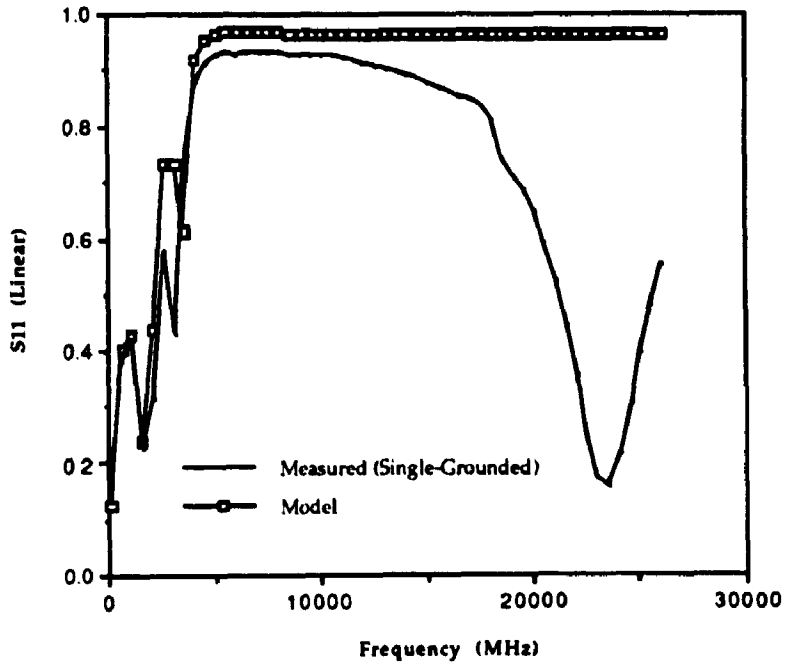

Figure 2.26a Model and Measured S11 vs Frequency for 250 ps Delay Line

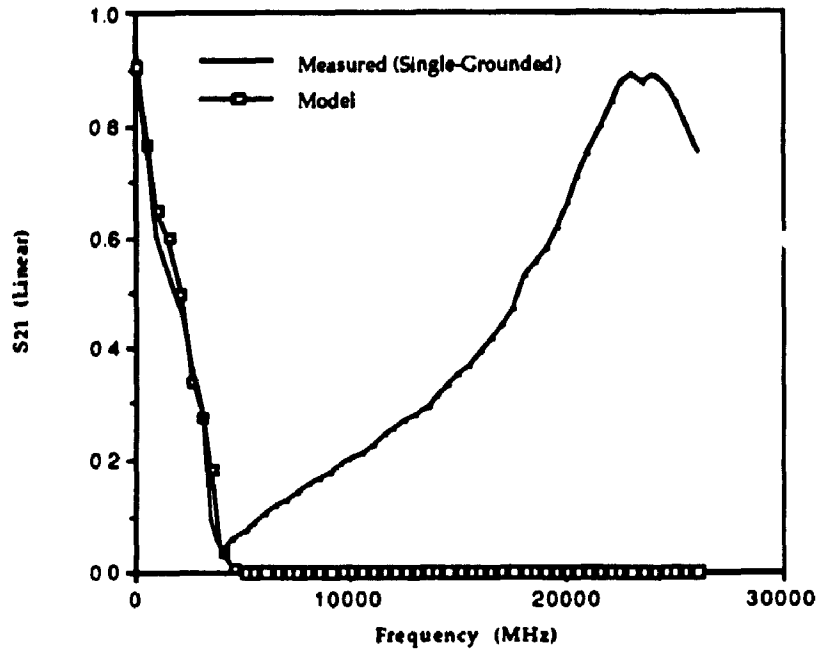

Figure 2.26b Model and Measured S21 vs Frequency for 250 ps Delay Line

3 Modeling and Analysis of Square Spiral Transfomers

3.1 Introduction

This chapter will discuss the design and analysis of MHMIC square spiral transformers fabricated on alumina and quartz substrates. There are many useful applications for these types of transformers such as impedance transforming elements in MMIC and MHMIC circuits. Also, they can be used at the input and output of pushpull amplifiers[23], or for DC bias isolation in active circuits. Ferguson et al.[24] have further extended their use to an image rejection mixer using a "wraparound" layout to conserve real estate.

In order to provide a significant coupling factor, k, between the primary and secondary coil, the layout of the transformers is that of two tightly coupled inductors. With these microwave transformers it is desirable to minimize the parasitics of the structure as much as possible, while maintaining the coupling factor close to 1.

If the transformers manufactured are to have the same characteristics as their low frequency counterparts, then they must behave in a manner as shown in Figure 3.1. This figure shows the S-parameters in Smith Chart form for three ideal transformers which all have primary and secondary inductances of 1 nH and mutual inductances from 0.5 nH to 1.0 nH. The primary and secondary are also grounded at one end of the transformer. Curves 1 to 3 show coupling factors k, of 0.5, 0.75 and 1.0. From the curves it can be noticed that the highest possible coupling is desired. For example, if the transformer is operating at 20 GHz on curve 3, then the value of S21 can be seen to be very close to unity and the insertion phase quite small. In this situation the transformer is almost matched, as shown by the S11 curve. However, the actual transformers designed at CRC will be seen to have parameters closer to that of

transformer 1 which is quite far from ideal. Also, with capacitive and resistive effects taken into account, it will be seen that the actual transformers behave far from the ideal desired case. After an analysis and results for several transformers are presented, it will be shown how the transformers can be optimized so that they behave more ideally. In addition a method to increase the inductive coupling to the output will be described.

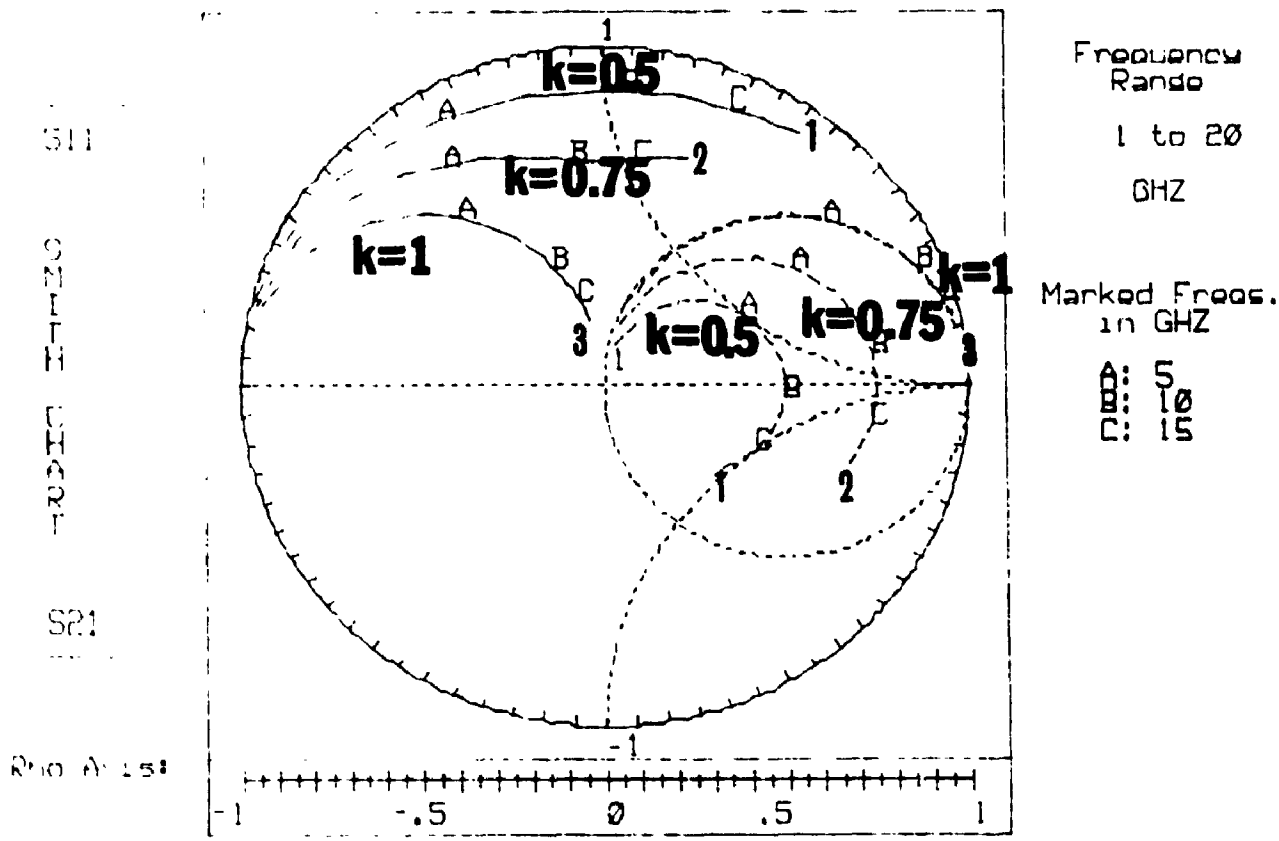

Figure 3.1 Ideal Transformer with Different Coupling Ratios

A sample transformer fabricated at CRC can be seen in Figure 3.2. Its primary as well as secondary has 2-1/4 turns. The two airbridges leading out of the primary and secondary to the ground bars can also be seen.

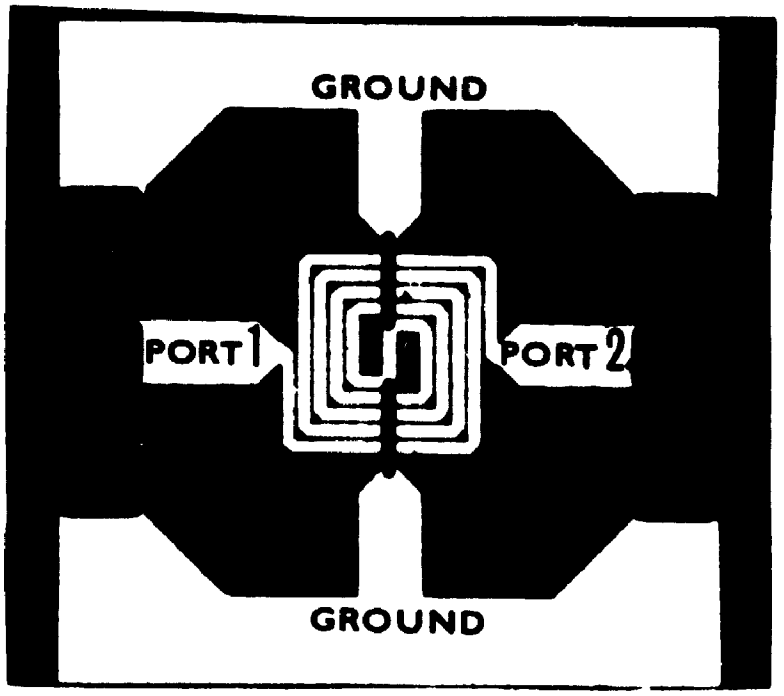

Figure 3.2 2-1/4 Turn Transformer

All of the transformers fabricated have been laid out in this configuration so that the number of turns is either 1-1/4, 2-1/4, or 3-1/4. Since the transformers are measured as 2-ports, the remaining terminals are grounded to the coplanar ground strips at either side of the transformer. The primary port, on the left, is called port 1, and the secondary port, on the right, is called port 2. The transformers are measured using a wafer prober and an 8510 HP Network Analyzer calibrated to 26.5 GHz.

3.2 Analysis

Very little study has been done in the area of transformer modeling to date. The only significant work which is available on the analysis of planar transformers is by Wiemer et al [25]. In their paper "Computer Simulation and Experimental Investigation of Square Spiral Transformers for MMIC Applications" a method is outlined to analyze square spiral transformers on GaAs substrates. The technique involves a

mutilayer-multiconductor hybrid mode transmission line analysis for the substructures present in the transformer, and a lumped element approach to calculate the coupling between the substructures. Results achieved by use of the method are good, but it requires excessive CPU time and is not easily integrated into commercial microwave CAD packages. In this chapter a method based wholly on lumped element theory is outlined which is simple to set up and easy to install as a user-defined model in either SuperCompact or Touchstone.

The analysis of the transformers is broken up into three major sections which concern the calculation of the inductive, capacitive, and resistive elements. The assumptions which were outlined previously for the inductor analysis are also applicable here. Since the method is completely general, it will be discussed first for the non-center-tapped transformers. Then it will be demonstrated how the model can be changed to accomodate slightly different transformer topologies.

The model which is used to characterize the transformers is shown in Figure 3.3. It is made up of four inductances, three capacitances, and four resistances. The inductance of the primary coil is modeled by L_1, its capacitance-to-ground by C_{g1}, and its losses by R_1. The same can be noted for the secondary. Due to the symmetrical geometry of the transformers, the inductance L_1 is always equal to the inductance L_2. Also, the resistance R_1 is always equal to R_2. The mutual inductance of the transformer is represented by M which is divided into two equal parts as can be seen in the model.

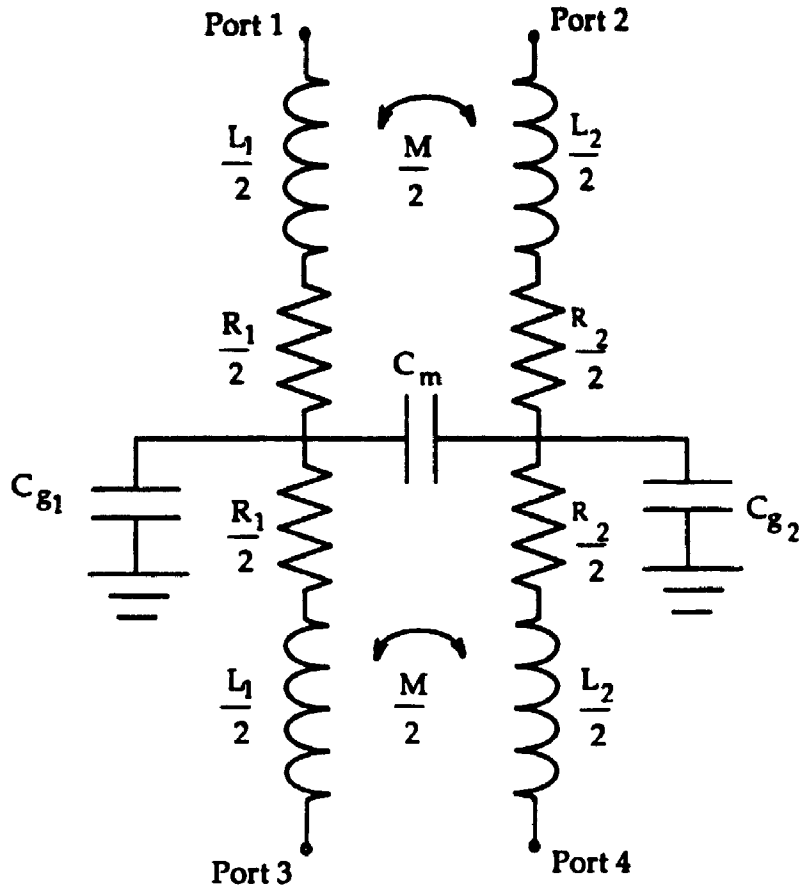

Figure 3.3 Frequency-Dependent Model of a Four-Port Transformer

The inductive coupling between the two coils of the transformer is given by :

$$k = \frac{M}{\sqrt{L_1 L_2}} \tag{3.1}$$

and typically has a value ranging from 0.4 to 0.6 for these types of planar transformers. The mutual capacitive coupling between the primary and secondary is given by C_m.

3.2.1 Model Inductance Analysis

As previously stated, the method used to calculate the transformer inductances is based on the same equations which are used to calculate the

inductances for the inductors. The direction of current through a sample transformer can be seen in Figure 3.5. If it is assumed that at a certain instant in time the current is flowing counterclockwise in the primary coil, then it will flow clockwise in the secondary coil. Hence, the current has a direct analogy to low frequency transformers. All of the transformers studied have the overall primary path length equal to the overall secondary path length, making them 1:1 transformers. Therefore the transformer model will be symmetrical, ie. $L_1=L_2$ and $R_1=R_2$. The structure of the transformers could be modified slightly in order to produce n:1 transformers.

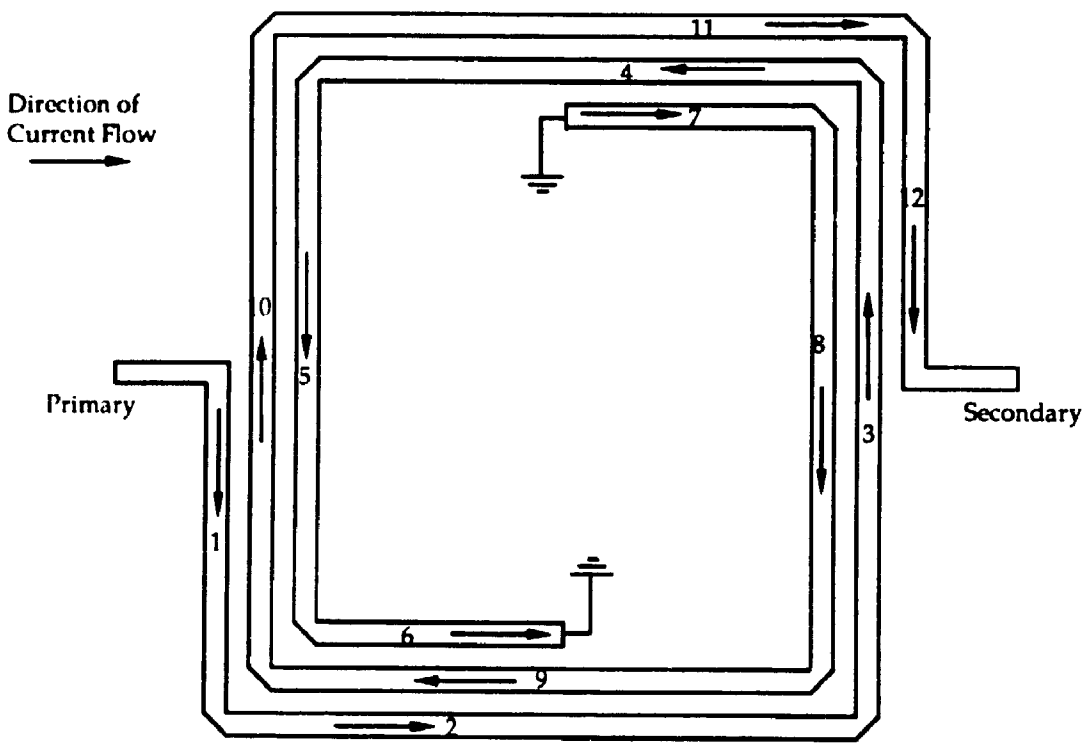

Figure 3.4 Direction of Current Flow Through Sample Transformer

The transformer of Figure 3.4 has six primary and six secondary segments. The self inductances of segments 1 to 6 summed together yield the total self inductance, $L_{1,self}$, of the primary and segments 7 to 12 yield

the total self inductance, $L_{2,self}$, of the secondary.

$$L_{1,self} = \sum_{i=1}^{6} M_{i,i} \tag{3.2}$$

$$L_{2,self} = \sum_{i=7}^{12} M_{i,i} \tag{3.3}$$

$L_{1,self}$ and $L_{2,self}$ are considered to be frequency-independent, for the same reasons as for the square spiral inductor. In addition, the mutual inductances within the primary and secondary spiral must be taken into account. As for the inductor case, $M_{1,5}$ is positive since the direction of current through both segments is the same. On the other hand, $M_{1,3}$ is negative since currents flow in opposite directions. The same rules can be applied for lines 7 to 12. Therefore the net mutual inductances of the primary and secondary is given by :

$$L_{1,mut} = \sum_{i=1}^{6} \sum_{j=1}^{6} M_{i,j} \tag{3.4}$$

$$L_{2,mut} = \sum_{i=7}^{12} \sum_{j=7}^{12} M_{i,j} \tag{3.5}$$

Furthermore, the image inductance of the transformer must be taken into account because of the effect of the ground plane. If the ground plane of the transformer structure is removed for the purpose of inductance analysis, then, in order not to change the properties of the structure, another transformer a distance 2H from the real transformer must be added. This transformer has exactly the same physical dimensions as the previous transformer but the current runs in the opposite direction, so that an electric field is set up with a potential of zero Volts at the ground plane level. Figure 3.5 shows the actual situation which is present in the transformer and Figure 3.6 shows the equivalent image transformer

currents. The relevant equations to determine the primary and secondary image inductance are given by :

$$L_{1,image} = \sum_{i=1}^{6} \sum_{j_{image}=1}^{6} M_{i,j_{image}} \tag{3.6}$$

$$L_{2,image} = \sum_{i=7}^{12} \sum_{j_{image}=7}^{12} M_{i,j_{image}} \tag{3.7}$$

Hence, the total static inductance of the transformer primary and secondary, L_1, and L_2, is given by :

$$L_{1,stat} = L_{1,self} + L_{1,mut} + L_{1,image} \tag{3.8}$$

$$L_{2,stat} = L_{2,self} + L_{2,mut} + L_{2,image} \tag{3.9}$$

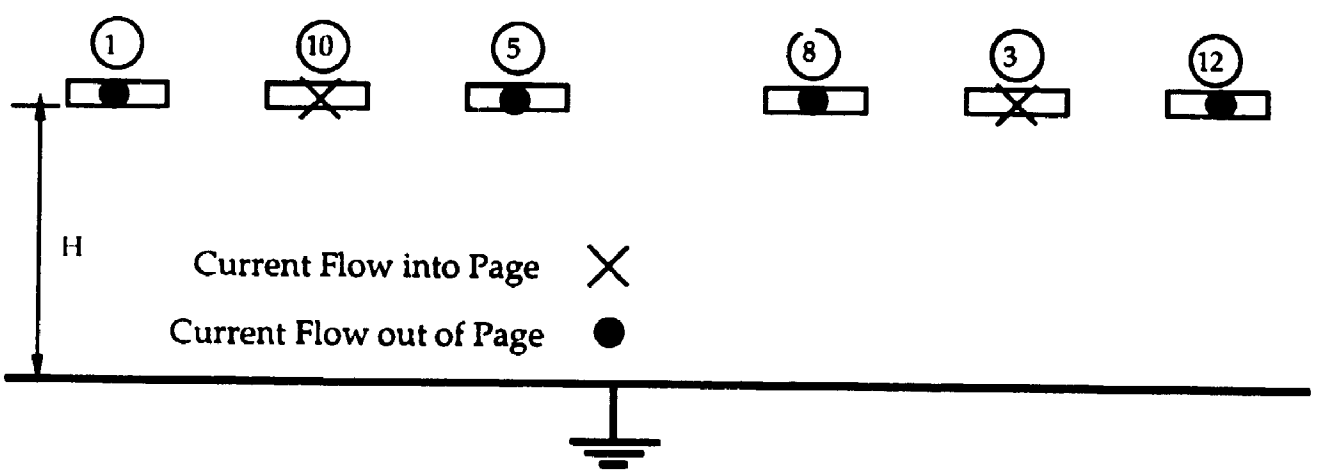

Figure. 3.5 Cross-Section of Current Flow Through the Transformer

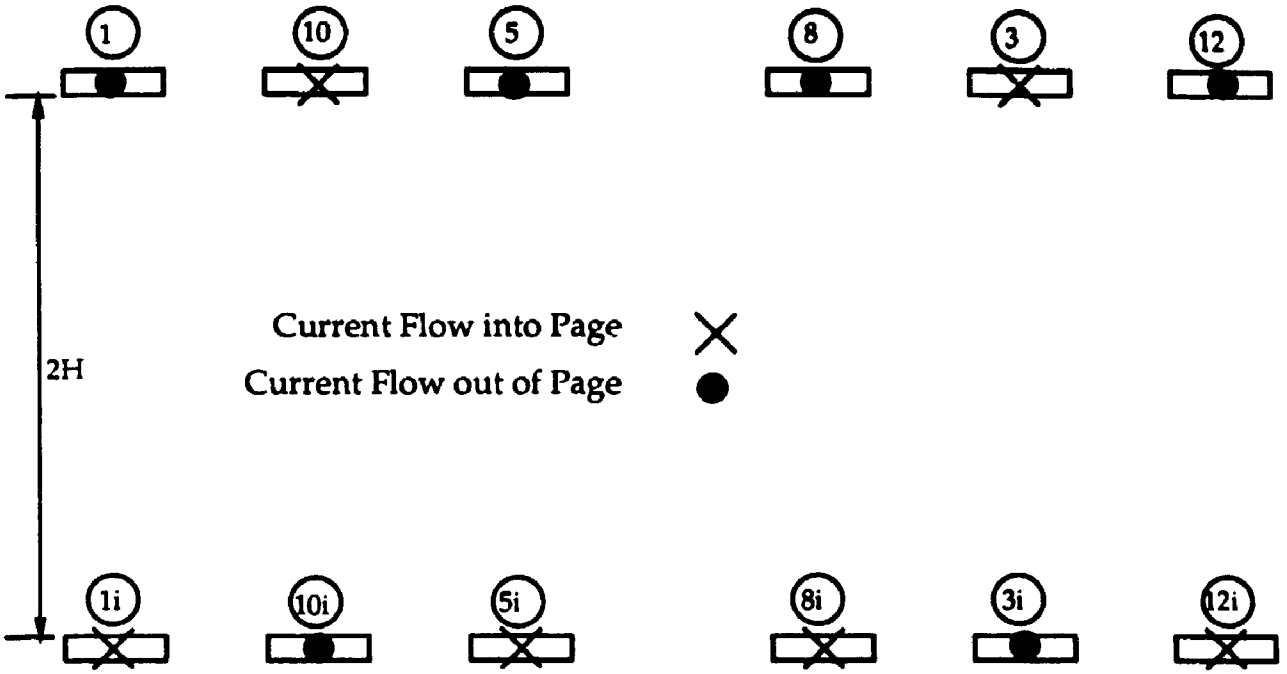

Figure 3.6 Current Flow Through Image Transformer and Actual Transformer

The analysis of ıe total static mutual inductance, M, of the transformer is performed in a similar manner. All of the individual mutual inductances between the primary segments and the secondary segments must be calculated. For example, the mutual inductance between segments 1 and 10 is calculated according to equation 2.1 and the sign of the mutual inductance is determined to be positive. Also, all of the mutual inductances between all pertinent segments of the transformer and its image transformer must be calculated. The appropriate equations are therefore :

$$M_{mut} = \frac{\sum_{i=1}^{6} \sum_{j=7}^{12} M_{i,j}}{2} \tag{3.10}$$

$$M_{image} = \frac{\sum_{i=1}^{6} \sum_{j_{image}=7}^{12} M_{i,j_{image}}}{2} \tag{3.11}$$

Again the double summation in equation 3.10 is divided by two. This is because the mutual inductance between the primary and secondary must not be counted twice, since it is already inherently present in the model as part of the total mutual inductance M. As for the mutual inductance portion of M, the image inductance portion, M_{image} must also be divided by two for the same reason.

Hence, the total static mutual inductance is given as :

$$M_{stat} = M_{mut} + M_{image} \tag{3.12}$$

The frequency dependence of the two inductances is calculated in the same manner as for the spiral inductor. It will be shown that since M in the model is only made up of mutual inductance, and not of any self inductances, its frequency dependent value will change much more rapidly. The self inductance portions of L_1 and L_2 are frequency-independent. Again, the frequency characteristics of the mutual and image inductance portion varies as $\cos(\Delta\theta)$ where $\Delta\theta$ is the phase shift between the centers of the two segments concerned. Therefore the frequency dependent values for $L_{1,mut}$, $L_{1,image}$, $L_{2,mut}$, and $L_{2,image}$ are given by :

$$L_{1,mut}(f) = \sum_{i=1}^{6} \sum_{j=1}^{6} M_{i,j} \cos(\Delta\theta_{i,j}(f)) \tag{3.13}$$

$$L_{2,mut}(f) = \sum_{i=7}^{12} \sum_{i=7}^{12} M_{i,j} \cos(\Delta\theta_{i,j}(f)) \tag{3.14}$$

$$L_{1,image}(f) = \sum_{i=1}^{6} \sum_{j_{image}=1}^{6} M_{i,j} \cos(\Delta\theta_{i,j}(f)) \tag{3.15}$$

$$L_{2,image}(f) = \sum_{i=7}^{12} \sum_{j_{image}=7}^{12} M_{i,j} \cos(\Delta\theta_{i,j}(f)) \tag{3.16}$$

The equations for L_1 and L_2 are then given by :

$$L_1 = L_{1,self} + L_{1,mut}(f) + L_{1,image}(f) \tag{3.17}$$

$$L_2 = L_{2,self} + L_{2,mut}(f) + L_{2,image}(f) \tag{3.18}$$

Similarly, the frequency dependence of the mutual inductance terms M_{mut} and M_{image} must be taken into account. They are given by :

$$M_{mut}(f) = \frac{\sum_{i=1}^{6} \sum_{j=7}^{12} M_{i,j} \cos(\Delta\theta_{i,j}(f))}{2} \tag{3.19}$$

$$M_{image}(f) = \frac{\sum_{i=1}^{6} \sum_{j_{image}=7}^{12} M_{i,j_{image}} \cos(\Delta\theta_{i,j}(f))}{2} \tag{3.20}$$

Hence, the final mutual inductance used in the model is calculated as :

$$M = M_{mut}(f) + M_{image}(f) \tag{3.21}$$

All of the three necessary inductance values in the model are divided by two, which means there are four final self inductances ($L_1/2$, $L_1/2$, $L_2/2$, and $L_1/2$) , and two final mutual inductances ($M/2$ and $M/2$).

3.2.2 Model Capacitance Analysis

The schematic cross-section of the transformer is shown in Figure 3.7.

The capacitance values of the transmission lines are calculated according to the closed-form conformal mapping equations derived by J.I. Smith, in the same way as the square spiral inductors. Again, since these transmission lines are approximately 1 μm thick, there is a small error of several percent introduced by these equations. This amount of error is considered negligible for this type of analysis.

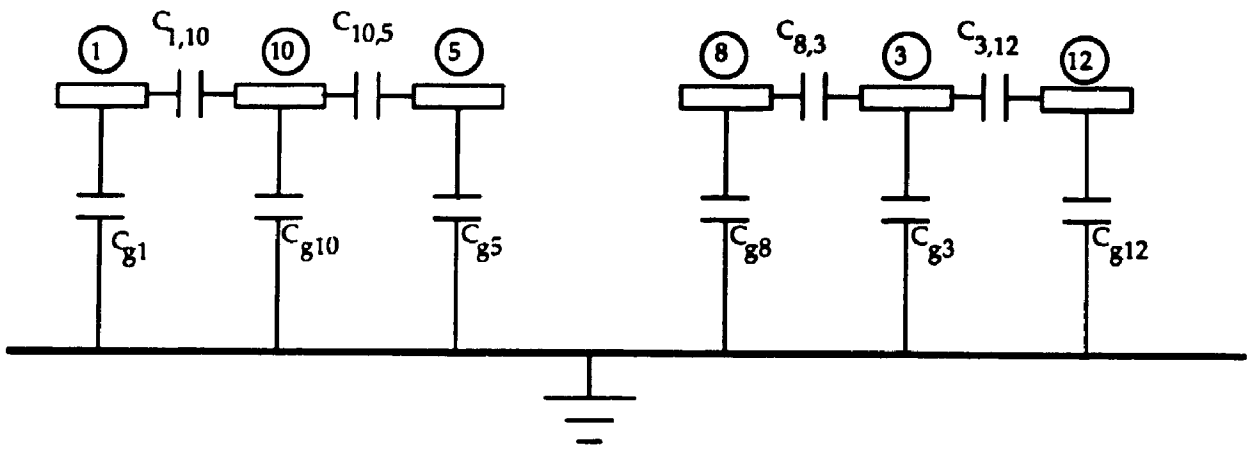

Figure 3.7 Individual Capacitance Values of the Sample Transformer

The value of each capacitance-to-ground depends on its position in the structure. For instance, if C_{g1} is 0.06 fF/μm, then C_{g10} might be 0.02 fF/μm. This is due to the fact that segment 10 has segments on either side of it, whereas segment 1 has only one segment to the right of it. Hence, its capacitance-to-ground is significantly greater. The values C_{g1} and C_{g2} in the model are considered frequency-independent and are given by :

$$C_{g1} = \sum_{i=1}^{6} C_{gi} \tag{3.22}$$

$$C_{g2} = \sum_{i=7}^{12} C_{gi} \tag{3.23}$$

The analysis for the calculation of the interline capacitance values gives the same value for all adjacent lines, regardless of relative position in the structure. Hence, $C_{1,10} = C_{10,5} = C_{8,3} = C_{3,12}$. With the even- and odd-mode analysis used, it is assumed that a value such as $C_{1,5}$ is zero. This is a very reasonable assumption and is quite close to the situation observed in reality. The model variable C_m is given by :

$$C_m = 2\sum_{i=1}^{4} C_{m_i}(1-\cos(\Delta\theta_{i,i+4})) \tag{3.24}$$

The value of $\Delta\theta$ between two adjacent segments is very important in the calculation of the effective capacitive coupling taking place in the transformer. Assuming the propagation of the even mode through the coil has a phase shift of θ_1 from the beginning of the primary and the phase at the center of segment 10 is (180 deg - θ_2). then the difference in phase between the two points is $|(\theta_1 - \theta_2)|$. The 180 degrees does not change the effective value of the phase shift. Equation 3.24 implies that at very low frequencies the value of C_m is quite small, but as frequency increases and the structure begins to have a definite size in terms of wavelengths, the value of C_m increases. Since the structure is inherently symmetrical, it can be seen that only half of the individual capacitances need be calculated, and the subtotal multiplied by 2 to obtain C_m. For small transformers, (sizes below 200 μm x 200 μm), the value of C_m is usually quite small and does not increase too rapidly with frequency.

It has been found that C_m is most critical to the proper calculation of the model response at high frequencies. Since dispersion effects inevitably take place at frequencies higher than 12 GHz, for the line widths used, the accuracy of the model may be slightly affected at these higher values in some cases.

3.2.3 Model Resistance Analysis

The analysis of the R_1 and R_2 elements of the model is very similar to that used for the rectangular inductors. The sum of R_1 and R_2 represents the total losses present in the transformer primary including the ohmic and dielectric losses. As before, it is found that since the spacing between the lines is not any closer than 5 μm, an even and odd mode analysis is not required to be done for these structures. The pertinent equations used for the resistance analysis are therefore equations 2.20 to 2.26 of chapter 2.

3.2.4 Other Effects Included

As for the inductors, the corner discontinuities are included in the design in order to have a more accurate model. The effects of the corner bends on the model at low frequencies are quite small due to their being chamfered. However, at higher frequencies they have a more significant effect. Therefore the equations that were used to calculate corner discontinuity values are given by 2.27 and 2.28 of chapter 2.

Dispersion occurs in any microstrip line above a certain frequency. When a microstrip line becomes dispersive it not only supports the quasi-TEM mode, but a host of other non-TEM modes, Reducing the guided wavelength in the microstrip, λg. For the dimensions of transmission lines typically used in the transformers, dispersion of the even mode can be ignored up to 12 GHz.

When necessary, dispersion can be taken into account by using the actual even-mode wavelength in the microstrip, $\varepsilon_{r,eff}$ (f), to calculate the phase shifts of the current around the coils.

3.3 Computer Program Integration

The transformer analysis was integrated into programs to calculate the S-parameters for two different kinds of transformers. The transformer of figure 3.2 is the standard non-center-tapped transformer fabricated at CRC, and its user-defined model will be discussed first.

3.3.1 Non-Center-Tapped Transformers

The analysis described in section 3.2 was distilled into a computer program which calculates the device parameters and then passes them to SuperCompact via a user-defined model. This model is called SSTR and has the following format:

```
  SSTR 1 2 3 4  TUR=2.25 LN1=250 LN2=250 WID=10 SPA=10 HEI=254
+ THI=1 RHO=1 EPS=9.9
```

The variables required to be specified are :

- TUR - the number of rotations of the transformer primary and secondary
- LN1 - overall horizontal dimension of the transformer
- LN2 - overall vertical dimension of the transformer
- WID - track width
- SPA - track spacing
- HEI - microstrip substrate height
- THI - first layer metal thickness (do not use 0)
- RHO - resistivity of the metal relative to gold being 1.0
- EPS - dielectric permittivity of the substrate

Note, all of the dimensions used in the model are assumed to be in units of μm.

Figure 3.8 is a sample transformer with all pertinent dimensions shown. The number of rotations of the primary and secondary is 2.25. Allowable numbers which can be used for TUR are 1.25, 1.75, 2.25, 2.75, 3.25, 3.75, 4.25, 4.75 etc. Also, the model parameters LN1 and LN2 which are used must be at least large enough to accomodate the number of turns specified by the user, otherwise an error will occur when the dimensions of each of the transformer segments are calculated.

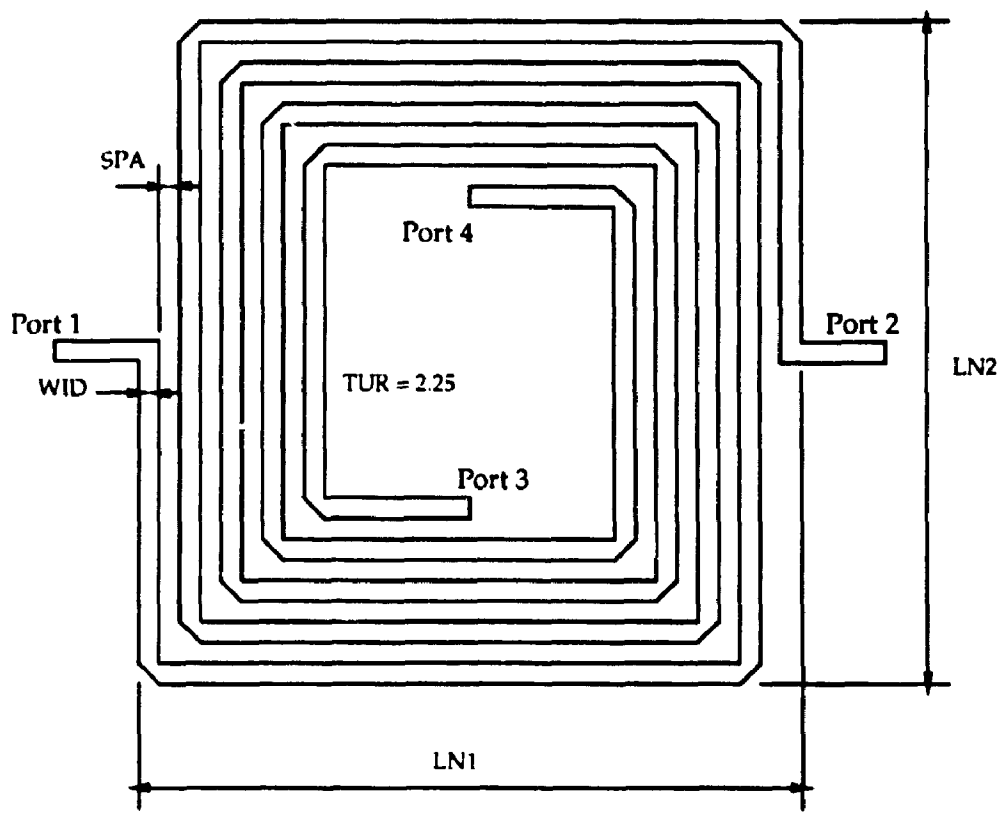

Figure 3.8 Sample Transformer With Required Dimensions for Input into User-Defined Model

The value of RHO used for pure gold is 1.0. However, since each

process produces a different resistivity of gold the proper value must be chosen. Typical values range from 1.5 to 3 depending on the quality of the gold and the method of circuit fabrication.

The method used to calculate the Y-parameters from the model element values of the device is explained in Appendix II.

3.3.2 Center-Tapped Transformers

Center-tapped transformers have slightly different applications than the non-center-tapped variety. A possible use for this type of transformer is at the input and output of a pushpull amplifier. Here, the transformer can convert the input signal to two signals which are 180 degrees out of phase in order to drive two active sections in class B operation. When one side of the amplifier is completely turned off, the other side is full on. The signal at the output is again formed by combining the output signals of the two sides of the amplifier into one signal. This type of amplifier is potentially useful for operation in medium power circuits. However the advantage gained by using a pushpull amplifier in a small signal application would not warrant the extra complexity of the circuit. This topic will be discussed more thoroughly in Chapter 5.

A photograph of such a transformer can be viewed in Figure 3.9. It has a topology which is identical to that of the non-center-tapped transformers except that it contains a transmission line to ground at the center of the secondary. The device is basically intended to be used as a three-port. The input port 1 on the left leads into the primary, with the other end of the primary grounded. The secondary has two outputs at either side. Hence, the signals at ports 2 and 3 should be approximately 180° out of phase and therefore balanced.

Figure 3.9 Photograph of a 1-3/4 Turn Center-Tapped Transformer

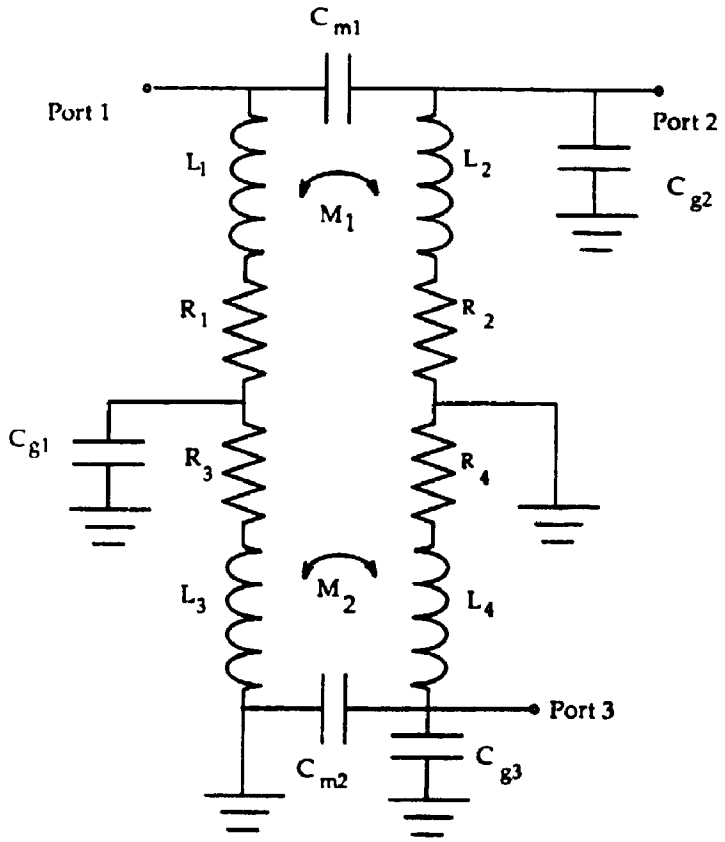

Figure 3.10 Center-Tapped Transformer Model

The model which was developed for this type of transformer is shown in Figure 3.10. It is very similar to the model for non-center-tapped transformers This is because the fundamental structure of the latter is almost identical to the former, except for the grounding of the secondary center. Its Y-parameter derivation is explained in Appendix III.

The model of Figure 3.10 was used to calculate the parameters of the center-tapped transformer. It can be seen that one end of the transformer is grounded. The output is taken at either end of the transformer secondary. Since the secondary is grounded at a certain point, the capacitance, C_{g2}, which existed for the previous case, is now moved to port 2. Also, there is now an additional capacitance, C_{g3}, which is used to represent the capacitance-to-ground on the other half of the secondary. The capacitor C_m does not exist any more. Instead, it is divided between the two capacitors C_{m1} and C_{m2}. Since the transformers are laid out such that the total transmission line length from port 2 to the center tap is greater than the length from the center tap to port 3, the inductances L_1 and L_2 are larger than L_3 and L_4. At the same time M_1 must be greater than M_2 for the same reason. Also, the resistors R_1 and R_2 must have greater values than R_3 and R_4.

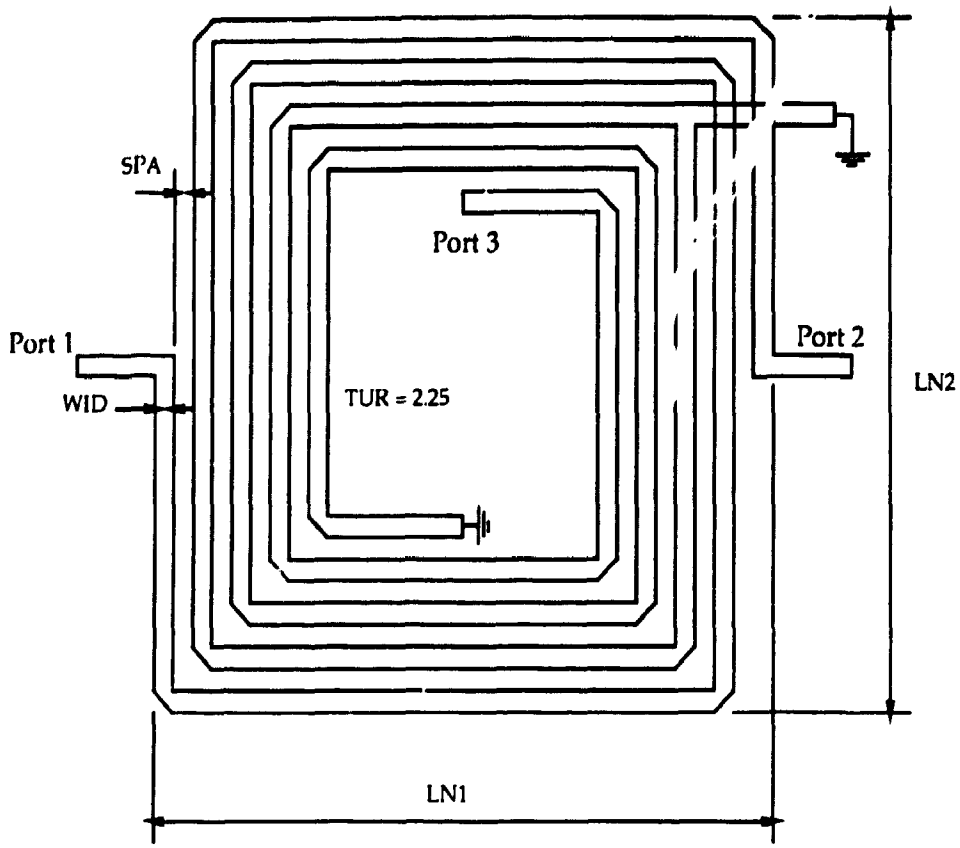

Figure 3.11 Sample Center-Tapped Transformer with Required Dimensions

The analysis for the center-tapped transformers was performed in a manner similar to that outlined above. Since the analysis is very similar, the FORTRAN 77 computer program did not have to be changed significantly. A sample transformer is shown in Figure 3.11 along with the required dimensions as input to the element SSCN. The user defined center-tapped model is :

```
SSCN 1 2 3 4  TUR=2.25 LN1=250 LN2=250 WID=10 SPA=10 HEI=254
+  THI=1 RHO=1 EPS=9.9
```

The variables required to be specified are :

TUR - the number of rotations of the transformer primary and secondary

LN1 - overall horizontal dimension of the transformer

LN2 - overall vertical dimension of the transformer

WID - track width

SPA - track spacing

HEI - microstrip substrate height

THI - first layer metal thickness (do not use 0)

RHO - resistivity of the metal relative to gold being 1.0

EPS - dielectric permittivity of the substrate

It can be seen that the same parameters are input for the center-tapped transformer as for the non-center-tapped transformer. The computer program assumes the location of the center tap. If the center tap is in a different position to that originally assumed, then the program can easily be modified to take the change in position into account. The model will give the three-port S parameters for the transformer.

3.4 Results and Discussion

3.4.1 Non-Center-Tapped Transformers

The transformers were fabricated on both alumina and quartz substrates. Results are given in this section for both types of transformers on the different substrates.

The S_{11} and S_{21} parameters for a 385 μm x 385 μm transformer, with 20 μm track width and 10 μm track spacing, and 2-1/4 turns on 0.010" alumina can be seen in Figure 3.12. The element values for its model can be viewed in Table 3.1.

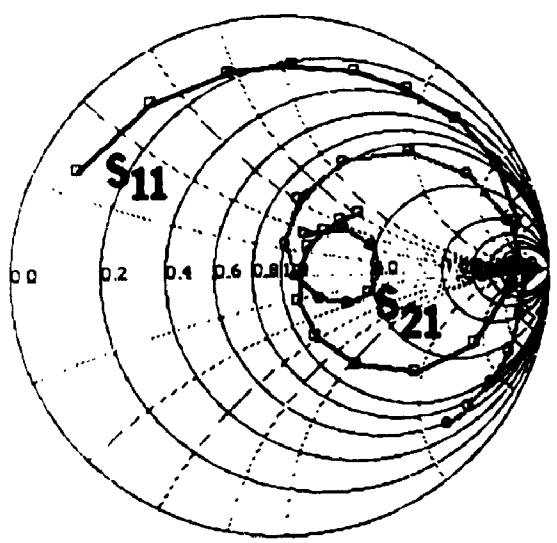

Figure 3.12 Measured S Parameters of 2-1/4 Turn Transformer on 0.010" Alumina

The S_{11} curve has a magnitude of approximately 0.9 for frequencies from 1 to 10 GHz. For this same range of frequencies $|S_{21}|$ shows a very small value from a maximum of 0.4 at 3 GHz to a minimum of 0.1 at 8 GHz. Since the transformer structure is symmetrical, $S_{11} = S_{22}$ and $S_{21}=S_{12}$. This in fact was observed when the devices were measured. The small

differences are within the accuracy of the network analyzer and the calibration method used. From the small magnitude of the measured S_{21} parameter over the lower frequency range, it can be seen that the coupling which one obtains from the transformer is not particularly significant. If the primary and secondary were more tightly coupled then the peak value $|S_{21}|$ should be larger.

The range from 1 to 8 GHz is the more useful range of transformer operation. This is evident when observing Figure 3.13c which shows the results as linear magnitude vs. frequency. The Figure clearly shows that for frequencies greater than 8 GHz the value of $|S_{21}|$ increases to a value of 0.9. It might be thought that this is desirable, however this is not the case. For frequencies above 8 GHz the capacitive effects in the structure become very significant and can no longer be ignored.

The modeled results for the structure can also be seen on the same figure. The agreement is quite good in the range 0 to 10 GHz. However, it can be seen that the measured resonance of S_{11} at approximately 15 GHz, is predicted to occur at 11 GHz by the model. This discrepancy is believed to be caused partially by ignoring the capacitive effect of the airbridge on the structure and only considering it as a certain length of transmission line leading out of the transformers. The same problem can be seen in Wiemer's[25] results (Figure 3.14) where the S_{21} minimum frequency is easily predicted, but where the S_{11} resonance is predicted 2 GHz lower than it actually occurs. Another reason for this problem may be the coupling effect between corners in the structure which has not been very well understood to date.

The error in phase is negligible over the frequency range of interest. Some phase error in S_{11} can be seen in Figure 3.13b above 11 GHz. This phase error occurs because the resonance frequency is predicted to be lower than the measured value. Also an increasing phase error above 8 GHz can be seen in Figure 3.13d for S_{21}. Again, this is believed to occur from the air bridge model used which becomes increasingly less accurate for

frequencies above X band.

Table 3.1
Model Element Values for Transformer
of Figure 3.13

f (GHz)	L_1 (nH)	M (nH)	R_1 (Ω)	C_{g1} (fF)	C_m (fF)
1	2.15	1.05	5.41	69.3	1.5
2	2.15	1.04	5.64	69.3	6.0
3	2.15	1.03	5.93	69.3	13.5
4	2.15	1.01	6.30	69.3	23.8
5	2.15	1.00	6.72	69.3	36.8
6	2.14	0.97	7.19	69.3	52.3
7	2.14	0.95	7.26	69.3	70.1
8	2.14	0.92	7.31	69.3	89.1
9	2.13	0.88	7.38	69.3	111
10	2.13	0.85	7.46	69.3	134
11	2.12	0.81	7.54	69.3	155
12	2.11	0.77	7.63	69.3	183
13	2.10	0.73	7.72	69.3	208
14	2.10	0.69	7.82	69.3	233
15	2.09	0.65	7.91	69.3	258
16	2.08	0.61	8.00	69.3	282
17	2.07	0.57	8.10	69.3	305
18	2.06	0.53	8.19	69.3	327
19	2.05	0.50	8.29	69.3	347
20	2.04	0.46	8.38	69.3	364

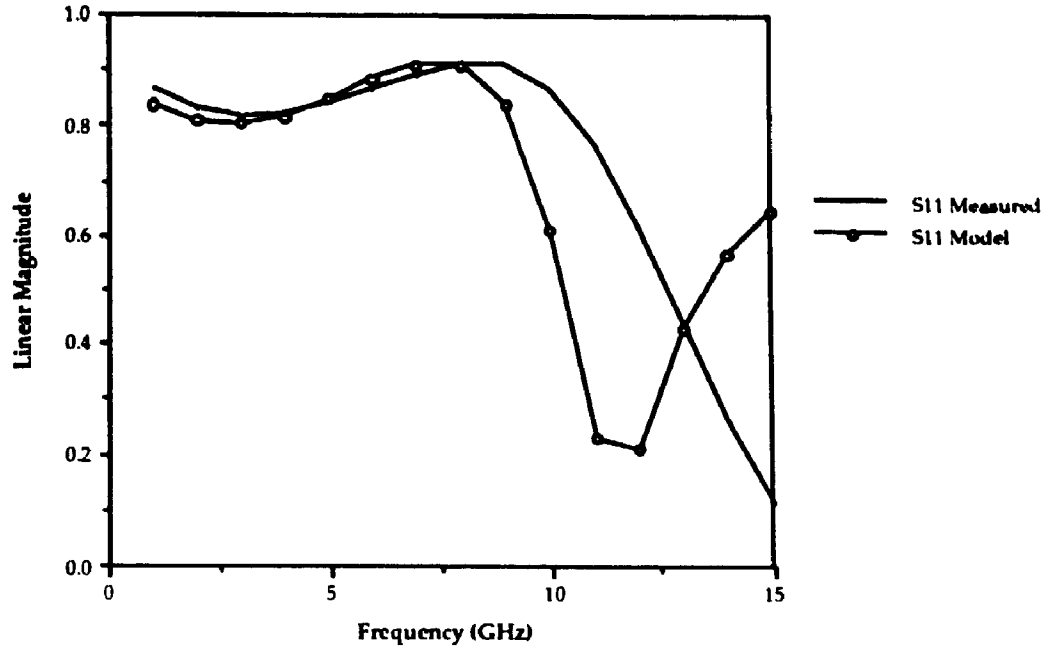

Figure 3.13a |S11| Response of 385 μm Square Alumina Transformer

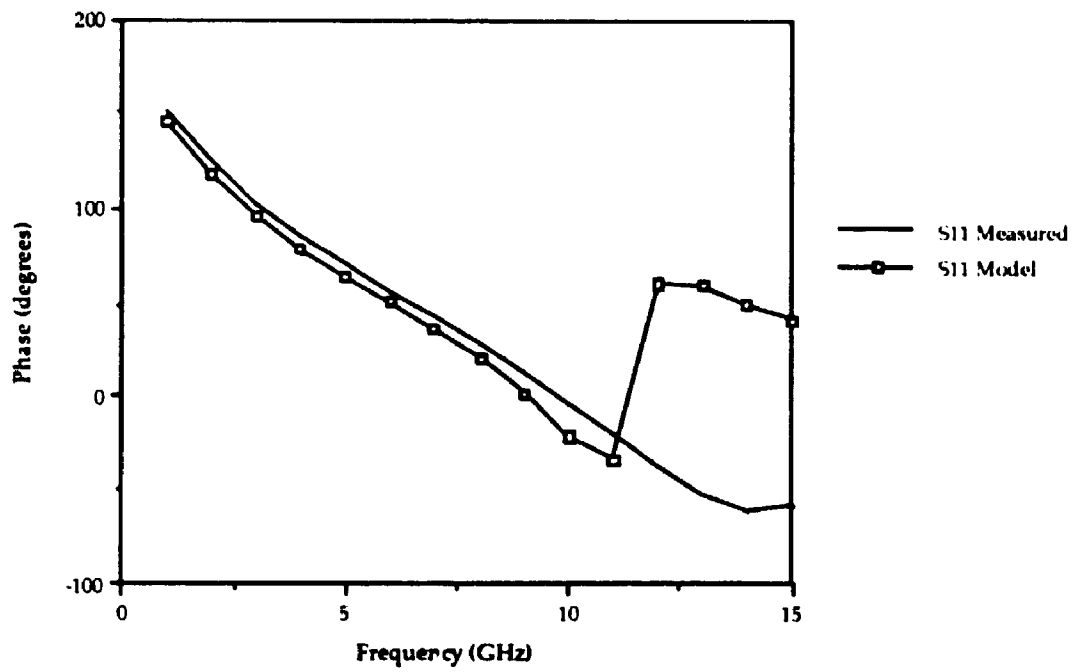

Figure 3.13b S11 Phase Response of 385 μm Square Alumina Transformer

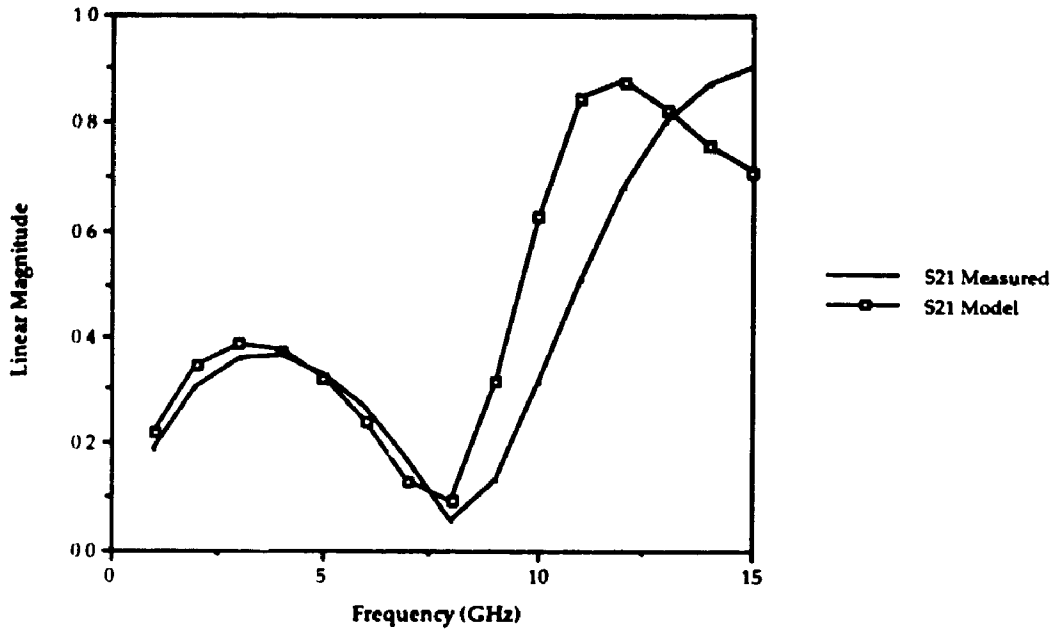

Figure 3.13c |S21| Response of 385 μm Square Alumina Transformer

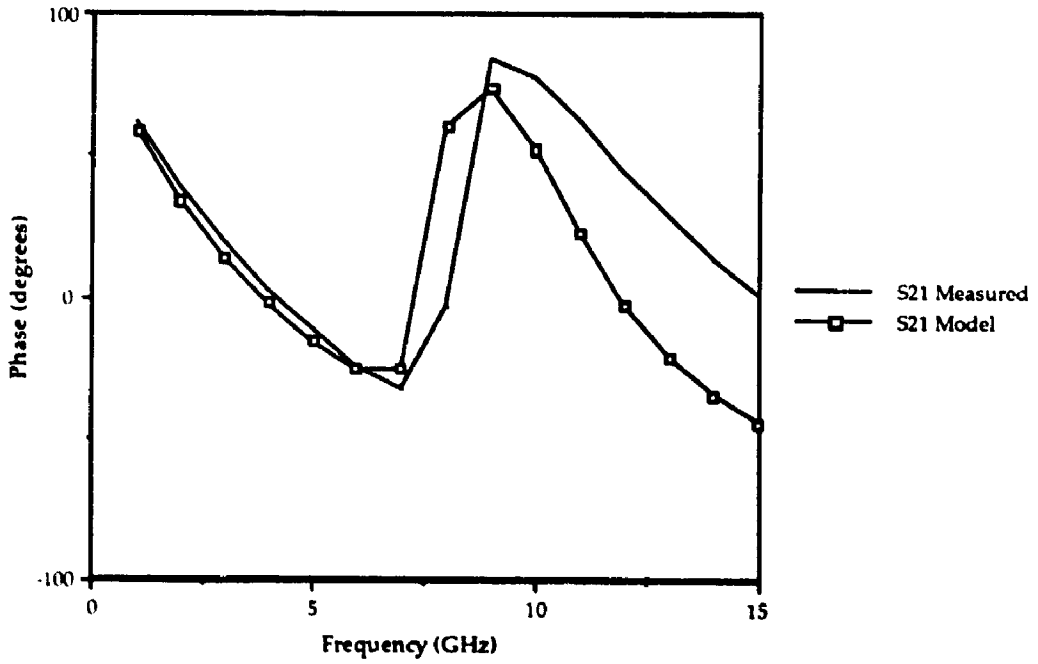

Figure 3.13d S21 Phase Response of 385 μm Square Alumina Transformer

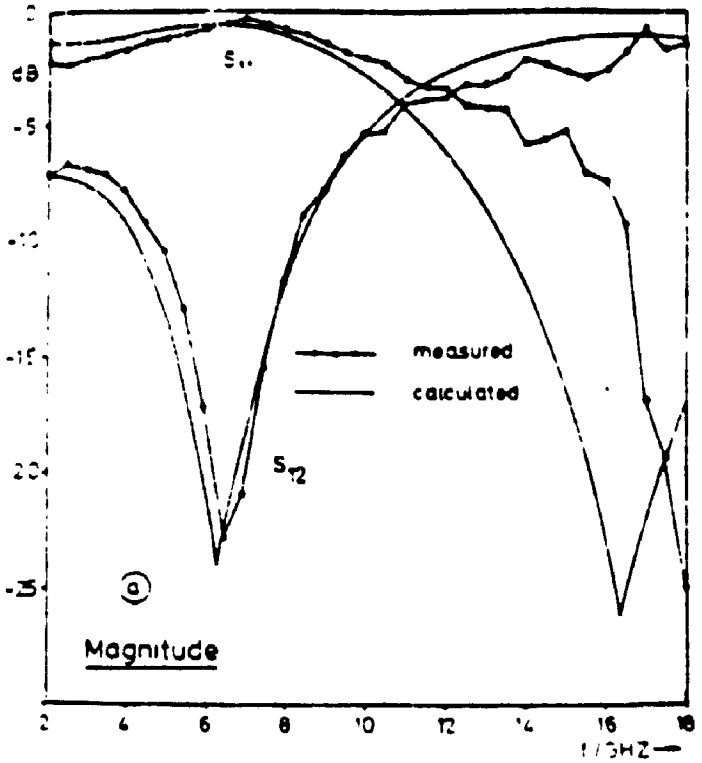

Figure 3.14 Results of Wiemer[25] for Typical MMIC Transformer

The measured and modeled results for another transformer on alumina are shown in Figure 3.15. It has dimensions of 265 μm x 245 μm with a track width and spacing of 10 μm and 2-1/4 turns. The modeled magnitude and phase results are seen to agree quite well with the measurements. Again, though, the same response is seen where the transformer has a very high return loss and a large insertion loss which makes it more difficult to use in certain circuits where power loss through the structure must be minimized.

Unlike the previous transformer, this one has no observable resonance in the frequency range from 1 to 20 GHz. Since this transformer has a considerably smaller primary and secondary overall path length, it remains inductively coupled over a much larger frequency range. Also, the maximum inductive coupling of approximately -7dB for this transformer occurs at a slightly higher frequency of 8 GHz.

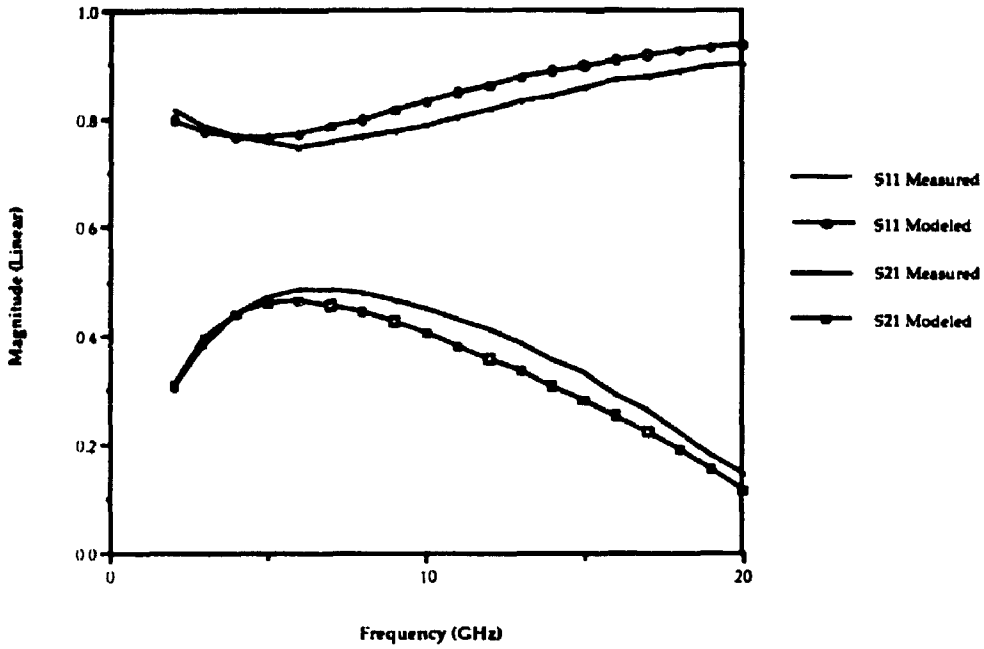

Figure 3.15a Magnitude Response of a Small Transformer on Alumina

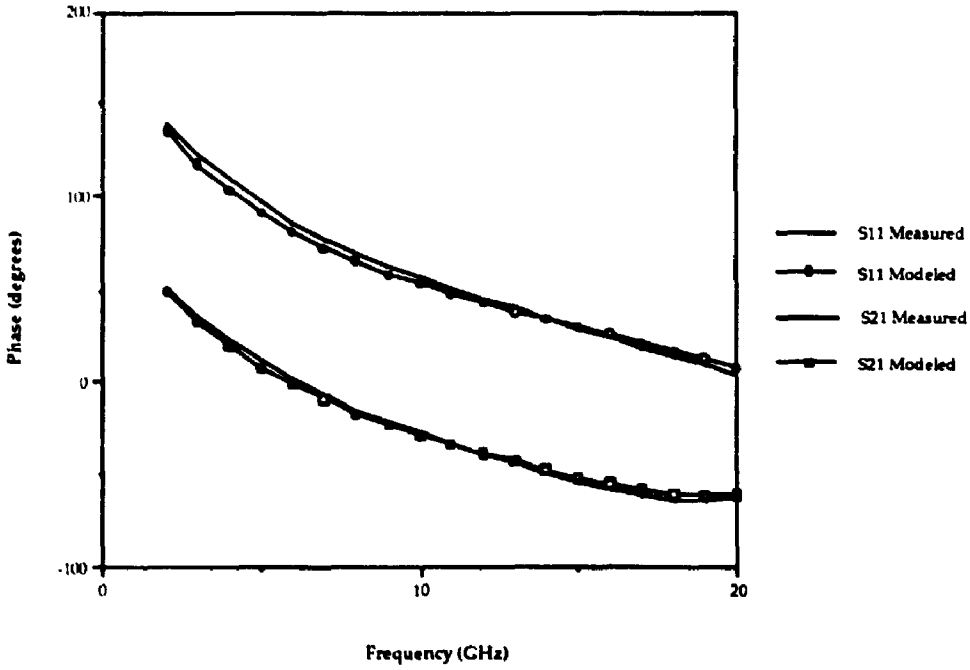

Figure 3.15b Phase Response of a Small Transformer on Alumina

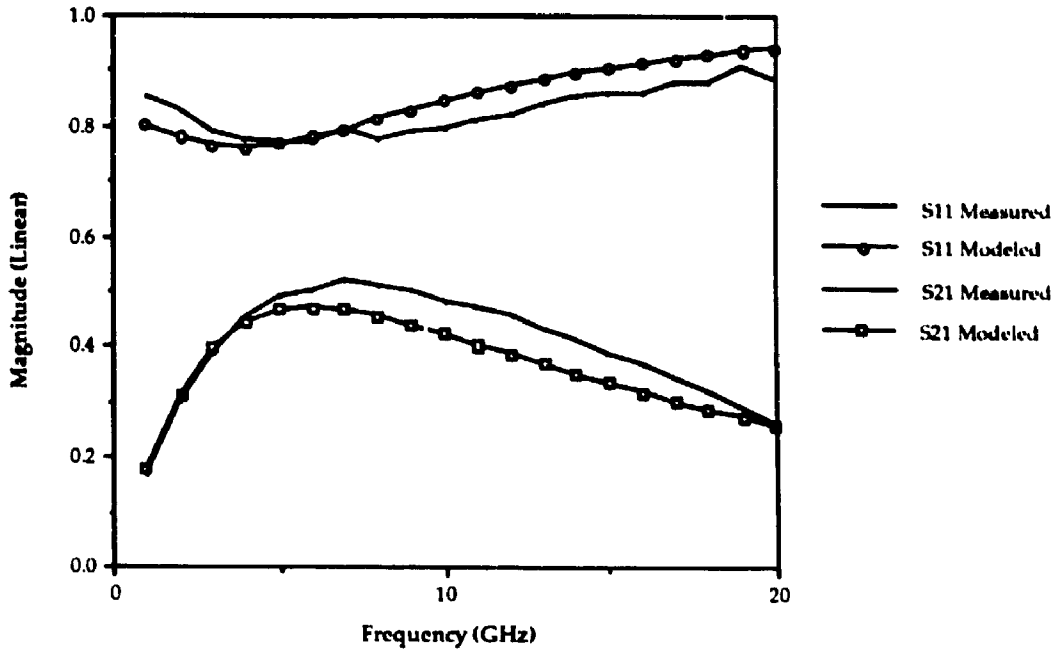

Figure 3.16a Magnitude Response of a Small Transformer on Quartz

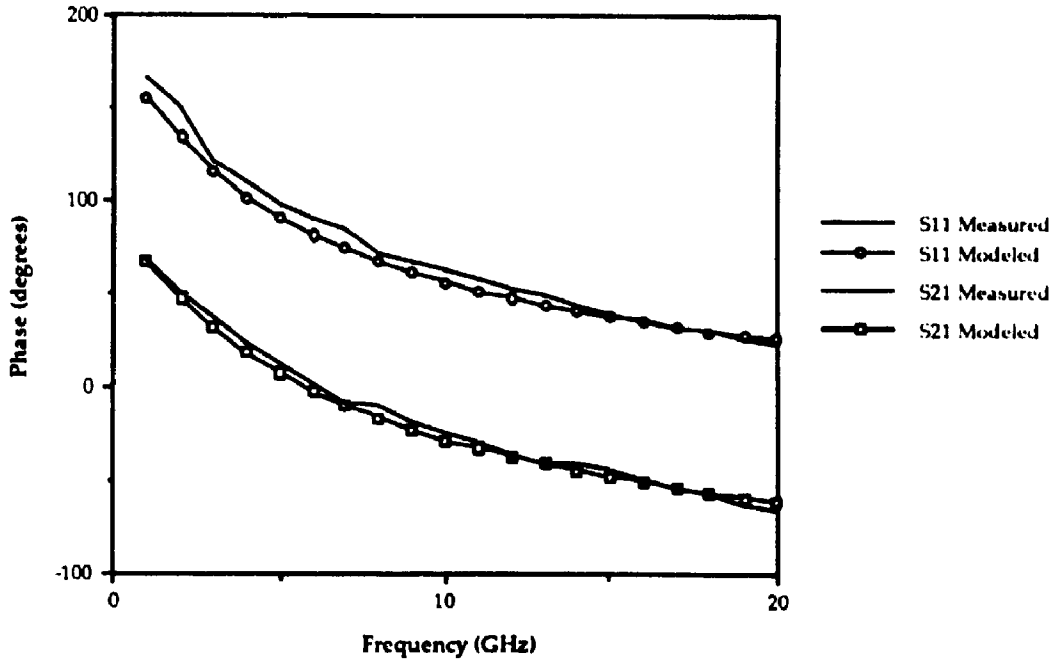

Figure 3.16b Phase Response of a Small Transformer on Quartz

Figures 3.16a and 3.16b show the results for an identical 265 μm x 245 μm transformer, fabricated on a quartz substrate. The maximum inductive coupling is seen to be slightly larger than for the alumina transformer. The transformer bandwidth is also seen to be slightly larger, as was predicted by the SSTR model. It can be said that transformers fabricated on substrates with a smaller permittivity, in general, will have better characteristics than those fabricated on high permittivity substrates. This is especially true for transformers operating in the higher frequency range, where the larger bandwidth may be critically important.

The theoretical frequency response for a 400 μm x 400 μm, 2-1/4 turn transformer with track widths of 20 μm and track spacings of 10 μm can be seen in Figure 3.17.

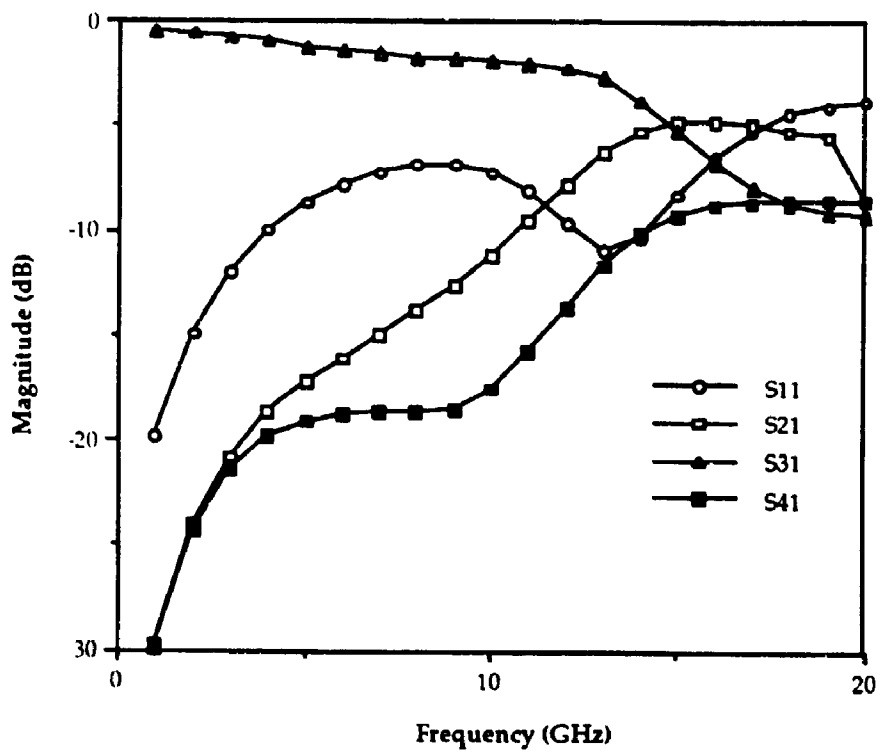

Figure 3.17 Frequency Response of 400 μm x 400 μm Four-Port Transformer with 2-1/4 Turns on 0.010" Alumina Substrate

The ports here are labelled the same way as in the SSTR model of the transformer. The results are seen to be very similar to those for a very weakly coupled pair of transmission lines. If port 1 is considered as the input, then port 3 is the direct port, port 2 is the coupled port, and port 4 is the isolated port. In this particular case the results show that at approximately 14 GHz, the direct and coupled power of the transformer is approximately -5 dB, and the isolation is 10 dB. The frequency at which the unwound length of the spiral is equal to $\lambda_{effective}/4$ gives approximately the point of maximum coupled power at port 2 of the transformer. The better than 20 dB isolation for frequencies below 10 GHz is acceptable, but it can be seen that for larger frequencies the isolation degrades significantly due to the rapidly changing values of the lumped element components in the higher frequency bands.

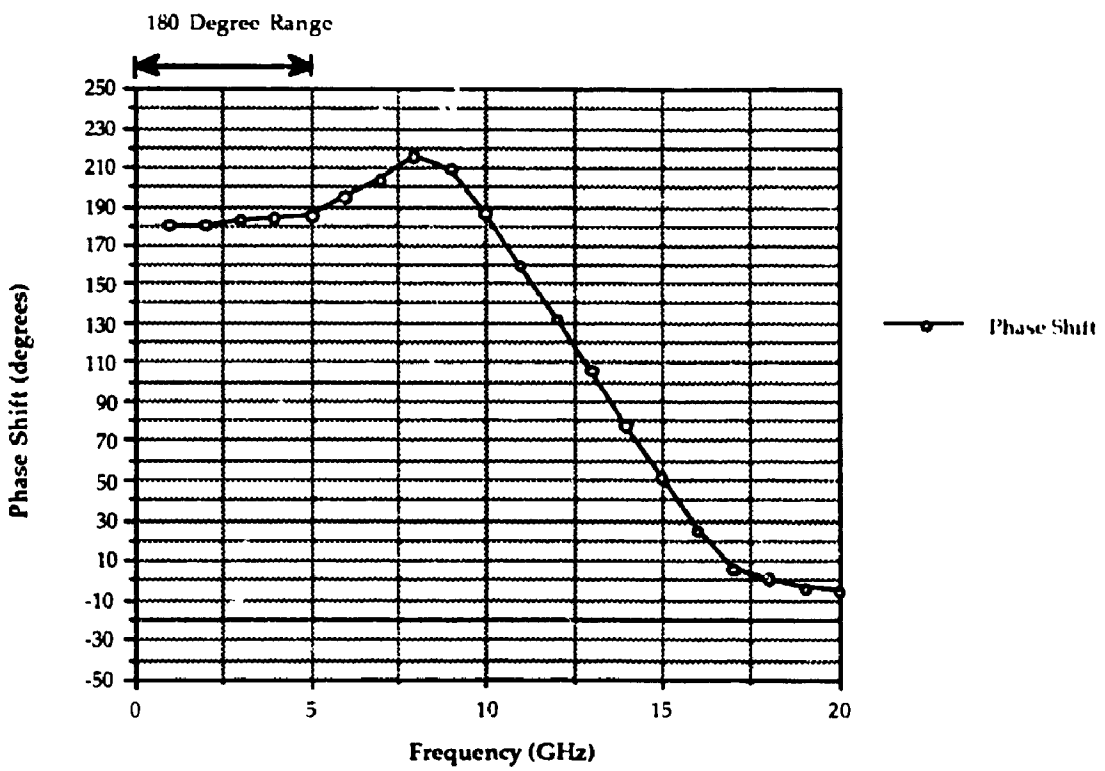

Figure 3.18 Differential Phase Shift Between Ports 2 and 4 for a Sample Transformer

2 OF/DE 2

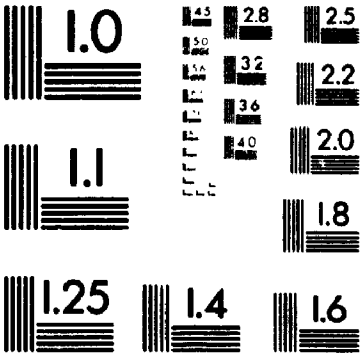

MicroD

A very useful application of a transformer is as a 180 degree phase shifter. Observing the four-port S parameters for the above transformers, the phase difference between the signals appearing at ports 2 and 4 is approximately 180 degrees. Once the transformer is not operating any more in the region where the majority of the power transferred to the secondary is inductively coupled, then the phase shift between ports 2 and 4 begins to decrease. The phase difference results for the transformer mentioned above can be seen in Figure 3.18. The region where the phase shift is within several degrees of the ideal 180 degrees is from DC to 5 GHz. From 5 GHz to 10 GHz the phase shift increases to a maximum value of 215 degrees and then decreases back to 180 degrees. For frequencies greater than 10 GHz, the phase shift begins to approach 0 degrees.

In order to learn more about the effects of changing a transformer's track widths and spacings, but keeping its area the same, the SSTR model was run for several different cases for a 385 μm x 385 μm. 2-1/4 turn transformer, on 0.010" alumina. The results of these analyses can be seen in Figures 3.19, 3.20, and 3.21. They are given in the form of the S21 magnitude as a function of frequency. The test cases are run for line widths from 10 to 20 μm in steps of 5 μm. For each of these line widths the spacing is varied from 5 μm to 20 μm in steps of 5 μm.

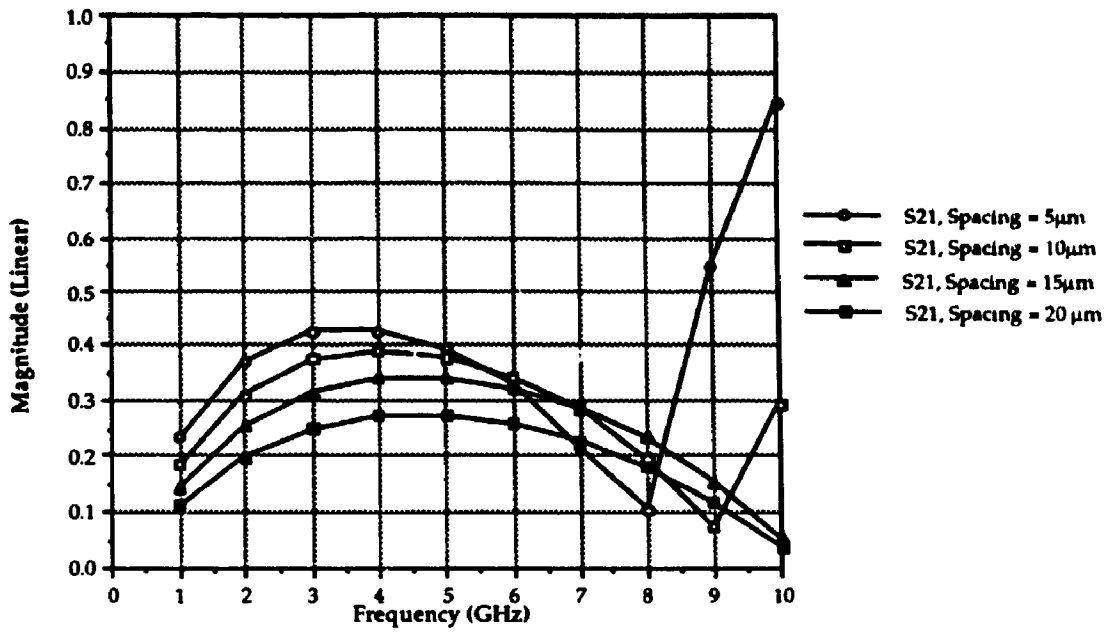

Figure 3.21 Sample Model Results for Transformer with WID = 20 μm

The results show several interesting patterns. For each transformer it is seen that as the track spacing is decreased, with all other variables held constant, the coupling between the input and output spirals increases. This is evident because as the lines are spaced closer together, the effective mutual coupling between any two lines on the same side of the transformer is greater. Furthermore, it can be seen that for smaller spacings the bandwidth of the transformer is decreased. Hence, for wideband operation the transformer should be operated with larger spacings, even though the insertion loss may be up to 3 dB greater, depending on the device. In order to maximize bandwidth, the track widths and spacings should be kept larger. If less insertion loss is desired, then the lines should be made narrower and the spacings smaller.

It can be seen that for this transformer, with the given technology, it would be difficult to achieve $|S_{21}|$ greater than 0.5 (or an insertion loss of

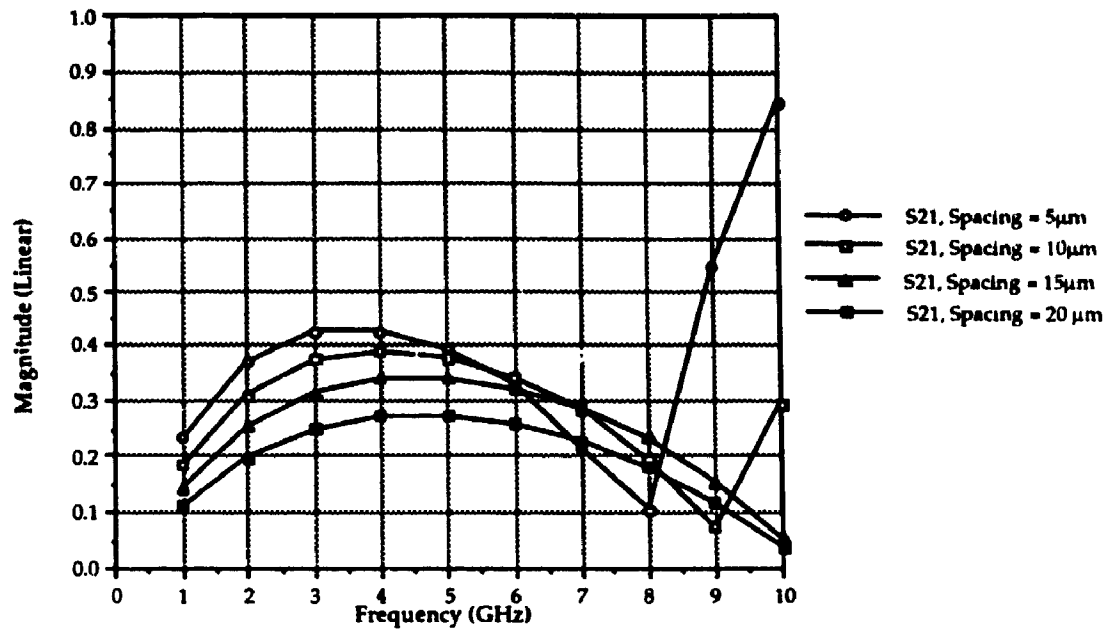

Figure 3.21 Sample Model Results for Transformer with WID = 20 μm

The results show several interesting patterns. For each transformer it is seen that as the track spacing is decreased, with all other variables held constant, the coupling between the input and output spirals increases. This is evident because as the lines are spaced closer together, the effective mutual coupling between any two lines on the same side of the transformer is greater. Furthermore, it can be seen that for smaller spacings the bandwidth of the transformer is decreased. Hence, for wideband operation the transformer should be operated with larger spacings, even though the insertion loss may be up to 3 dB greater, depending on the device. In order to maximize bandwidth, the track widths and spacings should be kept larger. If less insertion loss is desired, then the lines should be made narrower and the spacings smaller.

It can be seen that for this transformer, with the given technology, it would be difficult to achieve $|S_{21}|$ greater than 0.5 (or an insertion loss of

6 dB). This is one of the fundamental problems of these planar transformers. If the transformer were to be fabricated with the second layer gold placed directly on top of the first layer of 1 μm gold, then the total thickness of gold would be 5 μm. The Q-factor of the transformer would increase significantly and the device would become more efficient.

Also, track width and track spacing can significantly affect the performance a transformer in terms of its peak coupling frequency and bandwidth[26].

3.4.2 Center-Tapped Transformers

The photograph of the 455 μm x 455 μm center-tapped transformer, with 20 μm track width and 10 μm track spacing, on 0.020" quartz shown in Figure 3.9 is modeled in Figure 3.23. The model is very accurate below the first resonant frequency at 18 GHz. Above resonance, the dominant coupling mechanism becomes capacitive and here the structure shows a maximum power transfer with 1.9 dB insertion loss. The modeled $|S_{21}|$ magnitude is seen to overpredict the amount of coupling to the secondary port. This is most likely due to the fact that the value used for RHO was 2.0 and the actual value may have been slightly higher due to the quality of the gold used in the first layer metal.

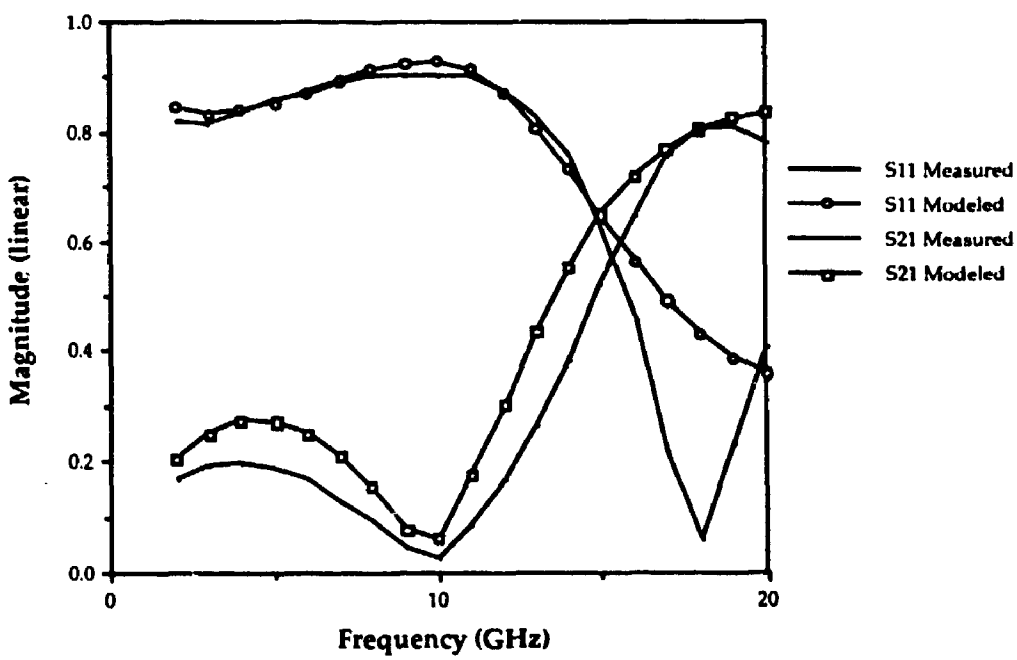

Figure 3.23a Magnitude Response of Center-Tapped Transfomer on Quartz

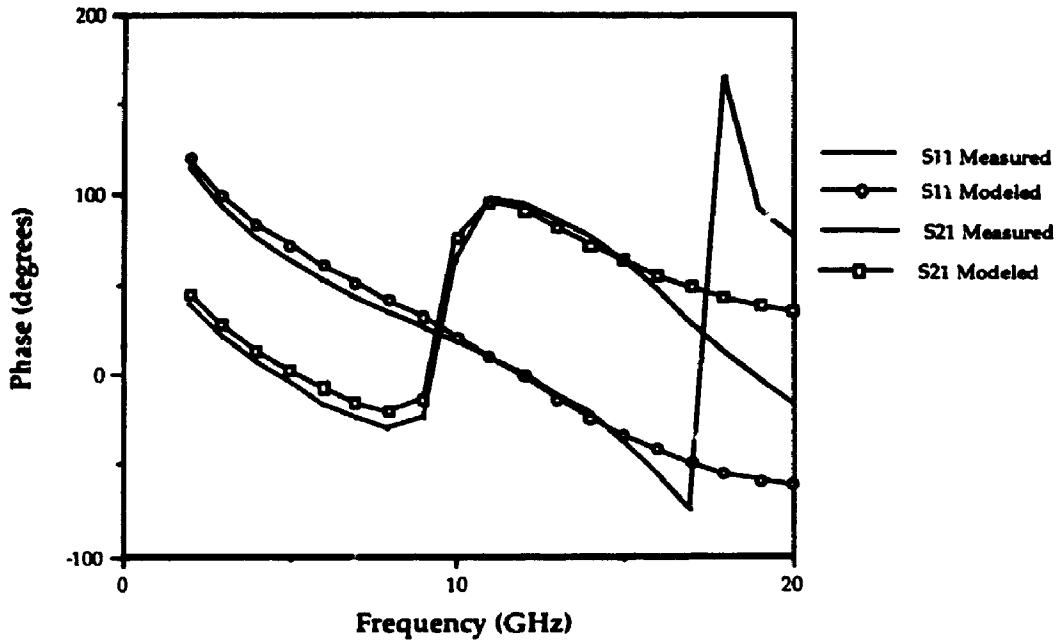

Figure 3.23b Phase Response of Center-Tapped Transfomer on Quartz

Also, the results can be seen to begin to deviate from the measured results as the frequency increases to values greater than 15 GHz. At these frequencies the limitations of the model are beginning to be brought out. The calculations for effective mutual coupling capacitance, and effective mutual inductance between the primary and secondary are becoming inaccurate at the higher frequencies.

Hence, the center-tapped transformers behave very similarly to the non-center-tapped transformers, but are only used in very specific applications such as pushpull amplifiers which are discussed in more detail in chapter 5. It can be noticed that the magnitude of S_{21} at the frequency of peak inductive coupling is no greater than 0.2. Therefore, if the transformer were to be used in an amplifier it would have to be matched in order to provide low insertion loss. This is one of the present

drawbacks of MHMIC planar transformers.

4 Overlay Couplers

4.1 Introduction

Overlay couplers were investigated as a possible alternative to standard edge-coupled couplers. A typical application could be to couple some power out to one circuit for sensing. while letting most of the power flow through to another circuit. The problem encountered with typical edge-coupled structures is that the dimensions required for the overall structure can be too excessive for a certain circuit application which is limited by space. Since the two lines of an overlay coupler are broadside to each other, and the gap between them is very narrow (here 0.2 μm), much more coupling can be obtained between the two lines without the need for large widths of lines placed beside each other on a substrate. The typical structure of an overlay coupler is shown in Figure 4.1. It basically consists of a long thin-film capacitor fabricated on some substrate material with a ground plane on its underside. The top plate in the process has a thickness of 4 μm while the bottom plate's thickness is only 1 μm. This is a result of the fabrication techniques used and cannot be altered. The same structure in Figure 4.2, shows the input port, along with the desired direct output and coupled output ports. So, optimally, for 3 dB coupling, it would be desired to place a signal at port 1 and obtain at least 20 dB return loss along with 3 dB of insertion loss at ports 2 and 4, and better than 40 dB of insertion loss at the isolated port 3.

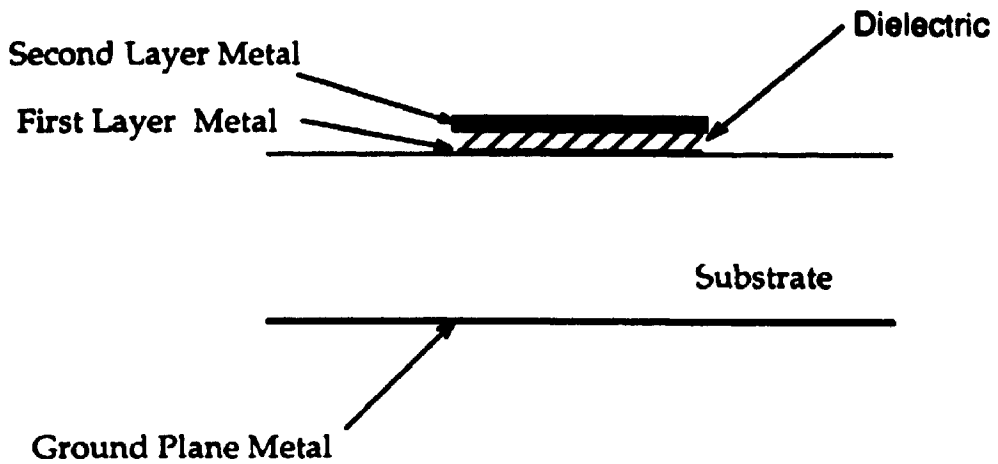

Figure 4.1 Cross-Section of Standard Overlay Coupler

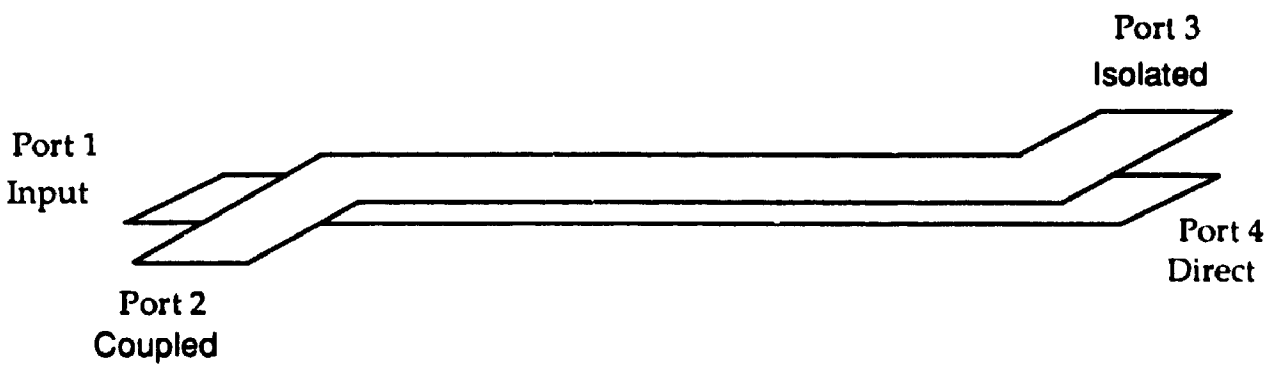

Figure 4.2 Overlay Coupler with the Four Ports

4.2 Analysis

The analysis which has been applied to spiral structures will be modified for the case of the overlay couplers discussed in this chapter. The couplers are very long structures in terms of the guide wavelength and therefore a lumped approach would not be the most suitable method.

Asymmetric coupled transmission line theory[27] will be used to

calculate the Y-parameters of the four-port coupler. The four-port Y-parameters will be obtained by writing the equations for the voltages and currents on the lines in terms of two independent modes. Then the relationship between the voltages and currents will be derived and the appropriate Y-parameters calculated. The analysis for this type of couple. cannot be accomplished using standard even- and odd-mode theory since these two modes cannot propagate independently in a non-symmetrical coupler.

Considering an infinitesimal section of any two-line system with a third line grounded (here the ground plane of the substrate), the equations relating the voltages to the currents on the coupled lines are given by :

$$-\frac{dv_1}{dx} = z_1 i_1 + z_m i_2 \tag{4.1}$$

$$-\frac{dv_2}{dx} = z_2 i_2 + z_m i_1 \tag{4.2}$$

$$-\frac{di_1}{dx} = y_1 v_1 + y_m v_2 \tag{4.3}$$

$$-\frac{di_2}{dx} = y_2 v_2 + y_m v_1 \tag{4.4}$$

The solution for the voltages on the lines is obtained as :

$$v_1 = A_1 e^{-\gamma_c x} + A_2 e^{\gamma_c x} + A_3 e^{-\gamma_\pi x} + A_4 e^{\gamma_\pi x} \tag{4.5}$$

$$v_2 = A_1 R_c e^{-\gamma_c x} + A_2 R_c e^{\gamma_c x} + A_3 R_\Pi e^{-\gamma_\pi x} + A_4 R_\Pi e^{\gamma_\pi x} \tag{4.6}$$

Here R_c represents the ratio of the voltage on the second line to the first line for the γ_c mode and similarly R_π for the γ_π mode. If the lines could be considered lossless, then γ_c and γ_π would correspond to the inphase and antiphase waves.

Solving for the currents on the lines yields :

$$i_1 = A_1 Y_{c1} e^{-\gamma_c x} - A_2 Y_{c1} e^{\gamma_c x} + A_3 Y_{\Pi 1} e^{-\gamma_\Pi x} - A_4 Y_{\Pi 1} e^{\gamma_\Pi x} \tag{4.7}$$

$$i_2 = A_1 R_c Y_{c2} e^{-\gamma_c x} - A_2 R_c Y_{c2} e^{\gamma_c x} + A_3 R_\Pi Y_{\Pi 2} e^{-\gamma_\Pi x} - A_4 R_\Pi Y_{\Pi 2} e^{\gamma_\Pi x} \tag{4.8}$$

where :

$$Y_{c1} = \gamma_c \frac{z_2 - z_m R_c}{z_1 z_2 - z_m^2} \tag{4.9}$$

$$Y_{c2} = \frac{\gamma_c}{R_c} \frac{z_1 R_c - z_m}{z_1 z_2 - z_m^2} \tag{4.10}$$

$$Y_{\Pi 1} = \gamma_\Pi \frac{z_2 - z_m R_\Pi}{z_1 z_2 - z_m^2} \tag{4.11}$$

$$Y_{\Pi 2} = \frac{\gamma_\Pi}{R_\Pi} \frac{z_1 R_\Pi - z_m}{z_1 z_2 - z_m^2} \tag{4.12}$$

A_1, A_2, A_3, and A_4 can be obtained according to the conditions placed on the ends of the two transmission lines. In this case, Y-parameters are desired and therefore the appropriate voltage sources are placed at the ends of the lines and 4.5 and 4.6 are used to solve for the unknowns. The necessary currents are then calculated. Once the currents are known at the end of the lines for a given voltage at an input port, the problem is solved and the Y-parameters can be written. The solution obtained is completely general and can be applied to a coupler with any dimensions as long as it is still operating as a quasi-TEM structure. The Y-parameters are given by :

$$Y_{11} = Y_{44} = \frac{Y_{c1} \coth \gamma_c L}{\left(1 - \frac{R_c}{R_\Pi}\right)} + \frac{Y_{\Pi 1} \coth \gamma_\Pi L}{\left(1 - \frac{R_\Pi}{R_c}\right)} \tag{4.13}$$

$$Y_{12} = Y_{21} = Y_{34} = Y_{43} = -\frac{Y_{c1} \coth \gamma_c L}{R_\Pi \left(1 - \frac{R_c}{R_\Pi}\right)} + \frac{Y_{\Pi 1} \coth \gamma_\Pi L}{R_c \left(1 - \frac{R_\Pi}{R_c}\right)} \tag{4.14}$$

$$Y_{13} = Y_{31} = Y_{24} = Y_{42} = \frac{Y_{c1}}{(R_\Pi - R_c) \sinh \gamma_c L} + \frac{Y_{\Pi 1}}{(R_c - R_\Pi) \sinh \gamma_\Pi L} \tag{4.15}$$

$$Y_{14} = Y_{41} = -\frac{Y_{c1}}{\left(1 - \frac{R_c}{R_\Pi}\right) \sinh \gamma_c L} - \frac{Y_{\Pi 1}}{\left(1 - \frac{R_\Pi}{R_c}\right) \sinh \gamma_\Pi L} \tag{4.16}$$

$$Y_{22} = Y_{33} = -\frac{R_c Y_{c2} \coth \gamma_c L}{R_\Pi \left(1 - \frac{R_c}{R_\Pi}\right)} - \frac{R_\Pi Y_{\Pi 2} \coth \gamma_\Pi L}{R_c \left(1 - \frac{R_\Pi}{R_c}\right)} \tag{4.17}$$

$$Y_{23} = Y_{32} = \frac{R_c Y_{c2}}{R_\Pi \left(1 - \frac{R_c}{R_\Pi}\right) \sinh \gamma_c L} - \frac{R_\Pi Y_{\Pi 2}}{R_c \left(1 - \frac{R_\Pi}{R_c}\right) \coth \gamma_\Pi L} \tag{4.18}$$

The model for an infinitesimal length of the overlay coupler structure can be seen in Figure 4.3. The bottom plate of the coupler is modeled by the elements M_{11}, R_1, and C_{01}, where M_{11} is the self inductance of the bottom plate/unit length, R_1 is the resistance of the bottom plate per unit length, and C_{01} is the self capacitance to ground of the bottom plate in the presence of the top plate. The values subscripted 2 refer to the equivalent values for the top plate. M_{12} is the mutual inductance/unit length

between the top and bottom plates of the coupler. Similarly, C_{12}, is the mutual capacitance between the two plates. The method used to calculate the values for each group of elements will be discussed now.

The values M_{11} and M_{22} are calculated according to the fundamental equation given for the inductance of a rectangular strip in chapter two. Since the two lines are almost touching, it can be assumed that their mutual inductance will be given by

$$M_{12} = \sqrt{M_{11}M_{22}} \tag{4.19}$$

The method outlined in the paper "An Experimental Verification of a Simple Distributed Model of MIM Capacitors for MMIC Applications" is used to calculate the capacitive values in the model.

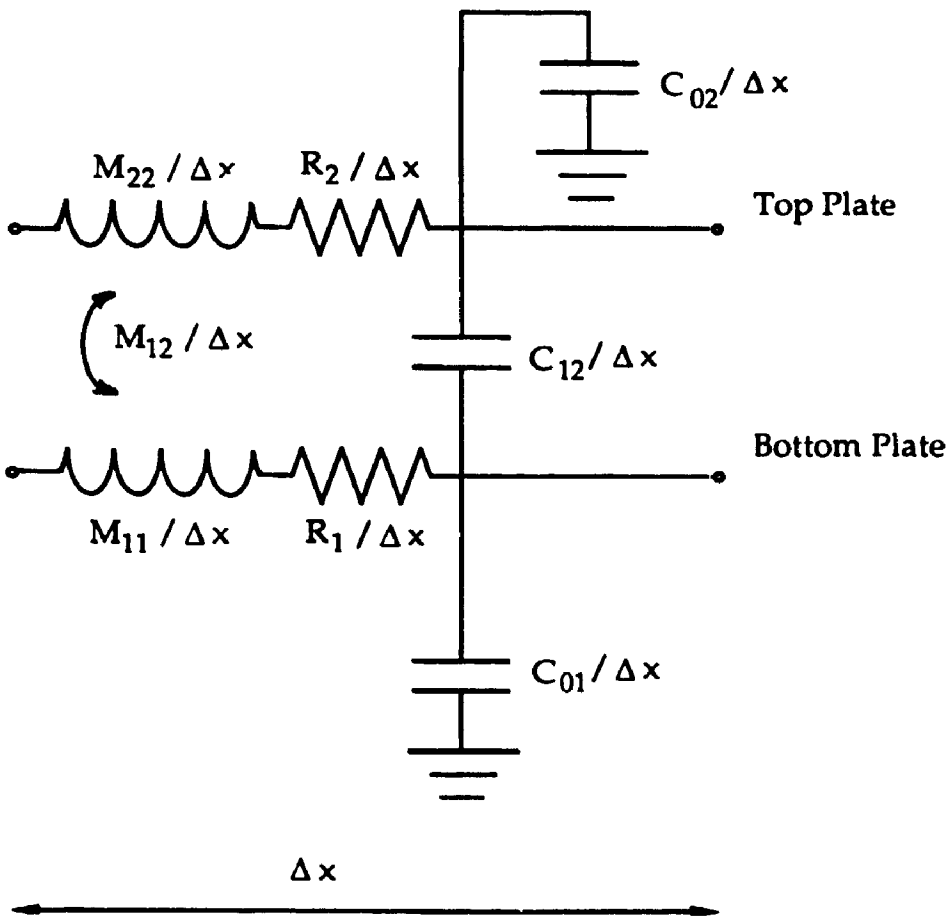

Figure 4.3 Model of Overlay Coupler for Length Δx

The capacitance values for the model in the above figure are calculated according to the method outlined by J.P. Mondal [28] which is used for thin-film capacitors. The parallel plate capacitance between the top and bottom layers is used to model C_{12}/unit length. Its value is given by :

$$C_{12} = \varepsilon_0 \varepsilon_{r,dielectric} \cdot \frac{W}{T_{dielectric}} \tag{4.20}$$

The values for C_{01}/unit length and C_{02}/unit length are calculated assuming that the overlay coupler is just a single transmission line on top of the substrate with a combined thickness of the top and bottom layers of the coupler. Using the capacitances of an equivalent stripline[29] and microstrip line, the desired quantities can be determined. Assuming half the capacitance of the stripline of Figure 4.4 is given by :

$$C_1 = \frac{1}{2}\left(\frac{Z_{stripline} v_{air}}{\sqrt{\varepsilon_r}}\right)^{-1} \tag{4.21}$$

Then the total capacitance of the equivalent microstrip line (Figure 4.5) is given by :

$$C_{total} = \left(\frac{Z_{microstrip} v_{air}}{\sqrt{\varepsilon_{eff,microstrip}}}\right)^{-1} \tag{4.22}$$

Hence, C_{01} and C_{02} can be calculated.

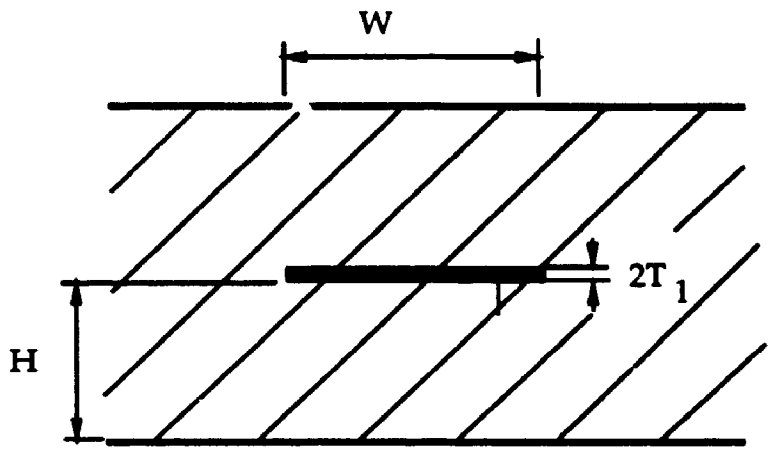

Figure 4.4 Stripline Structure

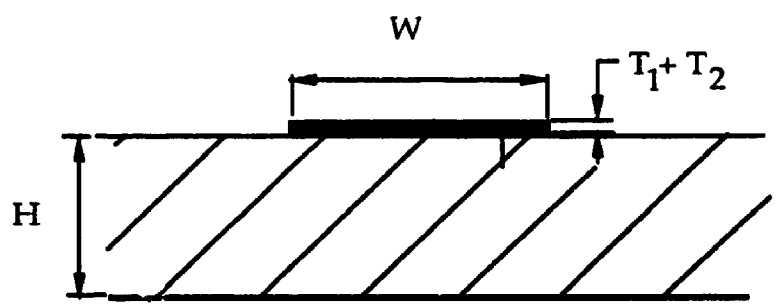

Figure 4.5 Microstrip Structure

The value C_{01}/unit length is given by :

$$C_{01} = C_{par} + (C_1 - C_{par}) \cdot \frac{\varepsilon_{eff}}{\varepsilon_{r,substrate}} \tag{4.23}$$

with :

$$C_{par} = \varepsilon_0 \varepsilon_{r,substrate} \cdot \frac{W}{H} \tag{4.24}$$

and, C_{02} by :

$$C_{02} = C_{total} - C_{01} \tag{4.25}$$

The equations for the resistive values R_1/unit length and R_2/unit length come from the same resistance equations used for the other structures. The values used in the paper mentioned are essentially based on DC resistances. The Pettenpaul resistance equations have a slightly better applicability here because frequency dependence is taken into account, although in reality the resistance of the top plate is affected by the proximity of the bottom plate and vice versa.

4.3 Results and Discussion

A photograph of an overlay coupler which was fabricated on Alumina, measured and analyzed can be seen in Figure 4.6. As stated in the introduction, all of the couplers measured were four-ports. The S-parameters were measured between any two ports at a time; the other two ports being terminated with 50 Ω loads. For instance when measuring S_{21}, ports 3 and 4 of the coupler would be terminated. Results are given in Figure 4.7 for an overlay coupler on 0.010" alumina substrate, with an overall length, L =1500 μm, width, W=15 μm, plate separation, $T_{dielectric}$=0.20 μm, and dielectric permittivity, $\varepsilon_{dielectric}$=7.0 .

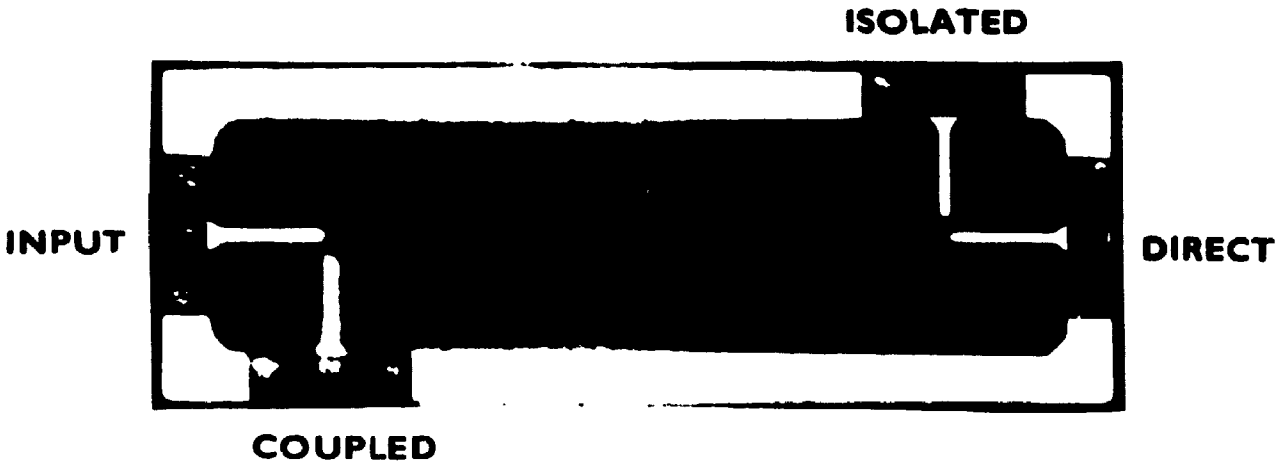

Figure 4.6 Photograph of Overlay Coupler on Alumina Substrate

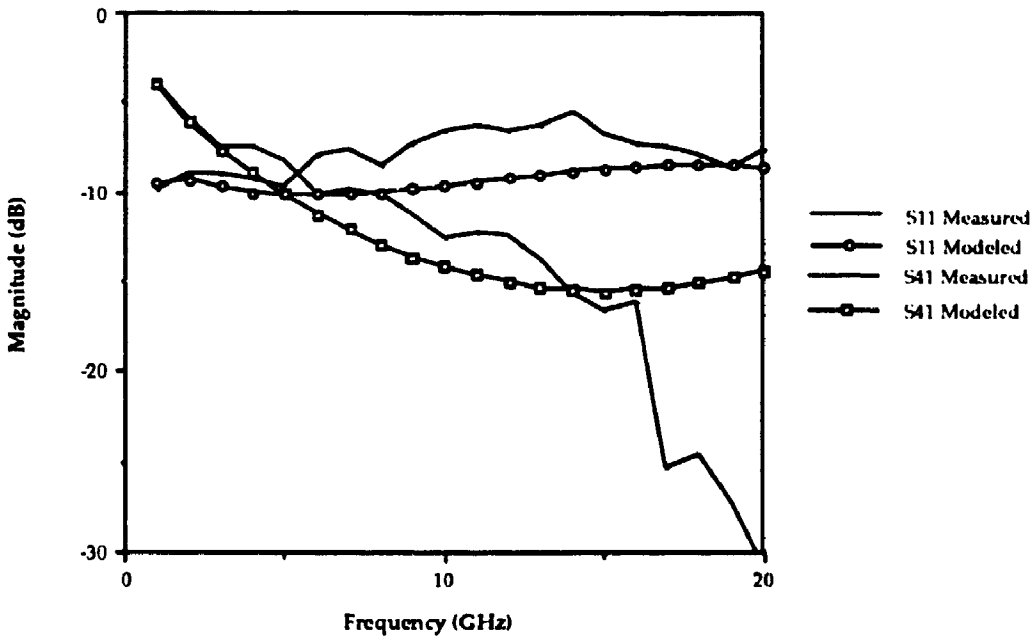

Figure 4.7a Power at Input Port and Direct Port vs. Frequency

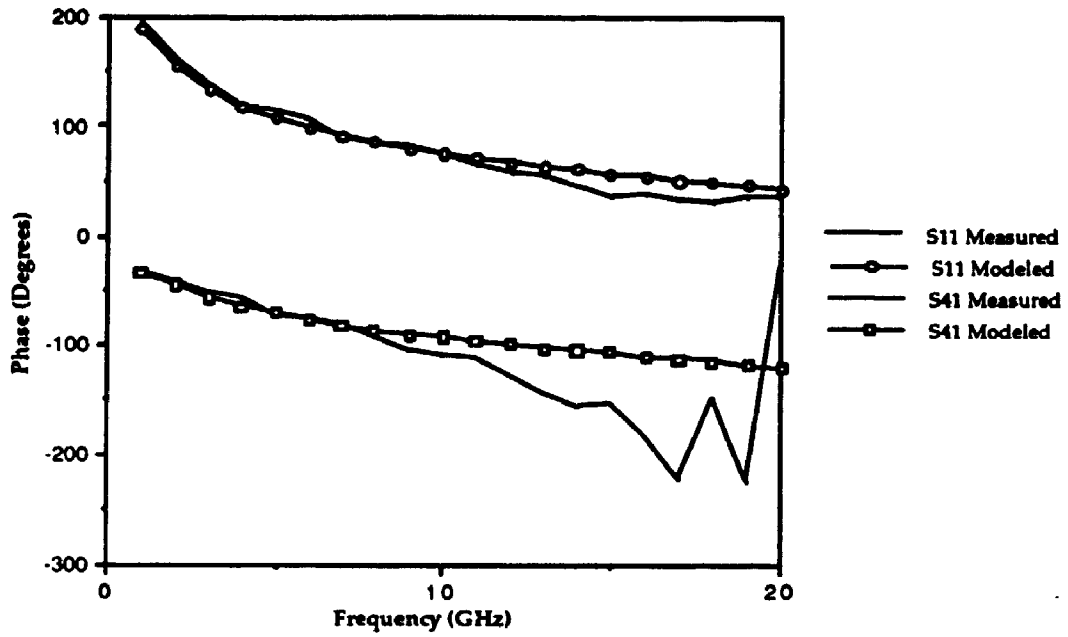

Figure 4.7b Phase at Input Port and Direct Port vs. Frequency

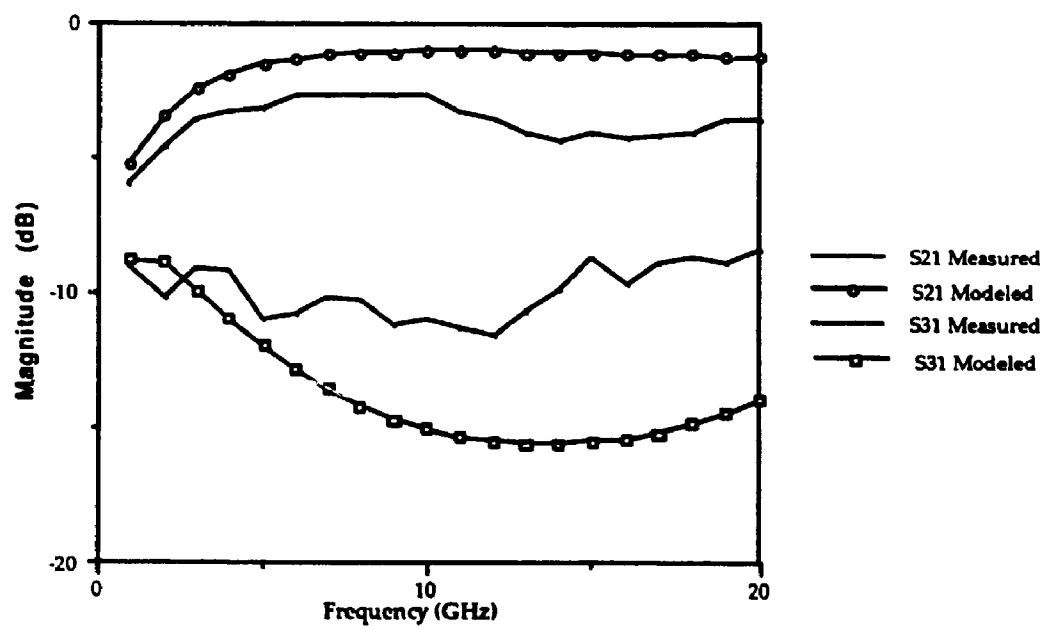

Figure 4.7c Power at Coupled Port and Isolated Port vs Frequency

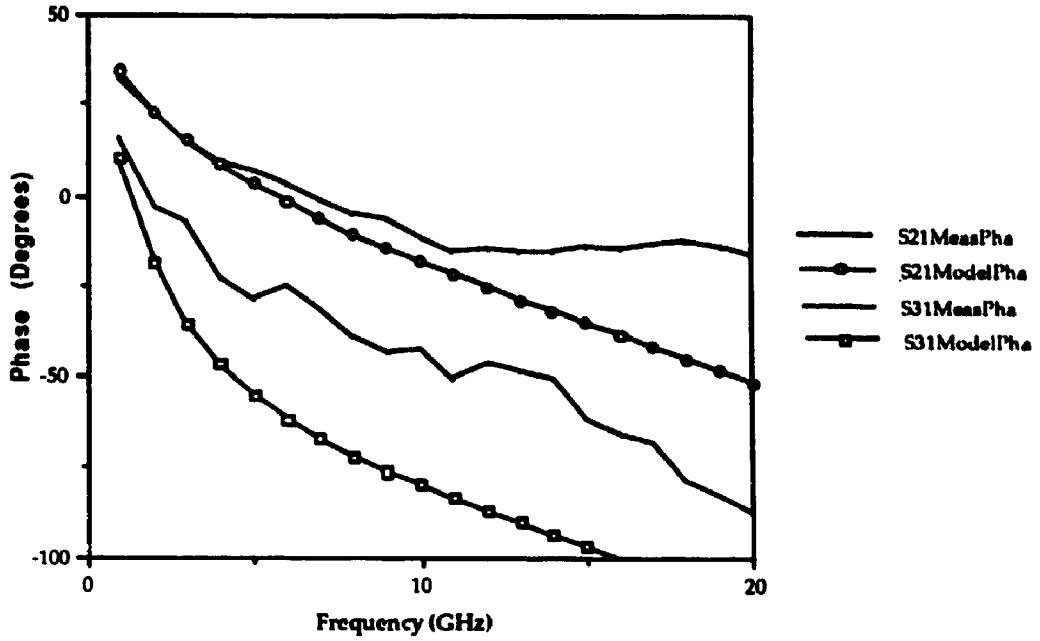

Figure 4.7d Phase at Coupled Port and Isolated Port vs Frequency

The same coupler fabricated on a quartz substrate was also measured and analyzed. Its model values can be seen in the Table 4.1 below and the results are shown in Figure 4.8. It can be noticed that R_1 is almost twice R_2 because of the smaller thickness of the bottom plate of the overlay coupler. Also, the effect of the bottom plate shielding the top plate of the coupler is brought out by observing that C_{01} is twice C_{02}.

Table 4.1
Model Element Values for Coupler
on Quartz Substrate

Element	Value
R_1	0.0043 Ω/μm
R_2	0.0022 Ω/μm
M_{11}	0.0013 nH/μm
M_{22}	0.0013 nH/μm
M_{12}	0.0013 nH/μm
C_{01}	0.0304 fF/μm
C_{02}	0.0150 fF/μm
C_{12}	0.0260 pF/μm

The results for the coupler can be seen in the set of figures below.

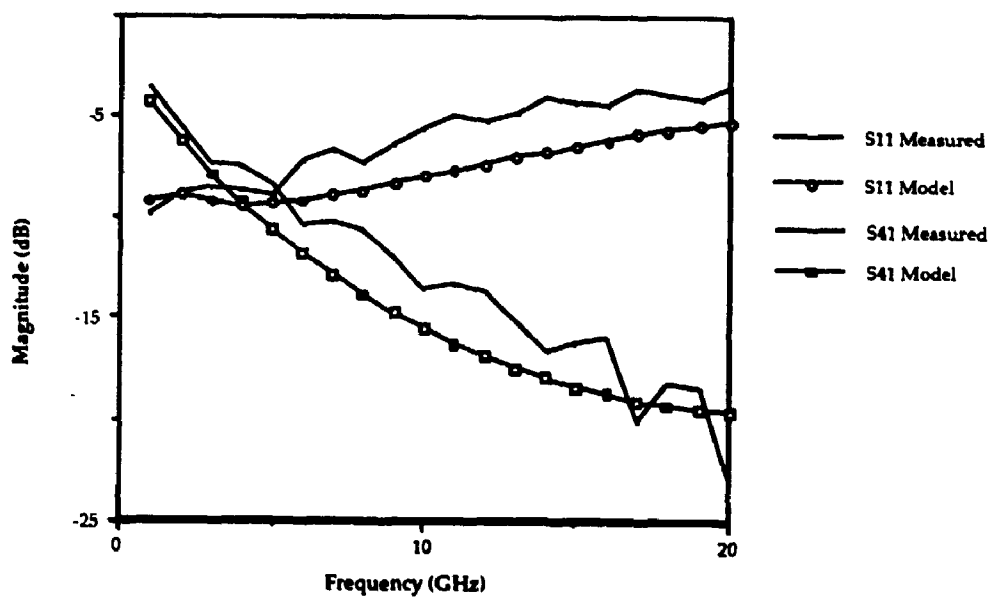

Figure 4.8a Power at Input Port and Direct Port vs. Frequency

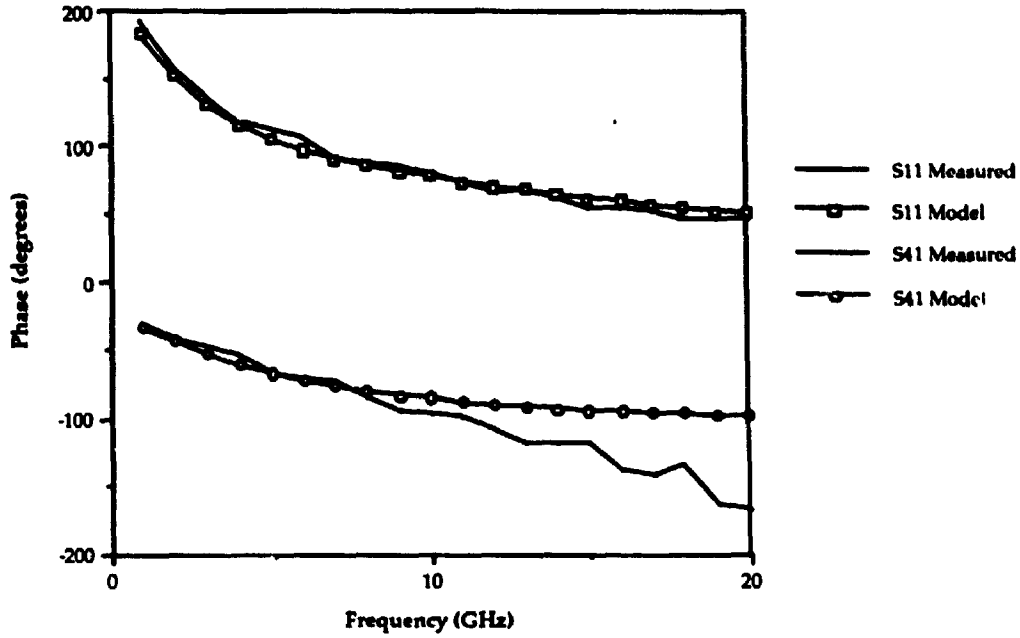

Figure 4.8b Phase at Input Port and Direct Port vs. Frequency

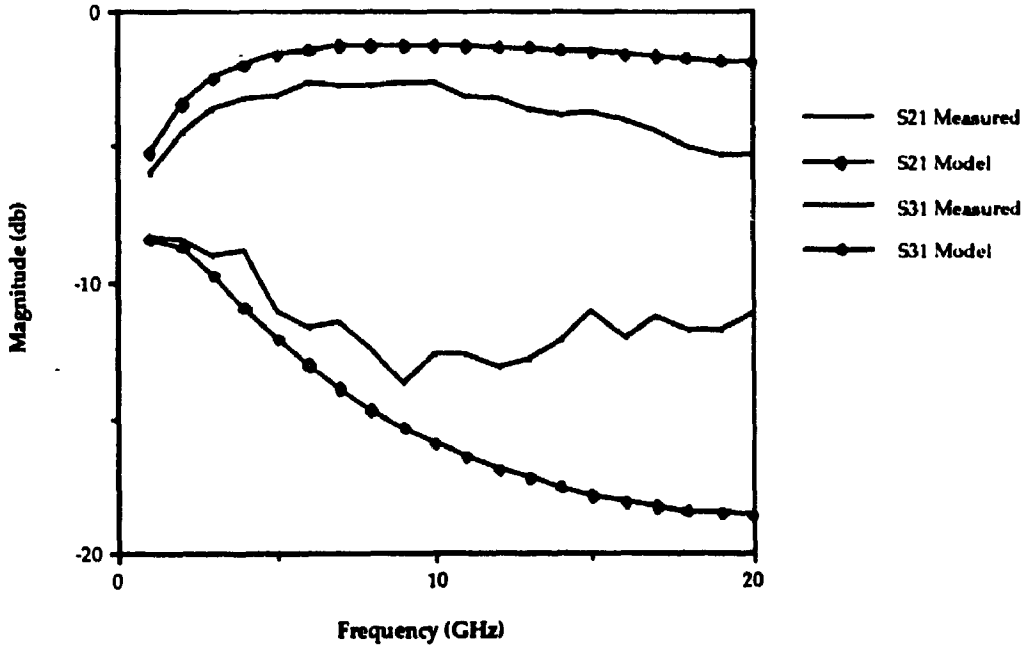

Figure 4.8c Power at Coupled Port and Isolated Port vs. Frequency

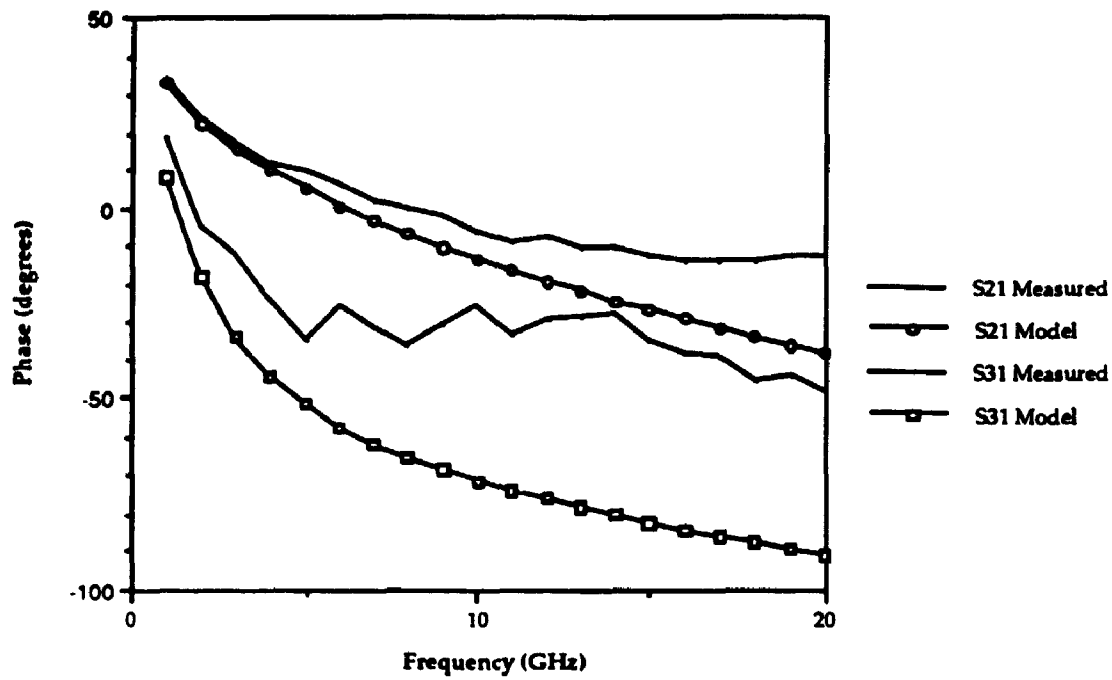

Figure 4.8d Phase at Coupled Port and Isolated Port vs. Frequency

Comparing the theoretically calculated S-parameters to the measured results, it can be seen that fairly good agreement is obtained for S_{11} and S_{41} over the frequency range from 1 to 10 GHz. The results for S_{21} and S_{31} are not as good. For S_{21}, which represents the power to the coupled port, it can be noticed that the model overpredicts the power by approximately 1.5 dB. This is believed to come about from the dispersion which is taking place in the structure. The major effect of the dispersion is to cause the C_{12} value used in the model to be lower than expected and therefore the coupled power should actually be slightly lower than calculated. For the measurements of power from the input port to the isolated port, the model predicts better isolation than is actually obtained.

Some general observations can be made from the results for the two couplers on the different substrates. First, all of these couplers have their

maximum coupling at the lowest frequency measured (ie. 1 GHz). They couple maximum power to the coupled port at some higher frequency, which can be seen to be around 10 GHz for these structures. For these couplers, at the frequency of maximum coupling, the direct power typically can have an insertion loss of 12 to 15 dB. Also the power to the coupled port undergoes an insertion loss of 3 dB. The same phenomenon is observed by Robertson and Aghvami [30]. They have measured the same type of structure on a GaAs substrate for possible use as an MMIC coupler. Their measured results show that for maximum coupling which occurs at 5 GHz, the insertion loss to the coupled port is 2.5 dB and the insertion loss to the direct port is 7dB.

It can be seen that the isolation of the couplers is quite poor. The measured isolation at the frequency of maximum coupling can be as low as 10 dB. This is a general property for this type of overlay coupler. The lower than desired isolation can be attributed to the nonsymmetric nature of the structure.

Comparing the alumina substrate and quartz substrate couplers, it is discovered that their direct and coupled power are approximately the same. The coupler built on the quartz substrate has poorer return loss but slightly better isolation.

When performing the calculations for the quartz substrate overlay coupler, it is found that $R_c = 1.043 - j0.027$ and that $R_\pi = -0.600-j0.184$. For the non-degenerative case of the R_c and R_π modes, their values are 1.0 and -1.0. However, here it can be seen that the R_π mode degenerates to a value quite different from -1.0, even though the even phase mode is quite close to 1.0 . This fact demonstrates the essential reason why the solution of the overlay couplers must be handled in the above-mentioned manner: the R_π mode degenerates because the capacitance C_{01} to ground is usually twice the capacitance C_{02} to ground, and this causes the passive device to become unbalanced.

As seen from the results, the couplers are quite broadband and could be

used in various microwave circuits. However, due to the general nature of the couplers, it is believed that they will not be able to function as 3 dB couplers in which the input power to the coupler would be split evenly between the two output ports and with acceptable isolation.

5 Class A Pushpull Amplifier Design Using Center-Tapped Transformers

5.1 Introduction

An MHMIC amplifier is discussed in this chapter which uses center-tapped transformers to couple power into, and out of the circuit. As well a novel DC biasing technique is used in which the voltage is applied directly to the transformer secondary center-tap.

To date the only work reported using transformers in microwave amplifiers is that of D. Ferguson et al[24]. They used a center-tapped transformer to couple power between the stages of their FET amplifier. A schematic of their eight-FET circuit can be seen in Figure 5.1.

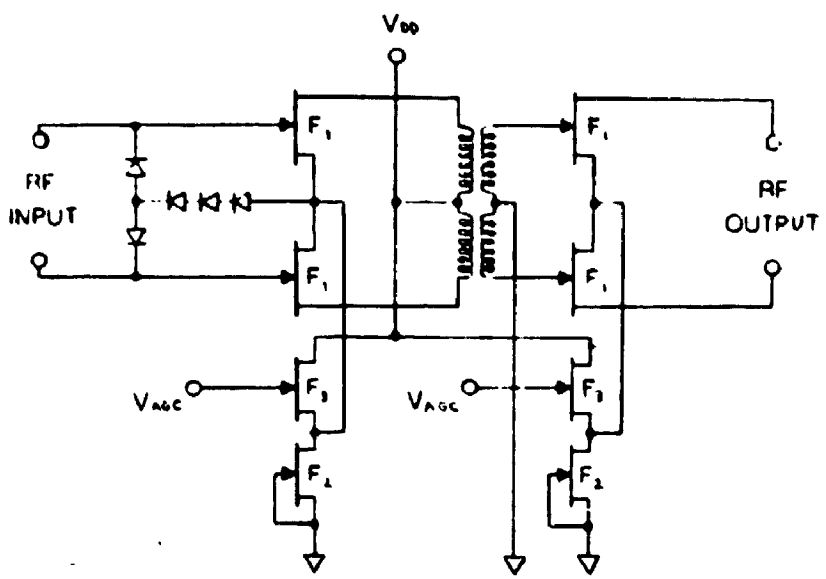

Figure 5.1 Ferguson's[24] Transformer Coupled Pushpull Amplifier

Here the four F_1 FETs perform the actual amplification in the circuit. The two FETs labelled F_2 are effectively current sources which are used to bias the F_1 FETs to 15% I_{dss}. F_3 are used as a means to change the overall

gain of the circuit by taking some current away from the F_1's. The center-tapped transformer can be seen to be used as a method to couple power to the second stage of the amplifier without using capacitors which would have to be abnormally large. The authors used 3 μm track spaces with the transformers and claim an expected coefficient of coupling of K=0.86 which is questionable. Even with this level of perfomance the author admit that the match between the stages is not conjugate, even though sufficient gain is given by the amplifier. The measured gain was found to be approximately 9 dB at a frequency of 4.4 GHz[23].

A push pull amplifier based on the use of the center-tapped transformers was designed and fabricated. Although it is not a two-stage amplifier, it is an excellent demonstration of a possible use for a center-tapped transformer in an amplifier. The particular amplifier designed here is Class A. Although pushpull amplifiers are better suited for Class B or Class AB operation, where the two active devices in the amplifier produce the most power possible, the analysis for this case is severely complicated. The basic schematic of the pushpull amplifier can be seen in Figure 5.2.

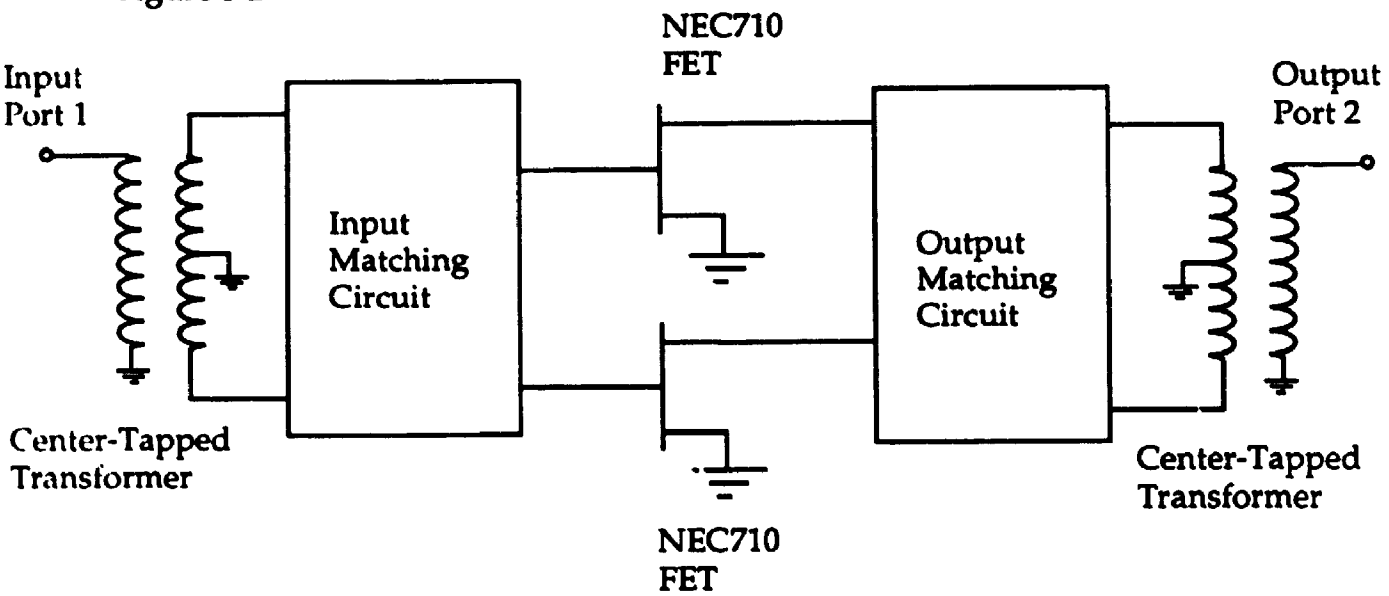

Figure 5.2 Schematic of Standard Pushpull Amplifier

The circuit consists of an input center-tapped transformer, an input

matching circuit, two active devices (here FETs), an output matching circuit, and an output center-tapped transformer. The input center-tapped transformer takes the signal at port one and produces a biphase sigal at its two output ports into the matching circuit. The input matching circuit is then used to try to minimize the return loss of the amplifier by matching the transformer to the gate capacitance, C_{gs}, of the FET. The output of the FET's are similarly matched to the output center-tapped transformer for the same reason. The two signals are combined in the output transformer and an output signal is obtained

The above-mentioned amplifier topology is different than the wide-band balanced amplifier topology[31],[32] in which 3-dB couplers are used to couple power into and out of the two FETs. Although, using couplers makes the design larger in bandwidth, the extra real-estate required is significant and would therefore be a drawback where space is limited.

5.2 Analysis and Discussion

The circuits are designed using MHMIC technology. Therefore the matching circuits contain standard lumped element inductors and capacitors. Distributed elements are avoided in most MHMIC designs due to their excessive use of real estate on a substrate. The FETs used for the design are the standard NEC 710[33]. The schematic of the amplifier is shown in Figure 5.3.

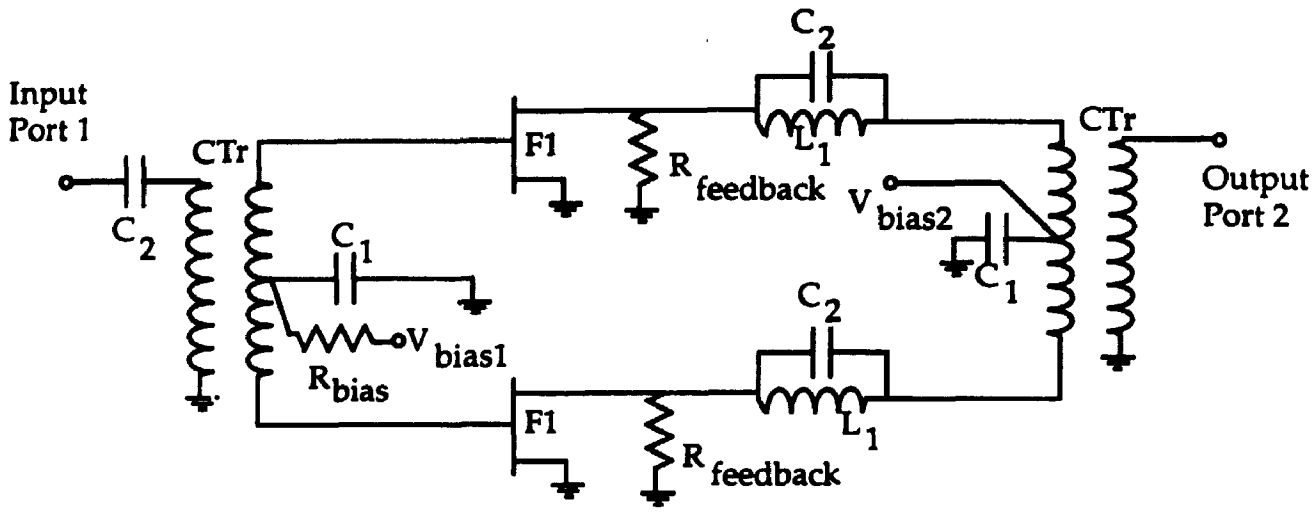

Figure 5.3 Schematic of 8 GHz MHMIC Pushpull Amplifier

Since the circuit has been designed with center-tapped transformers, the RF signal is isolated from the DC bias voltage at the input and output, simplifying circuit design. Furthermore the FETs are biased through an LC circuit where the L is provided by the self inductance of the transformer secondary, and the C by a large thin-film capacitor. Since the transformers are only 1:1 transformers they cannot be used for any real matching themselves. This means more components in the final circuit as well as a drop in the possible output power of the amplifier because of additional losses. Still, the transformers demonstrate one of their possible applications.

The amplifier's objective is to operate at 8 GHz with 5 dB of gain. Since the broadband matching of standard square spiral transformers is very difficult, the achievable bandwidth of operation of the amplifier is quite small.

The high insertion loss of the transformers affects the power output of the circuit quite severely. Also, the low coupling factor between the two spirals of the transformer is another limiting factor. Although the track spacing can be made smaller than the 10 μm used, the increase in ohmic losses is not acceptable. With spacings smaller than 5 μm other factors such as current crowding near the edges of the transmission lines occurs

which is not taken into account in the SSTR model.

The only new circuit element used here which has not been previously discussed is the via hole. This is a structure used to obtain contact to the microstrip ground plane at some desired point in a microstrip circuit. If via holes are not used, then the only alternative is to ground the circuit through the coplanar ground probes as has been done for the measurement of all the individual passive components up to this point. The via hole is fabricated by completely boring through the substrate material using either a laser driller or an ultrasonic driller. The laboratory at CRC provides ultrasonically-drilled via holes. The via hole fabrication is the first step in the processing of a wafer. After the holes have been physically drilled, they are gold-plated in order to obtain a contact to the underside ground plane of a substrate.

The presence of a 300 Ω feedback resistor at the drain of each of the two FETs provides increased stability. Although the resistors decrease the gain of the final amplifier circuit, their presence in the circuit significantly simplifies the design of the amplifier. Without the resistors the FETs have a tendency to oscillate in the L band frequency range.

The S-parameters for the center-tapped transformer used in this design are obtained from the SSCN model discussed in chapter 3. The input circuit is designed such that the inductance of the transformer secondary will resonate with the capacitance of the gate in order to minimize the return loss at that frequency. The value of C_{gs} resonating with the secondary inductance to ground of 1.0 nH gives a resonant frequency of 9 GHz. This is slightly off the value of 8 GHz because the value given is for the final optimized circuit. The input series capacitor, C_2, having a value of 1.6 pF, was chosen to produce a slightly better S_{11} frequency response in the range of interest.

For the output side of the FETs, it can be seen that a parallel LC resonant circuit is used. The main purpose of the 2-1/2 turn inductors is to provide a conjugate match to the two inputs of the center-tapped transformer. Looking into the drain with the given input matching

network, the output reflection parameter is given by S_{22}=0.642@θ= 44.5 deg. In order to match to the transformer, the impedance looking into the matching circuit must be the complex conjugate impedance. An inductor of 2.0 nH was used in order to improve the match slightly between the center-tapped transformer having an S_{11}=0.86@θ= 89.0 deg. The presence of the capacitor in the circuit results in slightly more broadband design.

During the design of this amplifier, an attempt was made to minimize the number of passive components. The input and output matching stages can be made more complicated, but it is found that doing this does not significantly improve the amplifier characteristics.

Table 5.1
Component Values of Pushpull Amplifier

Element	Value	Size
CTr	-	2-1/4 turn, 310μm x 310μm, width=12μm, spacing=12μm
F_1	-	NE710 FET
L_1	2.0 nH	2-1/2 turn, 250μm x 250μm, width=13μm, spacing=10μm
C_1	19.4pF	250μm x 250μm
C_2	1.03pF	60μm x 60μm
$R_{feedback}$	300Ω	-
R_{bias}	1200Ω	-

The final layout of the small signal pushpull amplifier is presented in Figure 5.6 and the values of the various elements used, are given in Table 5.1. The input port is at the left side of the figure and the output can be found at the right side of the figure. The large circles on the diagram are the positions for the ultrasonic drilling of the via holes in the substrate.

The position of the two FETs will be in the center of the figure, near the via holes. Bond wires will be used to make the connection from the various pads on the substrate to the actual contacts on the FETs.

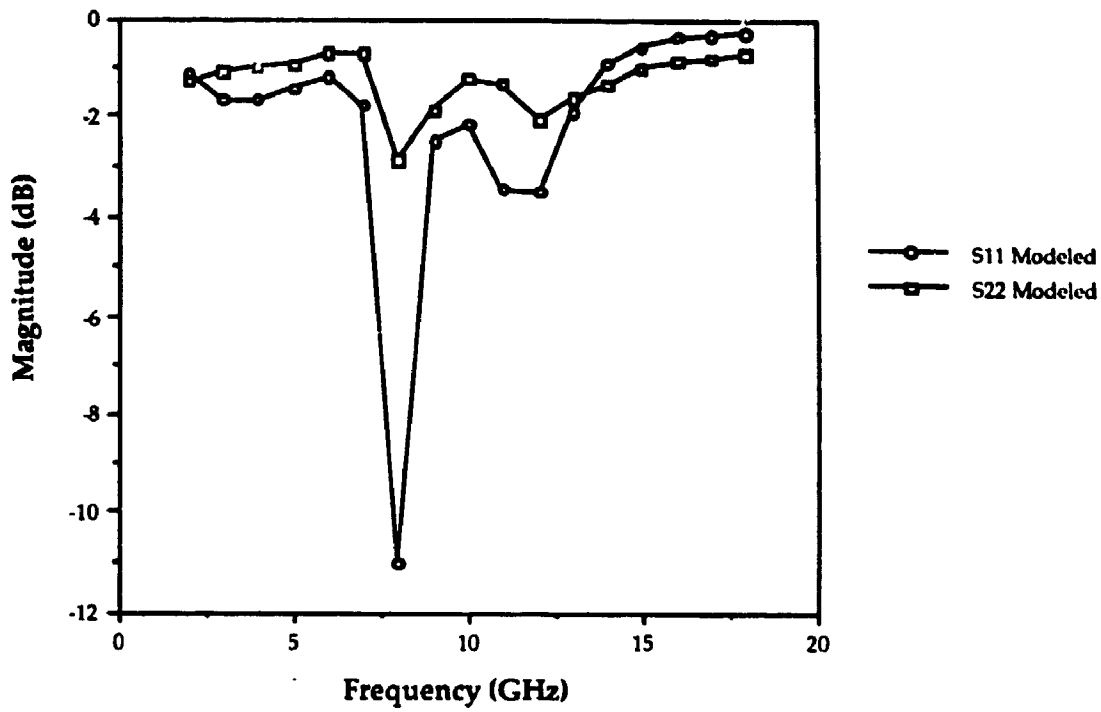

Figure 5.4 Input and Output Match of the Pushpull Amplifier

Figure 5.4 shows the modeled input and output return loss of the amplifier as a function of frequency. At the design frequency of 8 GHz the magnitude of S_{11} is -12 dB and the magnitude of S_{22} is -3dB. These values demonstrate the difficulty encountered when designing this type of amplifier. The FET S-parameters were taken for the DC bias case in which V_{DS} is 3V, and I_{DS} is 10mA. Although the current through the FET could be increased, this was not done, in order to keep noise figure low. For this bias position of the FETs, the overall noise figure was calculated (using

SuperCompact) to be 3.5 dB at 8GHz, which is acceptable.

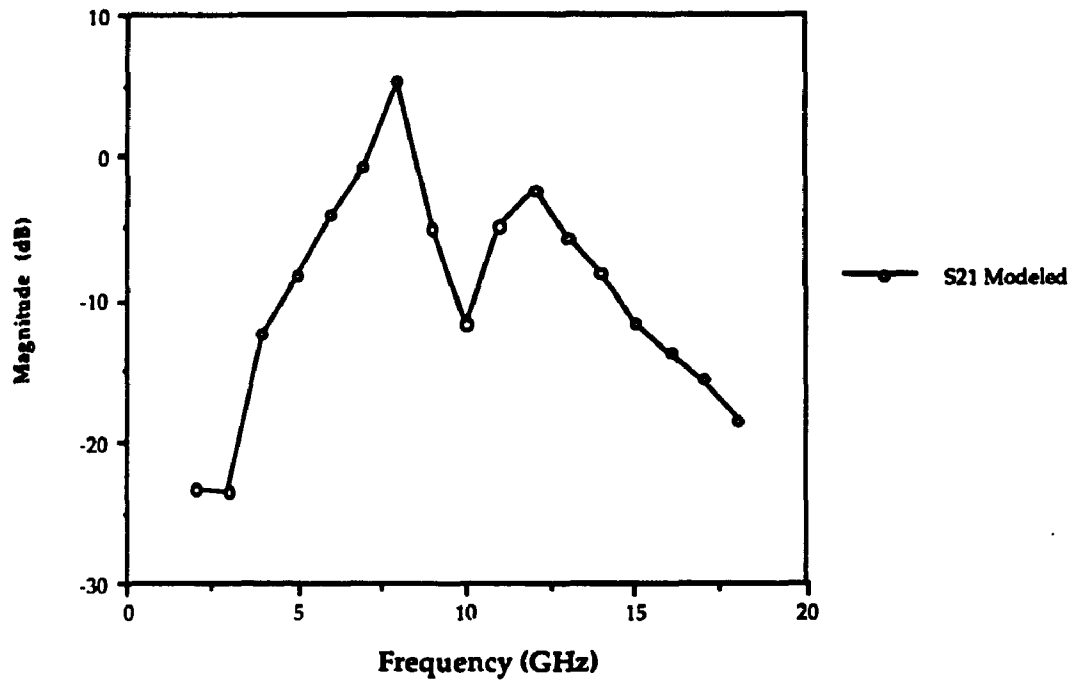

Figure 5.5 Gain of the Push Pushpull Amplifier

The gain curve of Figure 5.5 shows a maximum value of 5.1 dB at 8 GHz. From the modeled result it can also be seen that the amplifier bandwidth is not extremely large. At frequencies 1 GHz below, and above 8 GHz, the gain has already dropped to 0 dB. With a more involved design the bandwidth of the amplifier could probably be extended over several GHz. However as a first demonstration of the new center-tapped transformer technology, it was desired to keep the circuit simple in order to discover the source of possible problems with the circuit.

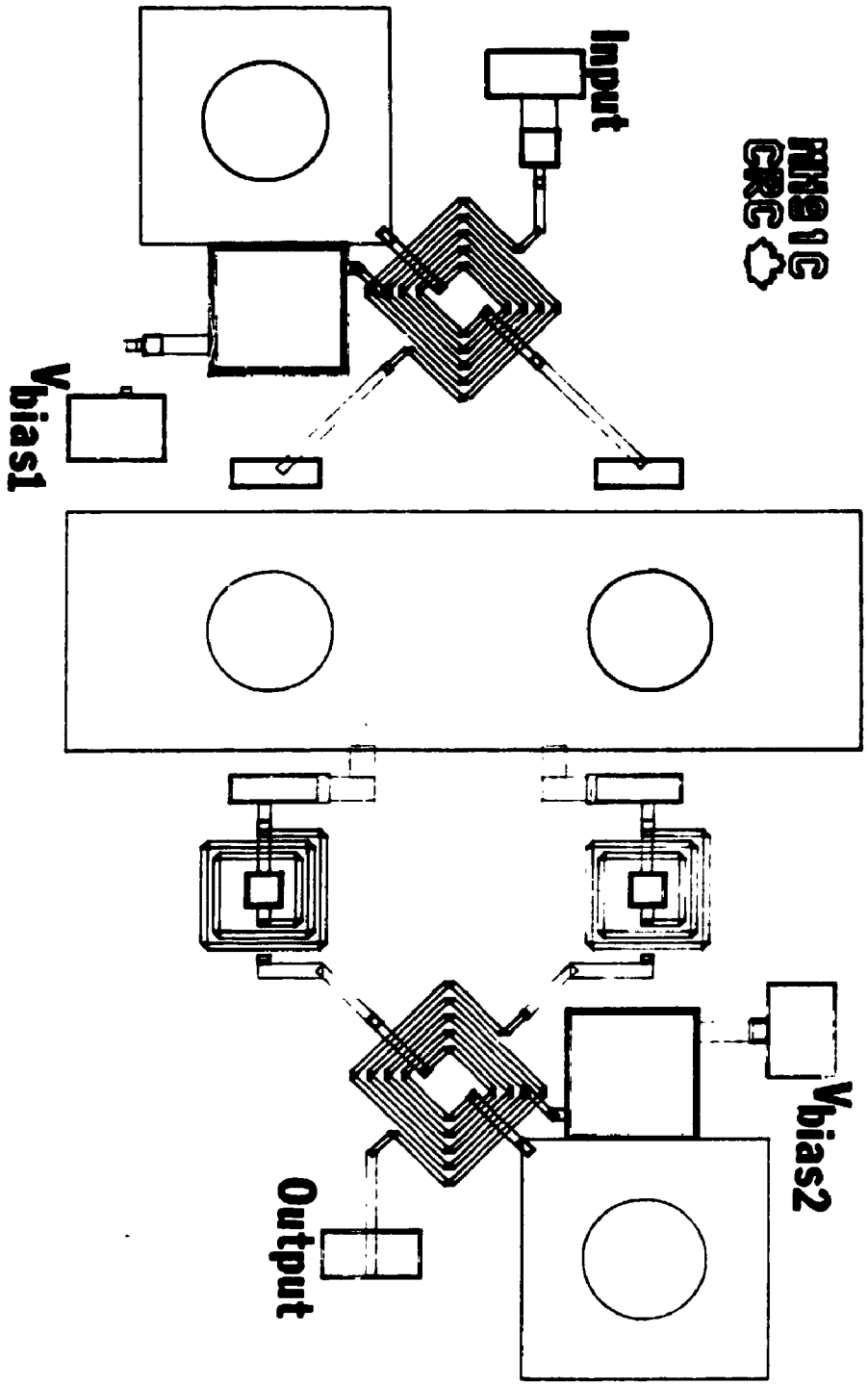

Figure 5.6 Layout of MMHIC Balanced Amplifier

6 Conclusions

6.1 Conclusions and Recommendations

This thesis has analyzed several passive structures for eventual use in MHMIC microwave modules. The emphasis of the thesis has been on the proper lumped element modeling of the passive structures before inclusion in more complex circuits.

Emphasis was placed on the investigation of the square spiral inductors were discussed in chapter 2 because of the large importance they play in many microwave circuits as a matching element. The spirals were successfully modeled to their first resonant frequency using a novel lumped element approach. The model contained frequency dependent variables in order to accurately extend the range of the model significantly above several gigaHertz. Each of the different types of elements found in the lumped element model were discussed separately. It was then described how the method was integrated into a computer program, called SSPI (square spiral inductor), which was installed in SuperCompact.

A study of how to optimize the inductor results was undertaken to provide an insightful understanding of this basic planar microwave structure. It was found that for inductors with a small number of turns, the inductance would not be increased significantly by decreasing the track spacing. For inductors with a large number of turns it was found that the inductance could be almost doubled by decreasing the spacing from 30 μm to 5 μm.

Since the inductors were accurately modeled to their first resonant frequency, they could be used confidently in linear amplifiers up to this frequency.

A basic application of the square spiral inductors and thin-film capacitors was in a lumped element delay line. Two delay lines were

fabricated; 250 ps and 500 ps versions. It was found that the time delays measured agreed with what was expected from the devices. They were found to operate better when the thin-film capacitors used were grounded to both sides of the coplanar ground, rather than to only one side. Therefore, if via holes are not to be used with this type of circuit, it is recommended to ground to both sides of the coplanar probe.

The method used to analyze the inductors was extended to square spiral transformers, as discussed in chapter 3 of the thesis. A frequency dependent lumped element model was formulated which accurately predicted the transformer S parameters to at least their first resonant frequency. As with the inductors, each of the elements used in the model were discussed separately. The model was then also integrated into a user-defined model for non-center-tapped transformers called SSTR (square spiral transformer).

Further, a model was developed for the specialized case of a center-tapped transformer which could have possible applications in a pushpull amplifier. The results for several of the transformers were presented and the conclusion was drawn that the transformers generally had a large bandwidth of inductive coupling, typically 0.5 octaves, but that the coupling coefficient, k, was found to be too small, having a value of 0.4 to 0.6 (depending on the transformer dimensions). In order to improve the general performance characteristics of the transformers, it is required that they have more turns, and that the spacing between the lines be decreased. Fabricating the transformers with thicker gold would also improve the Q factor of the transformers significantly.

The accuracy of the inductor and transformer models in the upper frequency range can be improved by including several higher order effects. For instance, the coupling of the airbridge to the underside tracks can be included directly in the models instead of assuming that the airbridge acts only as a transmission line. The capacitance formulae assume that there is negligible coupling between non-adjacent segments of a structure. For increased accuracy, more complicated analyses can be used so as to also

include the small capacitive coupling between non-adjacent segments. Also, the ohmic and loss tangents can be calculated by using a method which will calculate the even- and odd-mode losses of the coupled lines. As well, the proximity effect of the coplanar ground lines can be taken into account.

The study of thin-film overlay couplers was undertaken in chapter 4 with the goal to obtain a 3 dB coupler .A model for an infinitesimal section of the coupler was developed to calculate the Y-parameters of the four-port coupler. Measurements of the fabricated couplers was undertaken and the model was found to have fair agreement with the measured return loss and direct power through the coupler. However, the coupled and isolated power increased in error with frequency due to the fact that dispersion was not taken into account in the model. Also, the resistance values used in the model were not the even- and odd-mode values required for increased accuracy. The couplers were found to have potential as weak couplers but not as 3 dB couplers.

A class A pushpull amplifier was designed for fabrication on 0.010" Alumina substrate using two center-tapped transformers. It was found that designing circuits with these types of transformers was quite difficult because they are not matched to 50 Ω on their own. The expected gain of the amplifier designed was 6 dB at 8 GHz.

Appendix I

The Y-parameters for the inductor can be determined according to their basic definition. Applying a voltage source to one of the ports of the device, and shorting out all of the other ports, the current produced at each port must be determined. Taking the example of a two-port in the figure below, a voltage source is being applied to port 1.

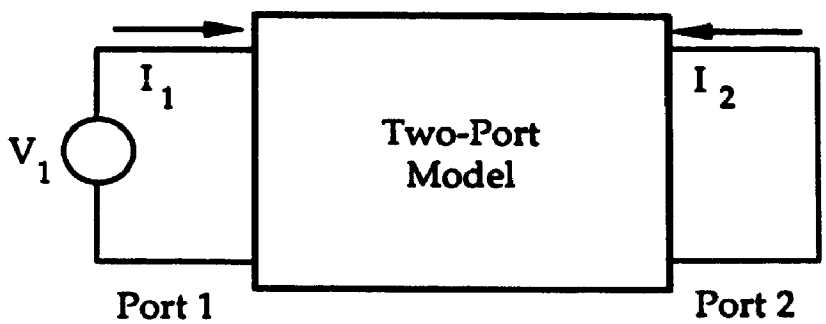

Figure I.1 Schematic of a Two-Port for Y Parameter Calculation

A knowlege of the current produced at ports 1 and 2 is sufficient to determine the Y_{11} and Y_{21} parameters according to the following equations :

$$Y_{11} = \frac{I_1}{V_1} \tag{I.1}$$

$$Y_{21} = \frac{I_2}{V_1} \tag{I.2}$$

Similarly, if the voltage source is moved over to port 2 and port 1 is short-circuited, then the parameters Y_{12} and Y_{22} can be determined according to:

$$Y_{12} = \frac{I_1}{V_2} \tag{I.3}$$

$$Y_{22} = \frac{I_2}{V_2} \tag{I.4}$$

Taking the actual model used for the inductor (Figure 2.4), and applying a voltage source to port 1 and a short to port 2, the schematic diagram of Figure I.2 is obtained along with the loop currents I_1 and I_2.

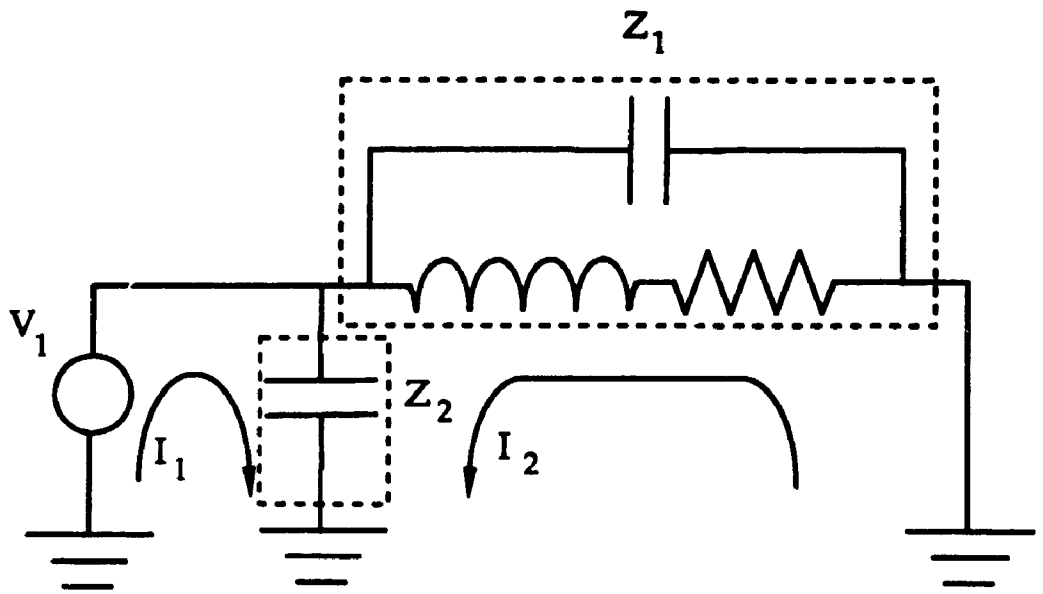

Figure I.2 Inductor Schematic Used to Calculate Y_{11} and Y_{21}

The presence of C_{02} for the calculation of Y_{11} and Y_{21} has been eliminated due to the fact that port 2 is shorted to ground.

Solving the above circuit for the currents I_1 and I_2, the following parameters are obtained :

$$Y_{11} = \frac{1 - \omega^2 L\,(C_f + C_{01}) + j\omega R\,(C_f + C_{01})}{R + j\omega L} \tag{I.5}$$

$$Y_{21} = -\frac{1 - \omega^2 L\,C_f + j\omega R\,C_f}{R + j\omega L} \tag{I.6}$$

Similarly, solving the other case so that Y_{12} and Y_{22} can be found, the following is obtained :

$$Y_{12} = -\frac{1 - \omega^2 L\,C_f + j\omega R\,C_f}{R + j\omega L} \tag{I.7}$$

$$Y_{22} = \frac{1 - \omega^2 L\,(C_f + C_{02}) + j\omega R\,(C_f + C_{02})}{R + j\omega L} \tag{I.8}$$

Once the above Y parameters are calculated for each frequency in the user-defined model SSTR, then the values are passed over to the SuperCompact main program in a FORTRAN Y matrix. The Y parameters calculated above are unnormalized.

Appendix II

In order to calculate the Y parameters for the non-center-tapped transformer, three of its four ports are terminated in short circuits and the other port has a voltage source applied to it. Figure II.1 shows ports 2 to 4 being short circuited to ground and port 1 having a voltage source applied to it.

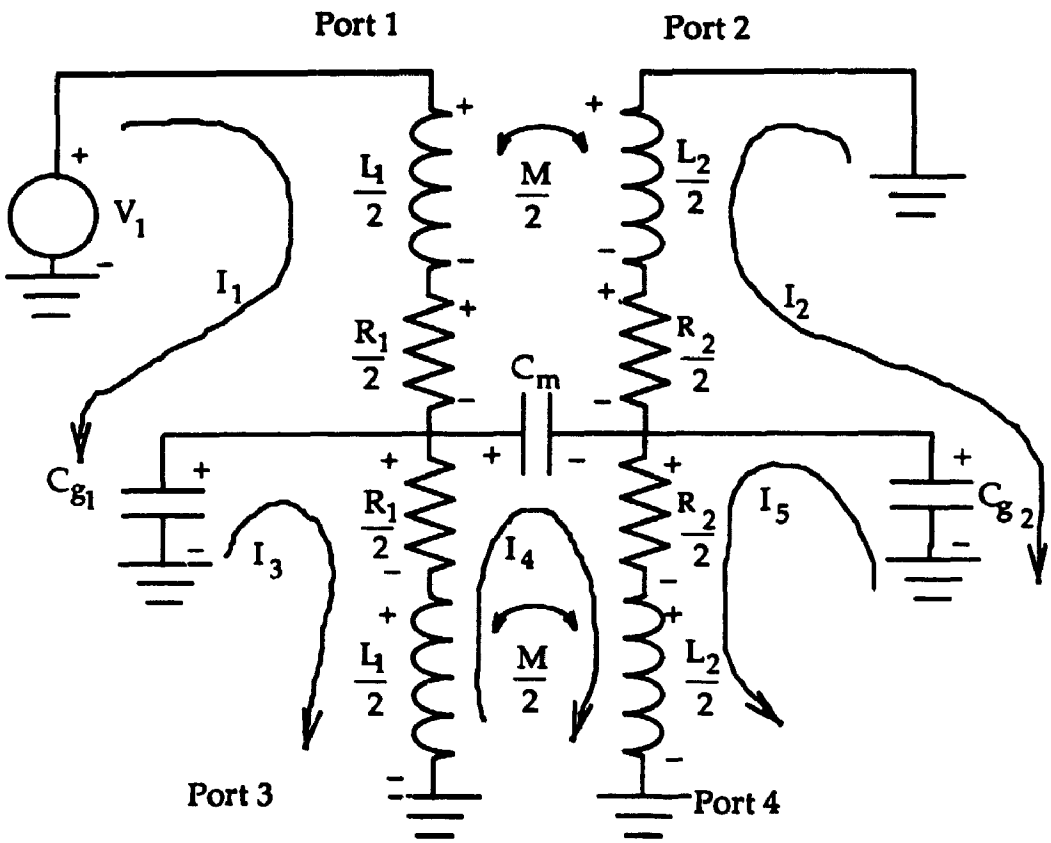

Figure II.1 Schematic of Transformer Model Used to Calculate Y-Parameters

Since the transformers are symmetrical, $L_1 = L_2$, $C_{g1} = C_{g2}$, and $R_1 = R_2$. Therefore, letting

$$Z_1 = j\omega\frac{L_1}{2} = j\omega\frac{L_2}{2} \qquad Z_4 = \frac{1}{j\omega C_m}$$

$$Z_2 = j\omega\frac{M}{2} \qquad Z_5 = \frac{R_1}{2} = \frac{R_2}{2}$$

$$Z_3 = \frac{1}{j\omega C_{g1}} = \frac{1}{j\omega C_{g2}}$$

the equations for the five current loops are found to be :

$$(Z_1 + Z_3 + Z_5)\, I_1 + Z_2 I_2 - Z_3 I_3 = V_1 \tag{II.1}$$

$$-Z_3\, I_1 + (Z_1 + Z_3 + Z_5)\, I_2 + (-Z_1 + Z_2 - Z_5)\, I_4 + Z_2\, I_5 = 0 \tag{II.2}$$

$$\begin{aligned}(-Z_1 + Z_2 - Z_5)\, I_3 + (2Z_1 - 2Z_2 + Z_4 + 2Z_5)\, I_4 \\ + (Z_1 - Z_2 + Z_5)\, I_5 = 0\end{aligned} \tag{II.3}$$

$$(Z_3) I_2 + (-Z_2)\, I_3 + (-Z_1 + Z_2 - Z_5)\, I_4 + (-Z_1 - Z_3 - Z_5)\, I_5 = 0 \tag{II.4}$$

$$(Z_2) I_1 + (Z_1 + Z_3 + Z_5)\, I_2 + (-Z_3)\, I_5 = 0 \tag{II.5}$$

The above equations were solved in the user-defined program SSTR using a Gaussian elimination algorithm. This had to be done at each frequency point which was desired to be analyzed.

When the unknown currents are determined, the following Y-parameters are calculated according to :

$$Y_{11} = \frac{I_1}{V_1} \tag{II.6}$$

$$Y_{21} = \frac{I_2}{V_1} \tag{II.7}$$

$$Y_{31} = \frac{I_4 - I_3}{V_1} \tag{II.8}$$

$$Y_{41} = \frac{-(I_4 + I_5)}{V_1} \tag{II.9}$$

The remaining Y-parameters are calculated from the three other cases possible for a four-port and will not be shown here since the same procedure is used to obtain them.

Appendix III

The calculation of the Y-parameters for the three-port center-tapped transformer is based on its model which is shown below.

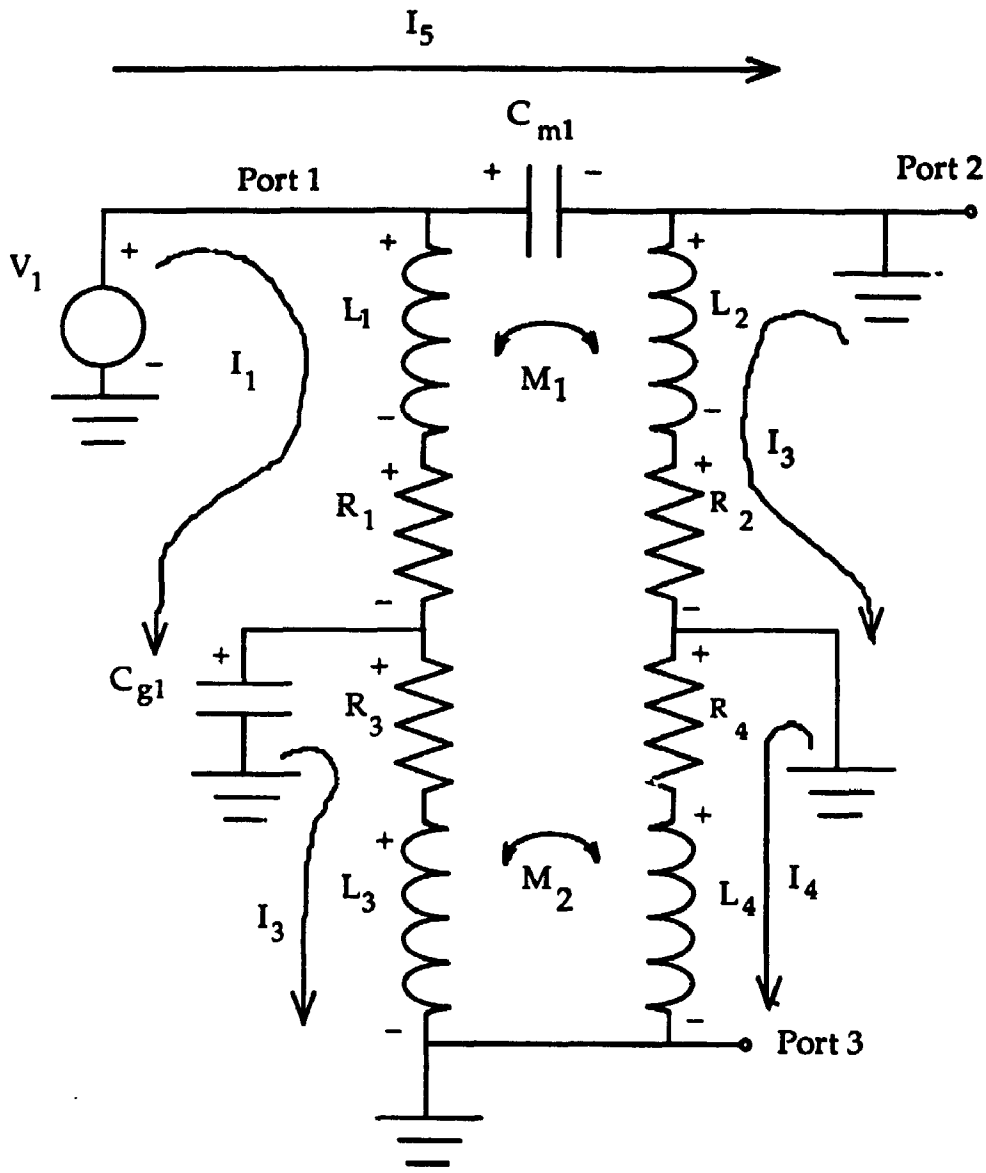

Figure III.1 Schematic of Center-TappedTransformer Model Used to Calculate Y-Parameters

Ports 2 and 3 are terminated in short circuits and a voltage source, V_1, is placed on port 1. Hence, five unknown current, I_1 to I_5, must be solved in order to obtain the three Y-parameters Y_{11}, Y_{21}, and Y_{31}. The two other

cases are used to obtain the six remaining Y-parameters.

The various impedances of the different model elements are shown below :

$Z_1 = jwL_1 = jwL_2$ $\qquad$ $Z_2 = jwL_3 = jwL_4$

$Z_3 = jwM_1$ $\qquad$ $Z_4 = jwM_2$

$Z_5 = \frac{1}{j\omega C_{g1}}$ $\qquad$ $Z_6 = \frac{1}{j\omega C_{g2}}$

$Z_7 = \frac{1}{j\omega C_{g3}}$ $\qquad$ $Z_8 = \frac{1}{j\omega C_{m1}}$

$Z_9 = \frac{1}{j\omega C_{m2}}$ $\qquad$ $Z_{10} = R_1 = R_2$

$Z_{11} = R_3 = R_4$

From figure A3.1, the following equations are obtained :

$$(Z_1 + Z_5 + Z_{10})\, I_1 + Z_3 I_2 - Z_5 I_3 = V_1 \qquad \text{(III.1)}$$

$$Z_3 I_1 + (Z_1 + Z_{10})\, I_2 = 0 \qquad \text{(III.2)}$$

$$-Z_5 I_1 + (Z_2 + Z_5 + Z_{11})\, I_3 + Z_4 I_4 = 0 \qquad \text{(III.3)}$$

$$Z_4 I_3 + (Z_2 + Z_{11})\, I_4 = 0 \qquad \text{(III.4)}$$

$$Z_8 I_5 = V_1 \qquad \text{(III.5)}$$

As for the transformer model, the equations are solved using a Gaussian elimination method which is embedded in the user-defined model as a subroutine. The three Y-parameters which can subsequently be obtained for this case are :

$$Y_{11} = \frac{I_1 + I_5}{V_1} \qquad \text{(III.6)}$$

$$Y_{21} = \frac{I_2 - I_5}{V_1} \tag{III.7}$$

$$Y_{31} = \frac{-I_4}{V_1} \tag{III.8}$$

The other two cases for the three-port provide the six remaining Y-parameters. The equations used will not be shown since they are obtained in the same manner as for the above example.

References

[1] Hoffman, R. K., Translated by Ediss, G.A., Keen, N.J., Handbook of Microwave Integrated Circuits, Copyright 1987, Artech House, Inc., pg. 8.

[2] Sobol, H., "Applications of Integrated Circuit Technology to Microwave Frequencies", Proc. of IEEE, Vol. 59, pg. 1201.

[3] Young, L., Sobol, H., Advances in Microwaves, Volume 8, New York, N.Y., Academic Press, 1974, pp. 184-190.

[4] Greenhouse, H.M., "Design of Planar Rectangular Microelectronic Inductors", IEEE Transactions on Parts, Hybrids and Packaging, PHP-10, No. 2, June 1974, pp. 101-109.

[5] Camp, W.O., Tiwari, S., Parsons, D., "2-6 GHz Monolithic Microwave Amplifier", 1983 IEEE MTT-S Digest, pp. 46-49.

[6] Cahana, D., "A New Transmission Line Approach for Designing Spiral Microstrip Inductors for Microwave Integrated Circuits", 1983 IEEE MTT-S Digest, pp. 245-247.

[7] Shepherd, P.R., "Analysis of Square-Spiral Inductors for Use in MMIC's", IEEE Microwave Theory and Tech., MTT-34, No. 4, April 1986, pp. 467-472.

[8] Wolff, I., Kibuuka, G., "Computer Models for MMIC Capacitors and Inductors", 1984 European Microwave Conference, pp. 853-858.

[9] Lang, D., "Broadband Model Predicts S-Parameters of Spiral Inductors", Microwaves and RF, January 1988, pp. 107-110.

[10] Dueme,P., LeBrun, M., Jay, P.R., Rumelhard, C., "Miniaturisation of a Band-X Monolithic GaAs Amplifier", 1983 IEEE MTT-S Digest, pp. 46-49.

[11] Parisot, M., Archambault, Y., Pavlidis, D., Magarshack, J., "Highly Accurate Design of Spiral Inductors for MMIC's with Small Size and High Cut-Off Frequency Characteristics", 1984 IEEE MTT-S Digest, pp. 106-110.

[12] Jansen, R.H., Wiemer, L., Finlay, A.J., Suffolk, J.R., Roberts, B.D., Pengelly, R.S., "Theoretical and Experimental Broadband Characterization of Multiturn Square Spiral Inductors in Sandwich Type GaAs MMICs", 1985 European Microwave Conference, pp. 946-951.

[13] Grover, F.W., Inductance Calculations, Van Nostrand, Princeton, N.J., 1946. Reprinted by Dover Publications 1962, pp. 17-47.

[14] Maxwell, J.C., A Treatise on Electricity and Magnetism, Parts III and IV, Volume II, article 692, 1st ed., 1873, 3d ed., 1891; reprinted by Dover Publications, New York, N.Y., 1954.

[15] Krafesik, D., Dawson, D., "A Closed-Form Expression for Representing the Distributed Nature of the Spiral Inductor", 1986 IEEE MTT Monolithic Circuits Symposium Digest, pp. 87-91.

[16] Smith, J.I., "The Even- and Odd-Mode Capacitance Parameters for Coupled Lines in Suspended Substrate", IEEE Microwave Theory and Tech., MTT-19, No. 5, May 1971, pp. 424-431.

[17] Waldo, P., Wolff, I., "Dual Bounds Variational Formulation of Skin Effect Problem", 1986 IEEE MTT-S Digest, pp. 333-336.

[18] Pettenpaul, E., Kapusta, H., Weisgerber, A., Mampe, H., Luginsland, J., Wolff, I., "CAD Models of Lumped Elements on GaAs Up to 18 GHz", IEEE Microwave Theory and Tech., MTT-36, No. 2, February 1988, pp. 294-304.

[19] Haefner, S.J., "Alternating Current of Rectangular Conductors", Proceedings of IRE, Vol. 25, pp. 434-447, 1937.

[20] Gupta, K.C., Garg, Ramesh, Bahl, I.J., Microstrip Lines and Slotlines, Artech House, Inc., 1979, pp. 91-92.

[21] Kirschning, M., Jansen, R.H., Koster, N.H.L., "Measurement and Computer-Aided Modeling of Microstrip Discontinuities by an Improved Resonator Method", 1983 European Microwave Symposium, pp. 495-497.

[22] SuperCompact User Manual, User Circuit Model Installation Guide, Appendix 11-1 - 11-67.

[23] Jamison, S.A., Podell, A., Helix, M., Ng, P., Chao, C., "Inductively Coupled Push-Pull Amplifiers for Low Cost Monolithic Microwave ICs", 1982 IEEE GaAs IC Symposium, pp. 91-93.

[24] Ferguson, D., Bauhahn, P., Keuper, J., Lokken, R., Culp, J., Chao, C., Podell, A., "Transformer Coupled High-Density Circuit Technique for MMIC", 1984 IEEE MTT-S Digest, pp. 34-36.

[25] Wiemer, L., Jansen, R.H., Robertson, I.D., Swift, J.B., "Computer Simulation and Experimental Investigation of Square Spiral Transformers for MMIC Applications", IEE Colloquium on "Computer Aided Design of Microwave Circuits", Digest No. 99, Nov. 11, 1985, p. 2/1-5.

[26] Frlan, E., Meszaros, S., Cuhaci, M., Wight, J.S., "Computer Aided Design of Square Spiral Transformers and Inductors", 1989 IEEE MTT-S Digest, pp. 661-664.

[27] Tripathi, Vijai K., "Asymmetric Coupled Transmission Lines in an Inhomogeneous Medium", IEEE Microwave Theory and Tech., MTT-23, No. 9, September 1975, pp. 734-739.

[28] Mondal, Jyoti P., "An Experimental Verification of a Simple Distributed Model of MIM Capacitors for MMIC Applications", IEEE Microwave Theory and Tech., MTT-35, No. 4, April 1987, pp. 403-408.

[29] Bedair, S.S., Sobhy, M.I., "Accurate Formulas for Computer-Aided Design of Shielded Microstrip Circuits", IEE Proc., Vol. 127, Part H, No. 6, December 1980, pp. 305-308.

[30] Robertson, I.D., Aghavami, A.H., "Novel Coupler for Gallium Arsenide Monolithic Microwave Integrated Circuit Applications", Electronic Letters, 8th December 1988, Vol. 24, No. 25, pp. 1577-1578.

[31] Engelbrecht, R.S., Kurokawa, K., "A Wide-Band Low Noise L-Band Balanced Transistor Amplifier", Proc. of IEEE, March 1965, Vol. 53, pp. 237-247.

[32] Saunders, T.E., Stark, P.D., "An Integrated 4-GHz Balanced Transistor

Amplifier", IEEE Journal of Solid-State Circuits, March 1967, Vol. SC-2, pp. 4-10.

[33] NE710 Preliminary Data Sheet, "Low Noise Ku-K Band GaAs Mesfet", NEC Corporation.

END

13 09 90

FIN